A NOVEL COMPACT SHEAROGRAPHIC NDT SYSTEM

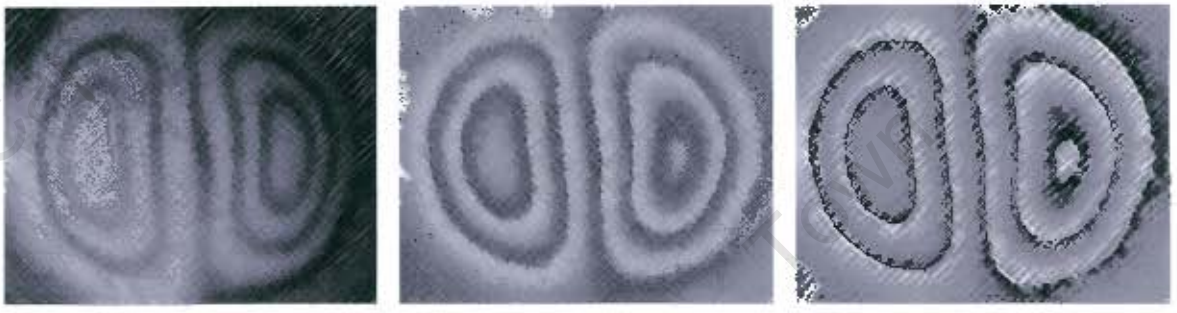

BY

Avinash Andhee

BSc. Mechanical Engineering

August 2005

A dissertation submitted to the Faculty of Engineering in partial fulfilment of the degree of Master of Science in Engineering.

University of Cape Town

Non-Destructive Testing Laboratory

DECLARATION

I hereby declare that this dissertation contains only my own original work, except where reference is made with acknowledgement to others. I also declare that this material has not been submitted for any purpose or examination to any other Department or University.

Signed by candidate

Avinash Andhee
August 2005

Acknowledgements

If I had to thank everyone who helped me get to where I am today then this document would be nothing but an acknowledgement of thanks. However, I would like to express my most sincere appreciation to the following people who have assisted and guided me during the course of this thesis.

Firstly, I would like to thank my supervisors Mr. D Findeis and Prof. J Gryzagoridis for their guidance, support and humor throughout my thesis.

I would like to thank the workshop staff namely; Glen Newins, Horst Emrich, Hubert Tomlinson and Martin Batho for their help with the machining of components and other minor catastrophes.

To my friends in the Mechanical Engineering Department: Sheilen Rambocus thanks for being a good friend throughout the years, Gerswyn Mckuur and Madia Matlali thanks for the encouraging and philosophical conversations that we had.

To my parents Krishna and Renitha Andhee to whom I have dedicated this thesis, thanks for all the love, support, patience, and motivation that you have shown me through the years.

A special thanks to my girlfriend Yanisha Sumbhoolaul for her motivation, love and support throughout my post graduate studies. I hope that we remain together forever.

Most of all I would like to thank God, without whom none of this would have been possible.

Dedicated to my parents
Krishna and Renitha Andhee

Thanks for all the love and support

SYNOPSIS

There is a need in industry and the NDT (Non-destructive Testing) community for quick, reliable, user-friendly and cost-effective compact NDT systems that can be used on a wide variety of materials and structures, for quality assurance and maintenance. Designing and building a compact Shearographic NDT system will enhance the capability of inspection during quality assurance and maintenance routines as well as reduce inspection time. Older compact Shearographic systems, which have been tested satisfactorily both under laboratory and field conditions at the NDT Laboratory at the University of Cape Town, have a rather restricted field of view. This is due to the proprietary shearing optics being placed in front of the camera lens, which in other words means that the field of view can only be increased by using a relatively small focal length camera lens which results in having to increase the size of the shearing optics. This would make the compact Shearographic device much larger which is counter-productive since technology enables/directs research and development toward more compact devices.

The new proposed Shearographic system has its shearing optics between the camera lens and CCD (charge-coupled device) camera. This feature will increase the field of view in that; it will only depend on the focal length of the camera lens, rather than being dependant on the size of the shearing optics as well. The proposed shearing device will also render the Shearographic system more versatile as zoom lenses of different magnifications can be attached to the device depending on the distance from the object and magnification required. A manually adjustable iris will be incorporated into the device between the camera lens and shearing optics so that the MTF (Modulation Transfer Function) of the imaging lens can be manipulated. MTF is a measure of a lens's ability to transfer contrast at varying resolution levels from the object plane to the image plane. Therefore it is an important parameter to control when clear and well defined images are essential.

Digital Shearography is a well established and widely used full field non-contacting optical interference technique that produces contour maps (i.e. fringe patterns) of measured

displacement gradients (i.e. strain) of an object under inspection, when stressed. The most attractive feature of Shearography is its quick and near-real-time method of strain measurement. It also has many advantages over other major optical interferometric methods such as ESPI (Electronic Speckle Pattern Interferometry) in that it has a common laser path and is therefore unaffected by environmental disturbances.

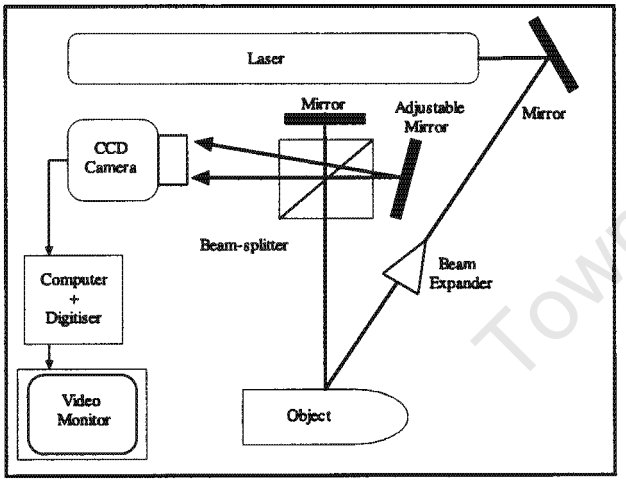

Figure 1: Typical Shearography set-up

A typical Shearography set-up is shown in figure 1, where it can be seen that the object under inspection is illuminated with monochromatic laser light. The light that is reflected off the object is viewed through a set of shearing optics, which has the ability to generate two laterally sheared images of the object. The two sheared images overlap in the image plane of the CCD camera resulting in a unique speckle pattern of the unstressed object (i.e. the reference image), which is then digitized and stored for later use by the personal computer. The object is subsequently stressed by thermal, pressure or mechanical methods, which causes the intensity distribution of the speckle pattern to change. The subsequent speckle pattern is then captured, digitized and compared to the unstressed speckle pattern (i.e. the reference image) of the object resulting in an interferogram which consists of alternating black and white "zebra-like" fringes as shown in figure 2.

Figure 2: A typical interferogram/fringe pattern

Phase-stepped Shearography, unlike Conventional Shearography is a quantitative method of data measurement and is also incorporated into the design of the Shearographic system. It is derived from the intensity integration method and has the following advantages over Conventional Digital Shearography:

- The technique dramatically increases the sensitivity of inspection by manifesting fringes that are much more prominent due to the reduction in noise.
- It allows for filtering of the fringe pattern.
- Data can be quantified.

Phase-stepping can be easily incorporated into the design of the Shearographic system as the only hardware required is a piezo-electrically driven mirror which can be easily fitted to either "arm" of the shearing device. However, the custom software must have the additional subroutines to perform the subtraction processes as the Phase-stepped Shearography equations differ from the Conventional Shearography equations. Phase-stepped Shearography produces much better quality fringe patterns since four measurements of the stressed object at known phase-steps are compared to the unstressed image of the object. This results in a reduction in noise when an interferogram is generated.

Subsequent to designing and building the compact Shearographic system, the device was calibrated by inspecting a helicopter blade with "manufactured" defects to establish the suitability of the device in detecting the presence and location of flaws.

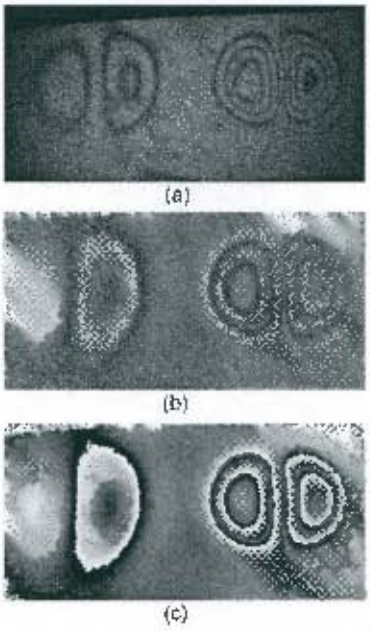

Figure 3: Fringe pattern of two defects located at the leading edge and middle of the helicopter blade using: (a) Shearography, (b) Phase-stepping (c) Filtering.

Figure 3(a) depicts the Shearographic fringe pattern that was produced while inspecting manufactured defects of equal size at the leading edge and the middle of the aerofoil section. The "double bull's eye" on the left shows the presence and location of the leading edge defect whereas the "double bull's eye" on the right locates the middle defect. It can be seen that the leading edge defect has manifested two fringes whereas the middle defect has manifested three. This is due to the middle defect being closer to the inspection surface (i.e. deeper from the far side/surface) than the leading edge defect. The number of fringes in an area where a defect is located does usually indicate the amplitude of the localized displacement induced, which is influenced by the size of defect and its depth. Figures 3 (b) and (c) depicts the Phase-stepped Shearography and Phase filtered fringe patterns respectively, where it can once again be seen that the middle defect has manifested more fringes.

The design parameters such as the intensity of laser illumination and the diameter of the manual iris were explored so as to determine the optimum setting of the Shearographic system for good quality fringe patterns to be produced. The final stage of testing was the implementation stage where a section of the main rotor helicopter blade was inspected.

Figure 4 summarizes the results of the inspection by depicting the phase-filtered fringe patterns as well as their location on the helicopter blade, where fringe anomalies had been observed.

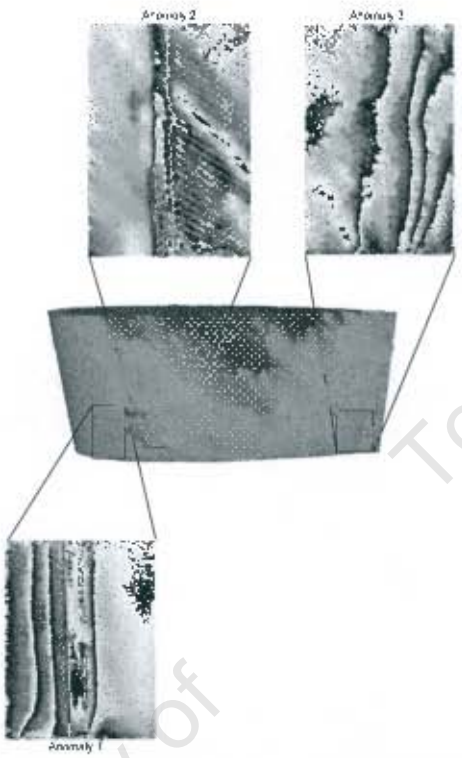

Figure 4: Schematic depicting the location and resulting Phase filtered fringe pattern of anomalies detected during inspection.

The areas where fringe anomalies were observed on the helicopter blade where marked off and cut open to establish the reason for the anomalies. Furthermore, this would determine if the Shearographic system produced clear and unambiguous results.

The following major conclusions were drawn from the results:

1. The Shearographic system is capable of detecting the presence and location of defects in composite structures. Furthermore, the device can differentiate between defects of varying depth by manifesting the appropriate number of fringes.

2. The number of fringes that can be manifested by a flaw is dependent on the period of stressing (when using heating or cooling techniques) as well as the amount of time before the fringe pattern is captured by the user.

3. The correct amount of laser illumination is important when measuring the displacement gradient of an object. An abundance of laser light saturates the pixels of the CCD detector resulting in those pixels not contributing to the measurement of the displacement gradient. On the other hand, insufficient laser light makes it difficult for the phase to be extracted resulting in fringes that are not well contrasted and not clearly visible.

4. The field of view of the Shearographic system is a function of the optical configuration and the available laser illumination. The Shearographic system is capable of using CCTV (Closed Circuit Television) lenses of different focal lengths and has an optical field of view of 57 degrees when using the 8.5mm focal length CCTV lens. Therefore the only variable that limits the field of view of the device is the available laser illumination. Laser light is normally available in collimated "pencil like" beams. This beam must be expanded using suitable optics to cover the required surface area. However, the more one expands the beam, the lesser the illumination intensity becomes, a fact that can only be remedied by using a higher laser power.

5. The MTF rating of a lens, which can be manipulated by adjusting the aperture of a lens, affects the contrast and fringe definition of a fringe pattern. Reducing the size of the aperture of a lens increases the MTF and improves the contrast and resolution of a fringe pattern.

The following recommendations can be made:

1. The compact Shearographic system has been successfully tested under laboratory conditions; further work should be done to make the device fully portable so that testing can be done under field conditions to confirm that the results will be still satisfactory.

2. The only variable that limits the field of view of an inspection area, using the proposed Shearographic system is the laser power. Therefore, further studies should be done to determine if two lasers of the same power can be used simultaneously or if a higher power laser can be made portable to improve light distribution and intensity.

3. Another method of increasing the field of view of inspection is to use a CMOS (Complementary Metal Oxide Semiconductor) camera[32] instead of a CCD camera. The CMOS camera allows the user to program the dynamic range of each pixel independent of each other whereas the CCD camera has a limited dynamic range, which means that a CMOS-sensor can gather more light than a conventional CCD-detector under the same illumination conditions. Therefore a comparative study should be done to determine the light efficiency and image quality of the fringe patterns, when using CMOS camera and the CCD camera.

TABLE OF CONTENTS

Page

LIST OF ILLUSTRATIONS

Figures

Appendix A

Tables

Appendix A

1. INTRODUCTION

1.1 Background

There is a need in the South African Air Force and aerospace industry for quick and effective Non-Destructive Evaluation (NDE) techniques for the inspection of aircraft during routine maintenance schedule. Designing and building a compact Shearographic NDT system will enhance the capability of inspection during maintenance as well as reduce the inspection time. Researchers at the Non-Destructive Testing (NDT) laboratory at the University of Cape Town have developed a compact Shearographic prototype which has been tested satisfactorily both under laboratory and field conditions[1,2,3]. The prototype has a proprietary shearing optics device placed in front of the camera lens with a rather restricted field of view. In other words, the field of view can only be increased by decreasing the focal length of the camera lens which results in having to increase the size of the shearing optics. Increasing the size of the shearing optics would make the prototype larger which was considered counter-productive, since technological advances enable or direct research and development toward more compact devices.

The new proposed Shearographic system has its shearing optics between the camera lens and CCD (charge-coupled device) camera. This feature will increase the field of view in that; it will only depend on the focal length of the camera lens, rather than being dependant on the size of the shearing optics as well. The proposed shearing device will also render the Shearographic system more versatile as zoom lenses of different magnifications can be attached to the device depending on the distance from the object and magnification required.

Modern Shearography, which is more formally known as Digital Speckle-Shearing-Pattern Interferometry (DSSPI) is a well established and widely used full field non-contacting optical interference technique that measures displacement gradients (i.e. strain) as well as curvature and vibrations of a specimen under inspection. An attractive feature of Shearography is its quick and near-real-time method of strain measurement. Shearography is used in a wide

variety of fields such as in academic and industrial research as well as inspection areas, which include experimental mechanics, vibration analysis and non-destructive evaluation (NDE). In the field of NDE, Shearography is aimed at detecting defects and has many advantages over other major optical interferometric methods such as ESPI (Electronic Speckle Pattern Interferometry). An in-depth comparative study of Digital Shearography and ESPI was done by Y.Y. Hung[4] concluding that Shearography has the following advantages over ESPI:

- It requires a simpler optical setup, thus eliminating the optical alignment problems.
- The coherent length requirement is greatly reduced.
- Shearography provides a wider and more controllable range of sensitivity, thus allowing large deformations to be inspected which is not the case in ESPI as it is too sensitive for many practical NDE applications.
- Rigid body motion does not influence the resulting fringe patterns, since Shearographic NDE uses a "common path" optical arrangement.

Furthermore, both Shearography and ESPI measure surface deformation, however the information they yield differ. ESPI yields surface displacement information whereas Shearography yields derivatives of surface displacement (i.e. strain). This makes Shearography more practical than ESPI as flaws normally create strain concentrations and therefore it is easier to correlate flaws with strain anomalies rather than with displacement anomalies.

Shearography is a versatile tool that can be used to inspect a wide variety of materials, including composites as shown in studies by Y.Y Hung[5], T Mayer[6] and R Krupka[7] as well as D Findeis and J Gryzagoridis[1, 3, 8]. These studies have also shown that different types of defects such as cracks, voids, delaminations and debonds can be detected. Consequently, Digital Shearography has received world-wide industrial acceptance for non-destructive testing. It is currently being used by the tire industry for evaluating tires, and in the aerospace industry for the non-destructive testing of aircraft structures, in particular, composite structures[9]. Shearography is also emerging as a novel industrial NDT tool in other industries such as the automotive industry. Digital Shearography has been researched and developed for

approximately a quarter of a century with the first full scale implementation of Shearographic NDT system being applied in the production of the Northrop B-2 Bomber by Northrop Grumman Corp. in 1988.

Shearography was invented in the early 1970s due to research efforts focusing on the development of novel methods for performing high sensitivity measurements on diffusely scattering illumination surfaces. However, at that stage it was limited in acceptance in that, photographic film was being used as the recording medium, which was tedious and costly. Interest in Shearography declined during the late 1970's until the 1980's when CCD cameras linked to image-processing modules replaced photographic film. At this point, Shearography became known as Digital or Electronic Shearography. The introduction of Phase Stepping and computerized fringe analysis has further helped to spread the use of Digital Shearography. Phase stepping and filtering of images dramatically increases the amount of information gained from an inspection as will be discussed later in this chapter. Advances in technology, particularly with respect to high resolution and high-speed data acquisition systems, as well as software development, has brought Digital Shearography to a new threshold, where it stands today.

The motivation to develop speckle based techniques came about due to the invention of the laser in 1960 and the realization that speckle could carry significant amounts of information about position and surface structure of a rough object[10,11].

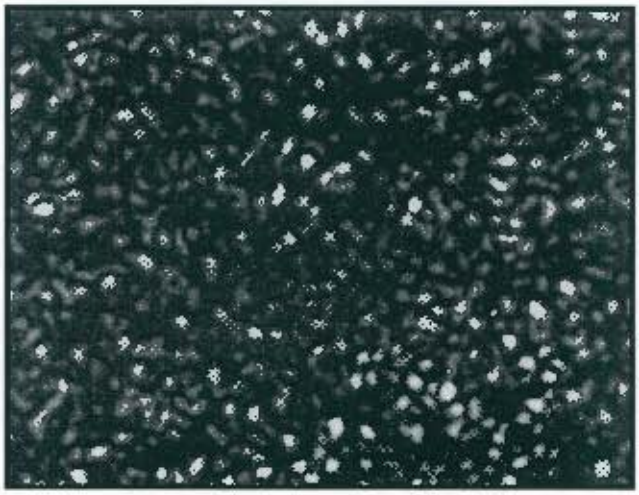

Figure 1.1: Typical laser speckle pattern

Speckle interferometric techniques (i.e. Shearography, ESPI and Holography) rely on the very basic phenomenon of light interference namely that objects illuminated with laser light have a granular appearance. Speckle as pictured in figure 1.1 is observed when an object is illuminated with coherent laser light. Most objects are optically rough even if they are rough only at a microscopic level. However, a speckle field can only be created if the height variation of a surface is of the order of or greater than the wavelength of the illuminating light. Speckle (i.e. the granular appearance) is created by the interference of wavelets of coherent light of different path length due to surface roughness. Each point on the object surface will reflect light. Furthermore, interference will occur between these object points due to the high coherence of laser light. If this is viewed by a detector, a random pattern of interference fringes (i.e. speckle) will be observed. This randomness is due to surface roughness, which causes a path length variation (i.e. phase variation), of scattered laser light in proportion to local height variation from point to point. This means that a speckle pattern is unique for a given object surface, illumination and viewing conditions.

The laser has been used in a wide variety of metrological and industrial inspection systems[12]. Light emitted from a laser is unusually simple in form, with variables that are quite constant with time and can be measured with high precision. This means that lasers offer brightness, high degrees of coherence and are monochromatic, which makes them the quintessential light

source for interferometry. However, a laser beam is only monochromatic over a certain distance and will only approximate a sine wave of fixed frequency for a certain distance, known as the coherence length[13].

There are many types of lasers on the market that can be used for interferometry, with varying power, wavelength and coherence length. The most commonly used laser is the Helium Neon (HeNe) laser, which is relatively inexpensive and easily available. The wavelength of the HeNe laser is 632.8nm, with power varying from 0.1 to 50mw and the coherence length varying from 5 to 30cm.

The Michelson interferometer is the most commonly used shearing device in Shearography and was invented in 1881 by Albert Michelson. He was awarded the Noble prize in physics for his optical instruments of precision and the spectroscopic and metrological investigations he executed with them. The Michelson interferometer measures out-of-plane displacement gradients with accuracy of the order of one wavelength of light used and can be modified to increase the accuracy to a tenth or even a hundredth of a wavelength.

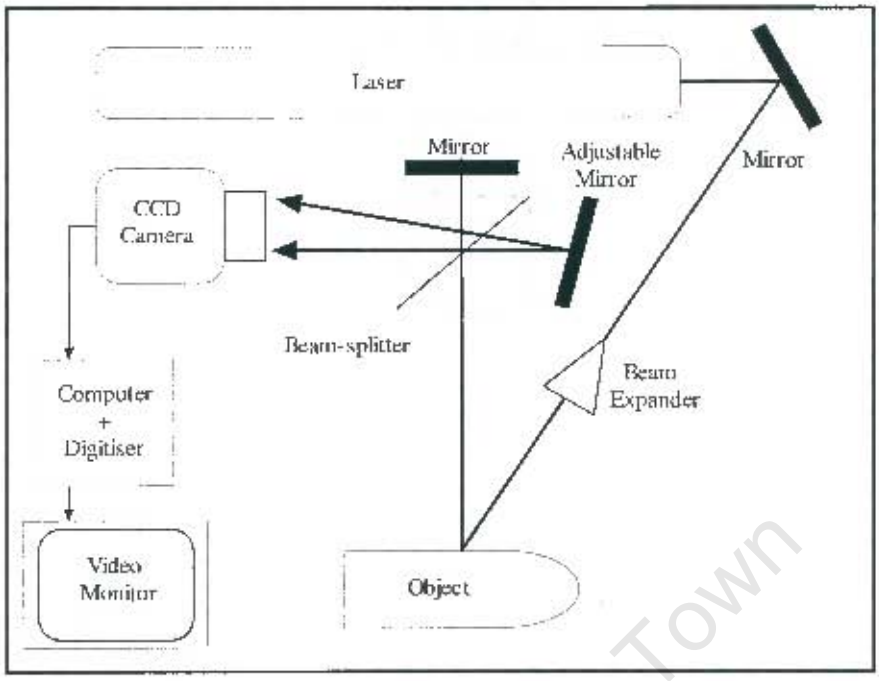

Figure 1.2: A typical Shearographic setup

A typical Digital Shearographic set-up is shown in figure 1.2. The object to be inspected is illuminated with monochromatic laser light which is dispersed by a beam expander so that it covers the entire object. The light that is reflected off the object traverses a set of shearing optics which laterally shears the image of the object into two. As a result, the two sheared images overlap when imaged onto the CCD camera. In other words, this also means that two neighboring object points $P(x,y)$ and $P(x + \delta x,y)$ now meet in the image plane, where δx is the magnitude of shearing parallel to the x-axis. Due to the monochromatic nature of laser light, the overlapped images produce a unique speckle pattern. This speckle pattern known as the reference image (i.e. unstressed image) is transmitted by the CCD camera to a personal computer, which digitizes and stores it for later use.

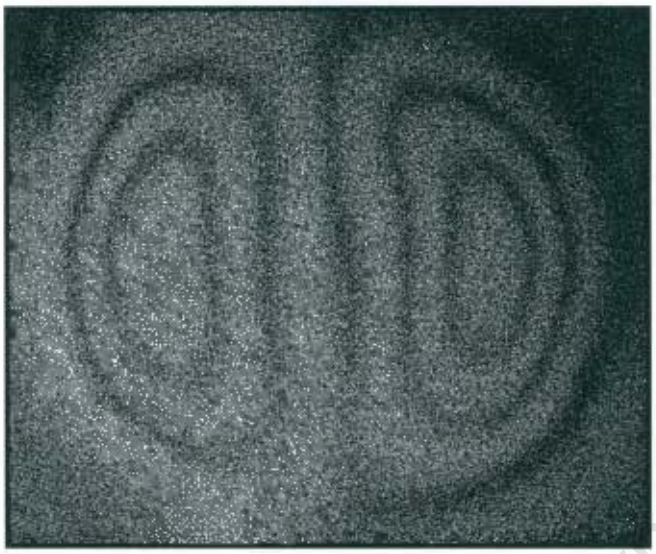

Figure 1.3: A typical fringe pattern

The object is subsequently stressed by either mechanical, pressure or thermal methods. Stressing of the object causes the surface of the object to distort and the intensity distribution of the speckle pattern changes. This is due to a change in the relative displacement of $P(x,y)$ and $P(x + \delta x,y)$ when the object is stressed. The second speckle image is digitized and subtracted from the reference speckle image. A final image is formed which contains "zebra" like black and white fringe patterns. An example of a typical fringe pattern of a laterally sheared image is illustrated in figure 1.3, where the fringe pattern looks like a double bull's eye. Shearographic fringe patterns differ from ESPI fringe patterns which appear as a single concentric fringe pattern as shown in figure 1.4.

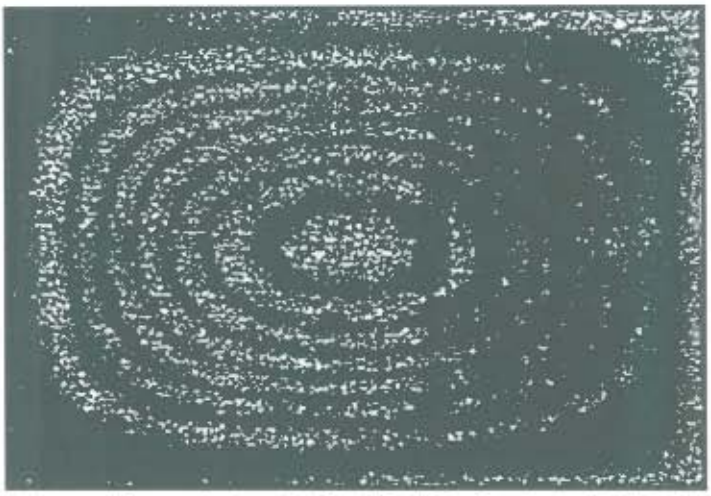

Figure 1.4: Typical ESPI fringe pattern[4]

The difference between the two types of fringe patterns becomes more apparent when a plot of deflection of an object as in figure 1.5(a) and a plot of the corresponding deflection derivative (as shown in figure 1.5(b)) is analyzed. It can be seen from the figure that ESPI measures the surface deflection whereas Shearography measures the strain which is the deflection derivative with respect to x since the image is being sheared parallel to the x-axis.

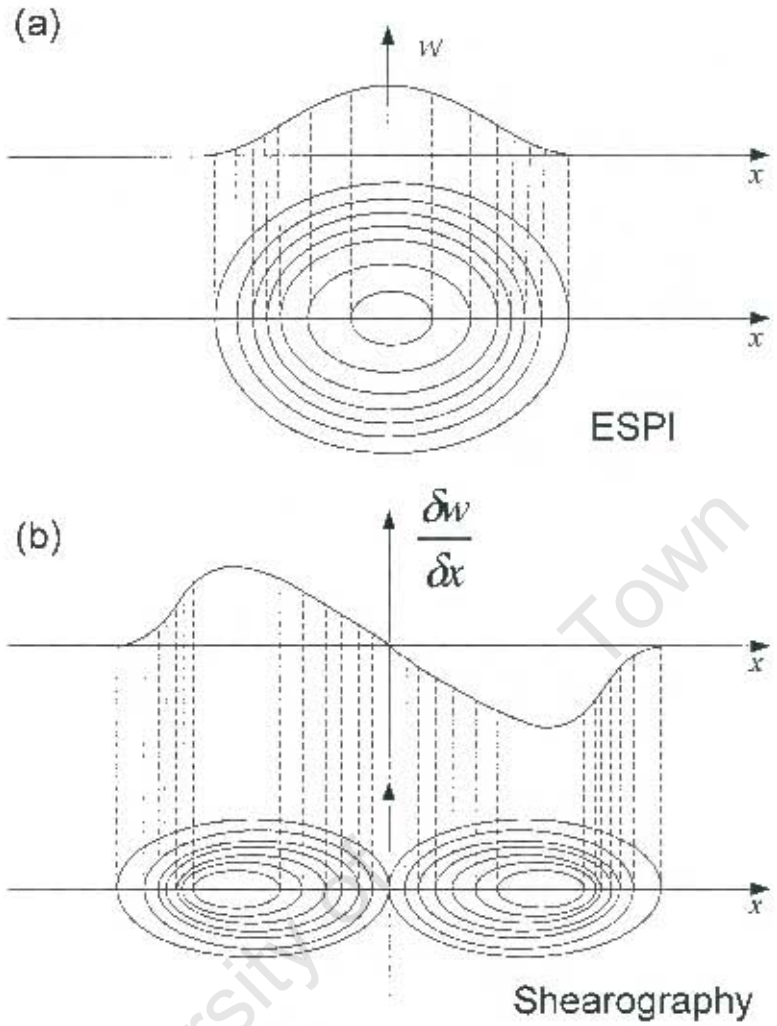

Figure 1.5: Plot of: (a) Single bull's eye fringe pattern in ESPI and (b) Double bull's eye in Digital Shearography for the deformation on an object

The Shearographic fringe pattern can also be translated into a 3D plot by means of an automated phase extraction technique employing a phase shift technique, done by Y. Y Hung[14]. The 3D plot is shown in figure 1.6 where the change in slope of the deflection derivative illustrates the points of maximum and minimum rate of deflection.

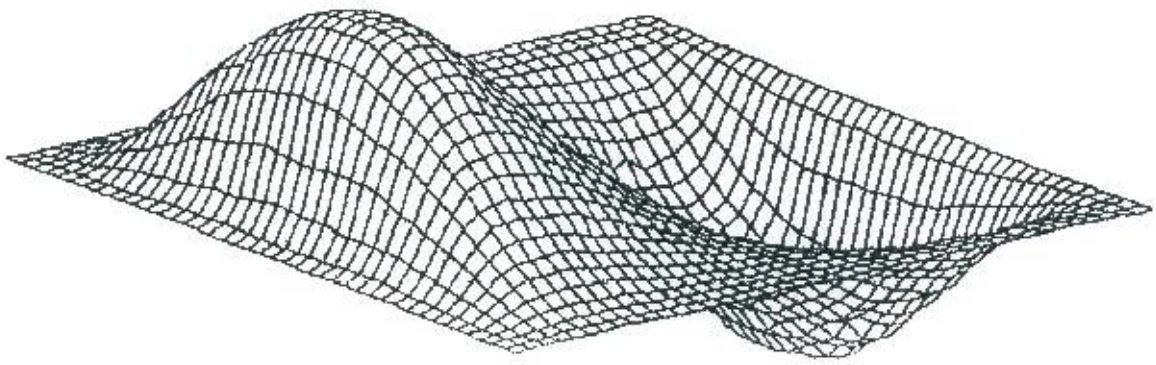

Figure 1.6: A 3D plot of the deflection derivative distribution of a Shearographic fringe pattern[6]

Phase-Stepped Shearography is a quantitative method of data measurement and is also incorporated into the design of the Shearographic system. It dramatically increases the sensitivity of the device and is derived from the intensity integration method. A comparative study of Conventional Digital Shearography and Phase-stepped Shearography was done by A. Andhee, J. Gryzagoridis and D. Findeis[15]. The study concludes that Phase-stepped Shearography has the following advantages over Conventional Digital Shearography:

- The technique dramatically increases the sensitivity of inspection by manifesting fringes that are much more prominent due to the reduction in noise.
- It allows for filtering of the fringe pattern.
- Data can be quantified.

A typical setup of Phase-Stepped Shearography is shown in figure 1.7. It can be seen from the figure that the Phase-Stepped Shearographic hardware can be easily incorporated into the Shearographic system as only a piezo-electrically driven mirror has to be fitted. However, the custom software installed on the personal computer must have additional subroutines installed to perform the subtraction processes needed to generate the fringe patterns in Phase-Stepped Shearography as the equations differ from Conventional Shearography.

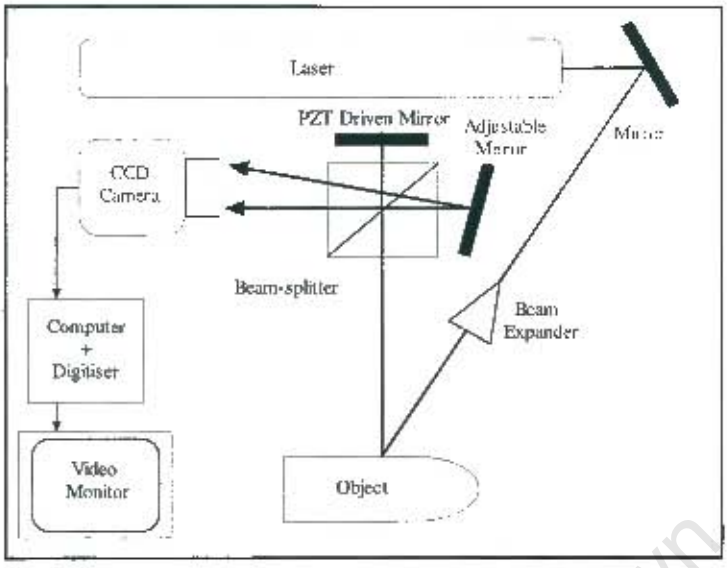

Figure 1.7: A typical Phase-Stepped Shearographic setup

The phase-stepping technique requires a minimum of three measurements (i.e. speckled images) to solve for three unknowns; however four measurements are more commonly used. Phase-steps are produced by mechanical micro-displacements of a piezo-electrically driven mirror, which is calibrated before testing can commence. The PZT (Piezo-electric Transducer) is the most commonly used device in phase-stepping in that it is cost effective and requires minimal power. The micro-displacements are produced by applying a voltage across the piezo-electric crystals which results in their expansion. A low voltage PZT can provide translation of a fraction of a micro-meter. The custom software also controls the piezo-electric transducer by sending a binary number to an expansion card fitted on the PC. The binary number is then converted into a voltage by a digital to analogue converter and sent to the piezo-electric transducer via a cable that connects it to the computer so that a calibrated micro-displacement can occur.

Each micro-displacement of the piezo-electrically driven mirror initiates phase-steps of $\pi/2$ increments, which is equivalent to changing the path length of the laser beam by a quarter of a wavelength. After each phase-step, a speckle image of the stressed object is captured by the image processing system. As mentioned earlier four measurements or speckled images are captured and this is known as the 4-bucket system. The four measurements are taken in less

than a second and the phase can then be described by these four measurements. The phase difference can then be calculated by subtracting the phase of the image of the stressed object from the phase of the image of the unstressed object. Subsequent to subtraction and altering of the limits, the phase difference lies within the range of 0 to 2π radians and thus contains 2π discontinuities.

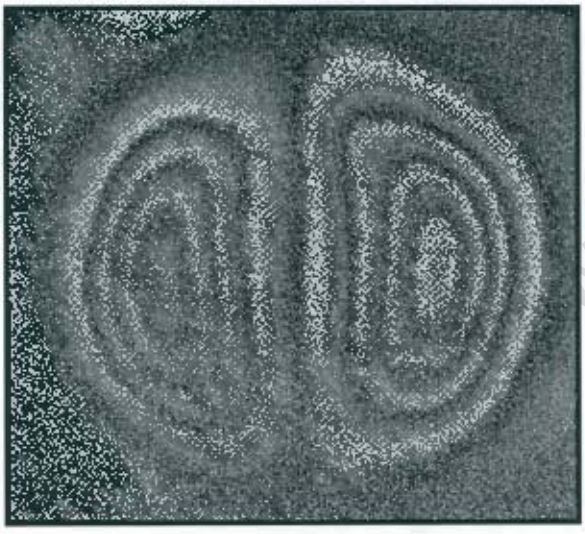

Figure 1.8: Typical phase map using Phase-Stepped Shearography

Once the phase difference is calculated using the image processing software, a phase map is produced consisting of fringes ranging from black to white and then suddenly changing to black again. This "saw tooth" pattern continues throughout the image as shown in figure 1.8. This drastic change occurs due to the phase difference increasing towards 2π and then jumping back to zero when the limit of 2π is reached. This means that in the final image, black represents the smallest phase difference and white the largest. The regions where these discontinuities occur are called 2π discontinuities and are the main characteristics of phase-stepping, which help determine the relative direction in which deformation takes place.

A paper written by Y. Bar-Cohen[16] titled "In-Service NDE of Aerospace Structures – Emerging Technologies and Challenges at the end of the 2nd Millennium" states the following:

"The requirements for NDE are continuing to be driven by the need for lower cost methods and instruments with greater reliability, sensitivity, user friendliness and high operation speed as well as applicability to comply with all materials and structures."

Later in the paper he also writes the following:

"Effective field inspection requires a portable, user friendly system that can rapidly scan large areas of complex structures"

It is clear that the NDE community and industry require portable/compact NDE methods which are reliable, sensitive, user-friendly, fast and cost-effective which are useable on a wide variety of materials and structures. Researchers such as Y. Y. Hung[17], M. Kalms[18] and S. Waldner[19] have already realized the need to meet these requirements and have attempted to design portable/compact Shearographic systems. It has been claimed that these prototypes produce satisfactory results under laboratory and field conditions. However, little or nothing is known about the optical configuration used to design these devices. Therefore the aim of this thesis is to design, build and test a novel compact Shearographic system capable of rapidly scanning the surface of test pieces and displaying clear unambiguous results.

1.2 Problem Clarification

This section breaks down the project and describes in full the objectives and design requirements of the project. The design requirements will be used later to decide on the best design concept which will be implemented into the final solution.

1.2.1 Objectives of this work

The main objectives of this research and development were to:

- Design a compact DSSPI (Digital Speckle-Shearing-Pattern Interferometer).
- Calibrate the DSSPI by inspecting an object containing defects/flaws.
- Vary the design parameters so that optimum performance and deeper understanding of compact shearing interferometry can be achieved.
- Test the device on a high value engineering component with suspected defects.

1.2.2 Design Requirements

The design requirements of this project were to:

- Design a compact Michelson type shearing interferometer.
- Place the shearing optics between the CCD camera and zoom lens so that the field of view can be varied.
- The overall dimensions of the shearing interferometer and the CCD camera should be approximately the size of an A5 page which is half the size of the previous prototype.
- Attachment of various focal length c-mount CCTV (Closed Circuit Television) zoom lenses must be possible.
- An iris should be incorporated into the device so that the laser light intensity can be controlled.
- One of the mirrors within the Michelson type interferometer must be capable of making small angle rotations in at least two axes to introduce shear on the observation plane.
- Phase-stepping must be incorporated into the design of the compact Shearographic interferometer, to enhance the quantitative results.
- The prototype must be able to inspect a minimum area of 300mm by 200mm (i.e. larger objects can be inspected in sections over a short period of time).
- The fringe patterns must be clearly visible and unambiguous.

1.3 Procedure used to gather Information

The information on which this thesis is based was gathered by means of:

- Books
- Papers
- Catalogues
- Correspondence with companies
- Internet searches
- Meetings with supervisors

1.4 Plan of Development

Chapter two establishes the basic principles of Digital Shearography and Phase-Stepped Shearography. Digital Shearography is discussed with particular reference to displacement gradient measurement followed by the factors which limit the application of the technique.

Chapter three outlines the important sections of the appendices which contain the background theory of optics. This information may be required by the reader, as an in-depth knowledge of optics was required to design the novel Shearographic system.

Chapter four begins by explaining the workings of the individual components that make up the Shearographic system. The optical configuration of the various design concepts, which were considered for the designing the Shearographic system, are then discussed. The advantages and disadvantages of each design concept are discussed so that the best solution could be implemented, with regard to the design requirements.

Chapter five explains in detail the experimental procedure that was used to obtain the results of this investigation. The setup of the Shearographic equipment as well as the manufacturing of the calibration specimens is then discussed.

Chapter six lays out the results of the investigation, which are the resulting Shearographic, Phase-stepped Shearographic and phase filtered fringe patterns.

Subsequent to analyzing the fringe patterns conclusions are drawn in chapter seven, followed by recommendations for further work in chapter eight.

2. BACKGROUND THEORY

2.1 Digital Shearography

The compact Shearographic Interferometer designed in this investigation will only be used in the field of Non-Destructive Testing to inspect high value engineering components. For this reason the compact Shearographic Interferometer will only be capable of measuring out-of-plane displacements gradients of stressed objects. The following section describes this technique in greater detail.

2.1.1 Principles of Digital Speckle-Shearing-Pattern Interferometry

A schematic diagram of a Digital Shearographic system is shown in figure 2.1 illustrating the path of a light beam from the object to the CCD Camera. Subsequent to reflection off the object, the light beam is split into two equal parts by the beam-splitter and travels through the two "arms" of the interferometer. One arm of the interferometer shears the image using a small tiltable mirror and directs the beam of light back into the beam-splitter. The other mirror (i.e. arm) satisfies the coherence length of the laser by making the split beam of light travel a distance equal to the beam of light in the first arm (the need for equal beam path length is discussed later in the section). A major disadvantage of this optical configuration is that when the light beams recombine at the beam-splitter only half the intensity of the light enters the CCD Camera since the other half of the light is guided out by the beam-splitter.

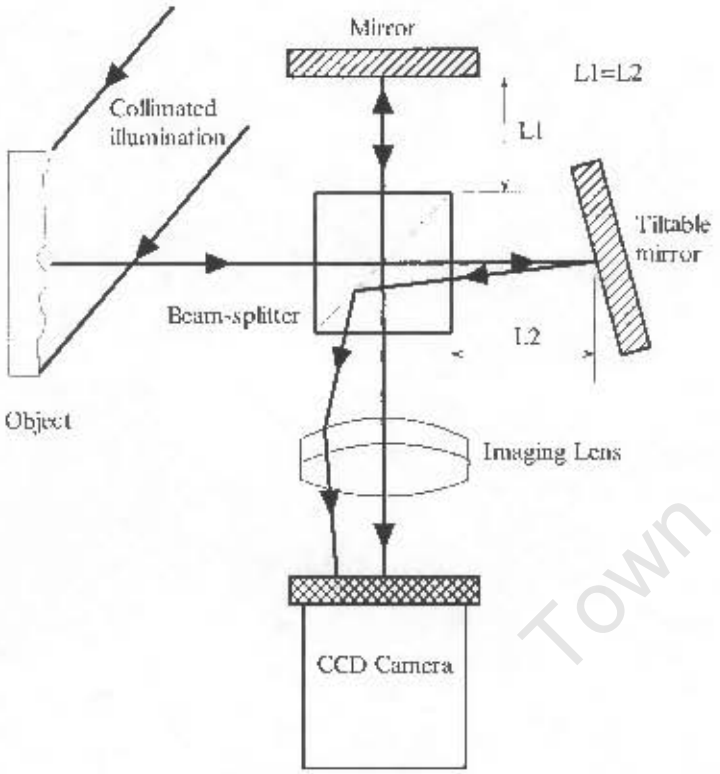

Figure 2.1: Path of a ray of light in a Michelson interferometer

The initial step in Digital Shearography is to capture a speckle pattern or image of the unstressed object, which is digitized and stored as a reference image. The intensity of light at any point on the speckle image of the unstressed object can be described mathematically by the following equation:

$$I_a = 2A^2\left[1+\cos\left(\theta(x+\delta x, y)-\theta(x, y)\right)\right] \tag{2.1}$$

Where A is a complex amplitude of the combined wavefronts and is a function of the object illumination and δx is the magnitude of shear. Furthermore, $\theta(x, y)$ and $\theta(x+\delta x, y)$ represents the phase in two object points that, due to shear, will correspond to the same image position. The object is then stressed by either mechanical, pressure or thermal methods. Stressing of the object causes the relative displacement between two points on the surface of the object to change, which in turn causes the laser path length to change. This

change of path length then alters the density distribution of the speckle pattern and the intensity can be expressed by the following equation:

$$I_b = 2A^2\left[1+\cos\left(\left(\theta(x+\delta x, y)-\theta(x, y)\right)+\Delta\phi\right)\right] \tag{2.2}$$

The variable $\Delta\phi$ in equation (2.2) represents the phase difference occurring due to the object being stressed. The speckle image, of the stressed object, is then digitized and stored. The phase difference $\Delta\phi$ can be extracted by either adding or subtracting the reference image from the stressed object image, described by equations (2.1) and (2.2) respectively. The software used in this investigation subtracts these two equations, which results in an interferogram with an intensity distribution as follows (the steps leading up to equation (2.3) are provided in appendix B):

$$I_r = I_a - I_b = 4A^2 \sin\left(\left(\theta(x+\delta x, y)-\theta(x, y)\right)+\frac{\Delta\phi}{2}\right)\sin\frac{\Delta\phi}{2} \tag{2.3}$$

The interferogram produced by equation (2.3) above maps the phase contours, which consist of alternating "zebra like" black and white fringe patterns. This is due to areas of pixel intensity correlating or decorrelating, when the two image images are subtracted, to form the interferogram. Correlation will take place when the phase difference is as follows:

$$\Delta\phi = 2n\pi \quad \text{where } n = 0, 1, 2,\ldots\ldots \tag{2.4}$$

This condition corresponds to the dark fringes on the interferogram. In contrast, decorrelation will take place when the phase difference is as follows:

$$\Delta\phi = (2n+1)\pi \quad \text{where } n = 0, 1, 2,\ldots\ldots \tag{2.5}$$

This condition corresponds to the bright fringes on the interferogram. The fringes can be modeled by the following mathematical equation:

$$\Delta\phi = \frac{4\pi}{\lambda}\left(\frac{\partial d}{\partial x}\right)S \tag{2.6}$$

Where $\Delta\phi$ is the correlation phase, $\frac{\partial d}{\partial x}$ is the rate of surface displacement, S is the magnitude of shear (i.e. the distance between common points that are sheared) and λ is the wavelength for laser light. The above equation shows that the correlation fringes represent lines of constant displacement rates, where $\Delta\phi$ is constant. The sensitivity of the interferometer can be varied by increasing or decreasing the angle of shear and thereby, varying the magnitude of shear (S). Therefore it can be seen from equation (2.6) that the greater the magnitude of shear, the larger the phase difference $\Delta\phi$, which therefore increases the sensitivity of the interferometer. If the phase difference in equation (2.6) is replaced by equation (2.4) then the spacing between adjacent fringes as a function of the displacement gradient can be obtained and is described by equation (2.7).

$$\frac{\partial d}{\partial x} = \frac{n\lambda}{2S} \quad \textit{Where } n = \textit{no of fringes} \tag{2.7}$$

This equation proves that for a given surface area, an increase in displacement gradient will produce a corresponding increase in the number of fringes. The Shearographic NDE equations and their derivations can be found in "*Holographic and Speckle Interferometry*" by R. Jones and C. Wykes[20].

2.1.2 Coherence Length and Unbalanced Interferometers

Laser light although assumed to be monochromatic, is only monochromatic until a finite spatial extent. Furthermore the coherence length is defined as the distance over which a laser beam will approximate a sine wave of fixed frequency.

Laser light, from a real source, traversing a Michelson interferometer of equal arm length (i.e. distance between the two mirrors and beam-splitter are equal) results in the interferometer

producing fringes of excellent contrast[21], as shown in figure 2.2(a). Areas of the fringe pattern containing dark fringes due to destructive interference will be perfectly black. The visibility of a fringe pattern, which is a measure of the contrast, is described by the equation (2.8) below.

$$V = \frac{I_{max} - I_{min}}{I_{max} + I_{min}} \tag{2.8}$$

Where I_{max} and I_{min} are the maximum and minimum values of the intensity of the fringes. Fringes in figure 2.2(a) have an I_{min} value of zero, which makes the visibility V unity. This is the maximum value of V; therefore maximum contrast is achieved. If one of the arms of the interferometer were to be extended by moving mirror M_1 by a distance of $\frac{\Delta l_1}{2}$ the visibility V would decrease in magnitude and the fringe pattern's contrast would become moderate as shown in figure 2.2(b). Further translation of mirror M_1 to a distance of $\frac{\Delta l_2}{2}$ would cause the fringe visibility to decrease even further until no fringes will be visible due to V tending to zero. The degradation of fringe visibility with increase in path length of a Michelson interferometer is a measure of temporal or longitudinal coherence of a light source. The coherence length of a light source is generally defined as the distance in which the fringe visibility V falls to $1/e^2$ (where e =2.718). In interferometry long coherency lengths are desirable. Helium-Neon lasers have a coherency length of approximately 20cm. However; the coherency length can be increased to seven meters. This can be accomplished by modifying the laser to produce a single axial mode. The disadvantage of modifying the laser is that it causes a loss in laser power.

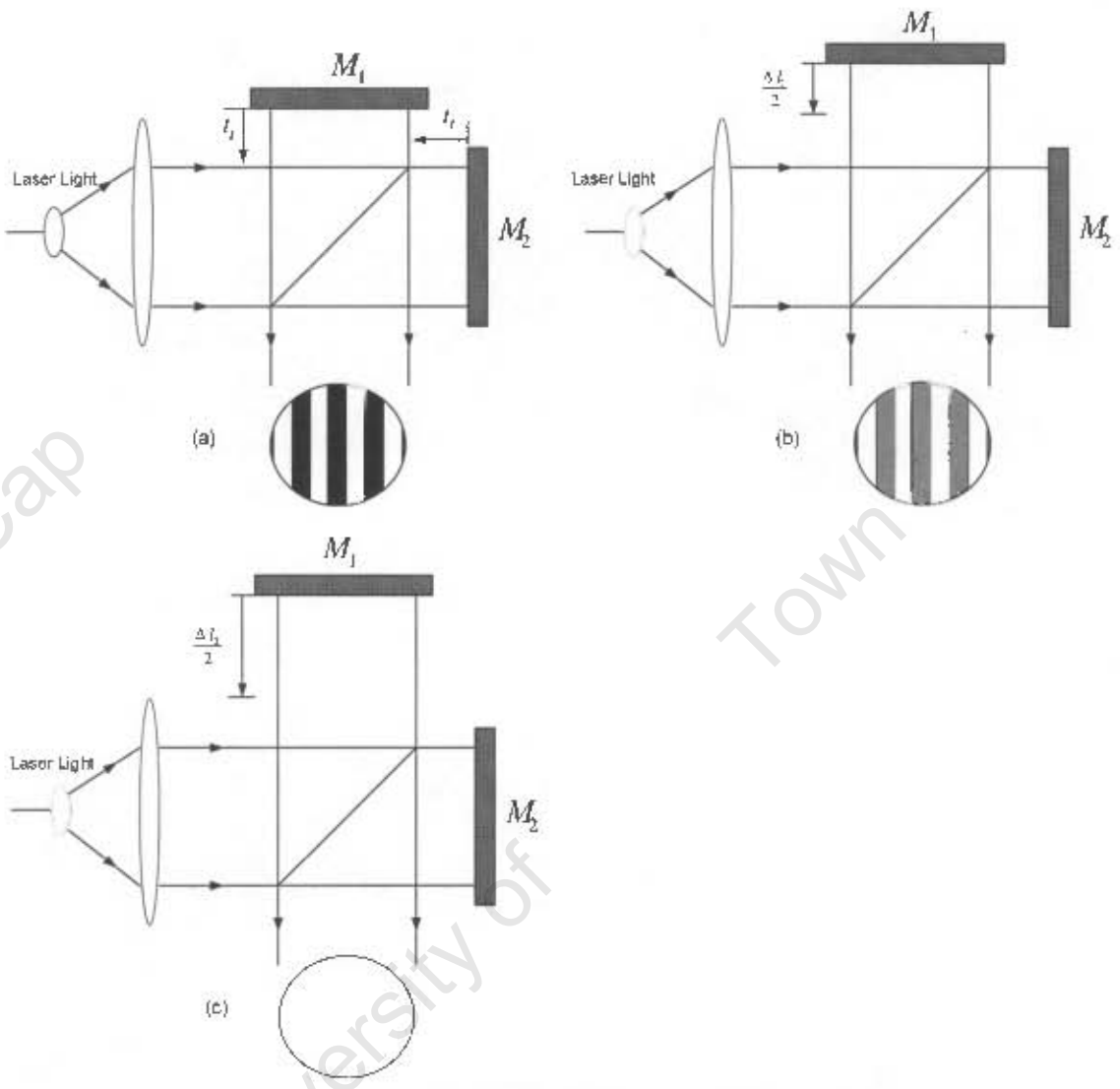

Figure 2.2: Temporal coherence effects displayed by a Michelson Interferometer[21]

To summarize, the path length of the two arms of the Michelson interferometer should be kept equal due to laser light having a specific coherence length, which affects the visibility of fringe patterns.

2.1.3 Limiting factors in Interferometry

This section points out the limiting factors concerning the measurement of displacement gradient using Shearographic NDE.

2.1.3.1 Sensitivity

The minimum displacement that can be measured by an interferometer depends on the speckle size. The displacement of the object must be such that the resulting displacement of the speckle pattern in the image plane is greater than the speckle size in that plane. Equation (2.9) shows the minimum out-of-plane displacement required to produce fringes.

$$d_{min} > {}^{q_s}/_{m} \tag{2.9}$$

Where q_s is the speckle size and m is the magnification of the viewing system. Since the magnification of a viewing system is usually unity to prevent lens aberration and fringe errors equation (2.9) can be written as follows:

$$d_{min} > \frac{1}{2}\lambda\left({}^{f}/_{a}\right) \tag{2.10}$$

Where (f) is the focal length and (a) is the aperture diameter of the lens making up the viewing system. It can be seen from equation (2.10) that an increasing aperture size allows the interferometer to detect smaller displacements. However, pixel intensity is also dependant on aperture size and if the aperture of the viewing system is too large it will cause the pixel intensity of the CCD detector to become saturated and therefore record the wrong measurement (Pixel intensity is discussed further in section 2.1.3.2). Furthermore, speckle size and hence minimum displacement is limited by the resolving power of the CCD detector known as the detector cut-off point[1]. Therefore larger speckle (caused by smaller apertures) are easier to resolve making fringes clearly visible.

The total number of fringes (i.e. the maximum displacement) that can be observed using an interferometer is limited by the speckle size. It has been proven by Jones and Wykes[20] that the ratio of fringe spacing to speckle size must be greater than 5 for fringes to be observed. This means that maximum displacement that can be measured by an interferometer of an object under inspection is limited by this factor.

2.1.3.2 Pixel Intensity

A measurement, of a camera pixel intensity, can vary from useful to incorrect depending on whether the pixel signal is very low, modulating or totally saturated. The intensity of a camera pixel is defined by the following equation:

$$I = I_O + I_M \cos\phi \tag{2.11}$$

Where I_O is the background intensity, I_M is the modulation intensity and ϕ is the phase. If these variables are known, then it is possible to tell whether the measurement of a pixel is valuable or not. For example if the signal exceeds the pixel saturation intensity I_{sat}, then the measured intensity will be wrong. Furthermore if the modulation intensity is too low, then it will be impossible to extract the phase from the intensity measurement. Therefore a pixel with high modulation intensity I_M and a total intensity I, which is below saturation, will contribute to a 'good' displacement gradient measurement. This means that there is an optimum amount of laser light required during an inspection and this can be controlled varying the amount of light that enters the CCD camera.

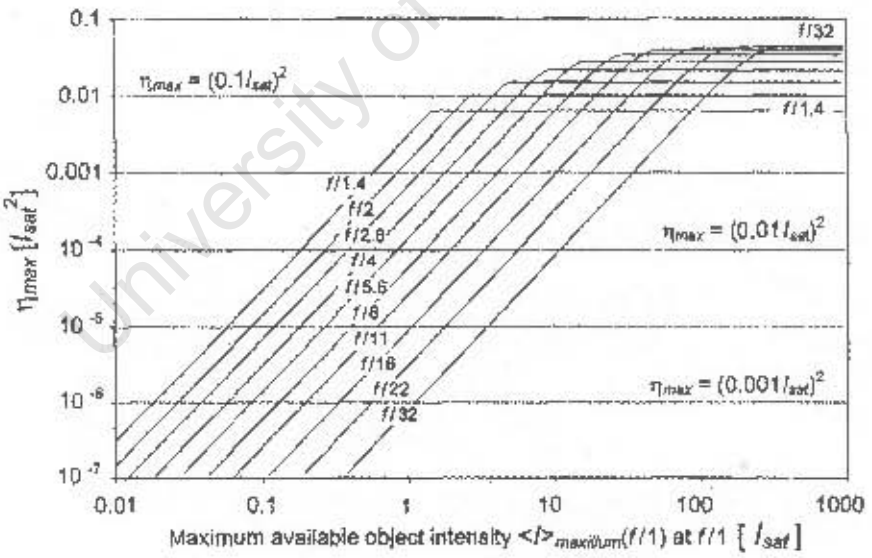

Figure 2.3: Efficiency versus maximum available object intensity[22]

Measurements taken under optimal conditions will lead to the highest number of good pixels and the least number of bad pixels. The quality of measurement can be defined by the measurement efficiency η, which takes into account all the camera pixels using weights related to the pixel quality. The weights are a function of the pixel modulation intensity I_M, background intensity I_O and phase ϕ. Therefore the right combination of these weights will produce high quality pixel measurement and thus allow the system to be optimized. Figure 2.3 is a graph of efficiency η versus maximum available object intensity (i.e. maximum available light). It can be seen from the graph that for every aperture number, the efficiency curve increases linearly until saturation sets in and at this point is where the highest possible efficiency for a particular aperture size is reached. Furthermore it can also be seen that once the optimum efficiency is reached for a particular aperture number, increasing the laser power will be fruitless since the efficiency will not increase. This means that when there is limited laser power large apertures are more efficient. However, if higher laser powers are available then smaller apertures are more efficient. Rastogi[22] explains these optimization criteria in much greater detail whilst this paragraph summaries the results of his study.

2.1.3.3 Object size

The maximum object area that can be inspected during a single inspection is not dependant on the field of view of the viewing system. Although the field of view does affect the amount of the object that can be seen at one time it is usually the laser power that is the limiting factor[20]. In a laboratory, laser power can easily be increased by using a high voltage laser that is water cooled. However in portable interferometry laser power is very limited and so is the size of the object area that can be inspected.

2.2 Phase-Stepped Shearography

2.2.1 Principles of Phase-stepping

The following sections describe the analysis of speckle patterns and the resulting phase map that is manifested when using Phase-Stepped Shearographic NDE. Filtering is discussed as means of substantially improving the phase map image quality.

2.2.2 Phase-Stepping

Phase-stepping is derived from the intensity integration method[23] and requires a minimum of three measurements (i.e. speckle patterns) to solve for three unknowns. However four measurements are more commonly used. Each micro displacement of the calibrated piezo-electrically driven mirror initiates phase steps of $\pi/2$ increments, which is equivalent to changing the path length of the laser beam by a quarter of a wavelength as shown in figure 2.4.

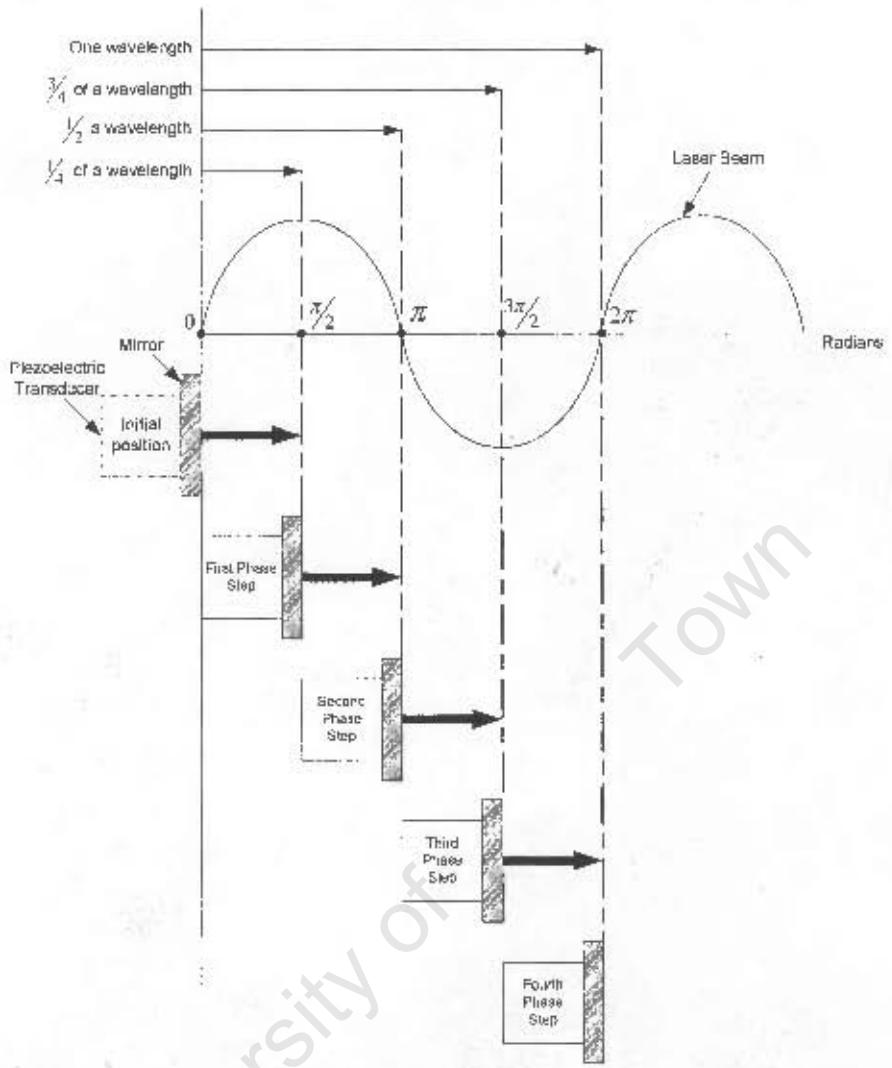

Figure 2.4: Motion of the piezo-electrically driven mirror relative to a monochromatic laser beam

It can be seen from figure 2.4 that a monochromatic laser beam is sinusoidal in nature and that as the piezo-electrically driven mirror is displaced from it initial position it changes the laser beam path length. First by a quarter of a wavelength, second by half a wavelength, third by three quarter of a wavelength and finally at the fourth phase step the beam path length has been changed by a full wavelength. At this point the piezo-electrically driven mirror reverts back to its initial position.

After each phase-step a speckle pattern is "grabbed" by the image processing system. The measured intensity $I_i(x,y)$ of the speckle pattern, at any given co-ordinate (x,y), can be described by the following equation[24]:

$$I_i(x,y) = I_{BM}(x,y) + I_{mp}(x,y)\cos(\phi(x,y) + i\alpha) \qquad i = 1,2,\ldots,N \qquad (2.12)$$

Where, $I_{BM}(x,y)$ is the background intensity, $I_{mp}(x,y)$ is the modulation intensity, $\phi(x,y)$ is the phase difference between the object and reference beam and α is the relative phase step (i.e. $\pi/2$). When four images are grabbed (i.e. when i goes from 1 to 4), the process is known as the 4-bucket system[25].

Since $\cos\left(\theta + \frac{\pi}{2}\right) = -\sin\theta$ *and* $\cos(\theta + \pi) = -\cos\theta$

$$I_1(x,y) = I_{BM}(x,y) - I_{mp}(x,y)\sin(\phi(x,y)) \qquad (2.13)$$

$$I_2(x,y) = I_{BM}(x,y) - I_{mp}(x,y)\cos(\phi(x,y)) \qquad (2.14)$$

$$I_3(x,y) = I_{BM}(x,y) + I_{mp}(x,y)\sin(\phi(x,y)) \qquad (2.15)$$

$$I_4(x,y) = I_{BM}(x,y) + I_{mp}(x,y)\cos(\phi(x,y)) \qquad (2.16)$$

Equation (2.12) produces four trigonometric equations as described by equations (2.13-2.16), which can be solved to eliminate the unknown background intensity $I_{BM}(x,y)$. The phase difference can only be calculated after the background intensity $I_{BM}(x,y)$ is eliminated as discussed in the next section.

2.2.3 Calculation of the Phase Change Distribution

The technique described above provides a wrapped phase distribution, $\phi(x,y)$, which still contains the spatially random phase distribution described by the background intensity $I_{BM}(x,y)$. The background intensity $I_{BM}(x,y)$ is removed by subtracting equation (2.14) from

equation (2.16) and equation (2.13) from equation (2.15) which yields equation (2.17) and (2.18) respectively.

$$I_4 - I_2 = 2I_{mp}(x,y)\cos(\phi\ (x,y)) \tag{2.17}$$

$$I_3 - I_1 = 2I_{mp}(x,y)\sin(\phi\ (x,y)) \tag{2.18}$$

The phase can be described as a function of the four intensities by the following equation [24,25]:

$$\phi(x,y) = \arctan\left(\frac{I_3(x,y) - I_1(x,y)}{I_4(x,y) - I_2(x,y)}\right) \tag{2.19}$$

The phase difference $\psi(x,y)$ can then be calculated by using the following equation:

$$\psi(x,y) = \phi_b(x,y) - \phi_a(x,y) \tag{2.20}$$

Where, $\phi_b(x,y)$ and $\phi_a(x,y)$ represent the phase before and after deformation respectively. The inverse tangent in equation (2.19) ranges between $-\pi/2$ to $\pi/2$ but does not provide the true phase since values after $\pi/2$ till $3\pi/2$ are not within the limits. Taking into consideration the sign of the sine and cosine solves this problem. If the cosine is negative, then it will be in the second and third quadrant and π is added to the arctangent value to get the correct phase.

The phase difference $\psi(x,y)$ is then calculated using equation (2.20) and is limited to the range of -2π to 2π and thus contains 4π discontinuities. This range is then shortened so that the limit is from 0 to 2π since a wave repeats itself after every 2π. Taking the absolute of the phase difference is one method of shortening the range but this method produces noise, a second and better method is to add 2π to the negative result of the subtraction of the two waves.

Once the true phase difference is calculated, using the image processing software, a phase map will be produced consisting of fringes ranging from black to white and then suddenly changing back to black. This "saw tooth pattern" continues throughout the image. This drastic change occurs due to the phase difference increasing towards 2π and then jumping back to zero when the limit of 2π is reached. This means that in the final image black represents the smallest phase difference and white the largest. The regions where these discontinuities occur are called 2π discontinuities and they are the main characteristics of phase stepping in helping to determine the relative direction in which deformation takes place.

2.2.4 Filtering of Phase-Difference maps

Once the phase difference is calculated for the individual pixels in an image and a phase map is produced, a common way to improve visibility of the fringes is to filter it. Speckle noise and 2π discontinuities in phase fringe patterns are characterized by a high spatial frequency so using a low-pass filter will not only reduce noise but also smear the discontinuities, which are vital information[26].

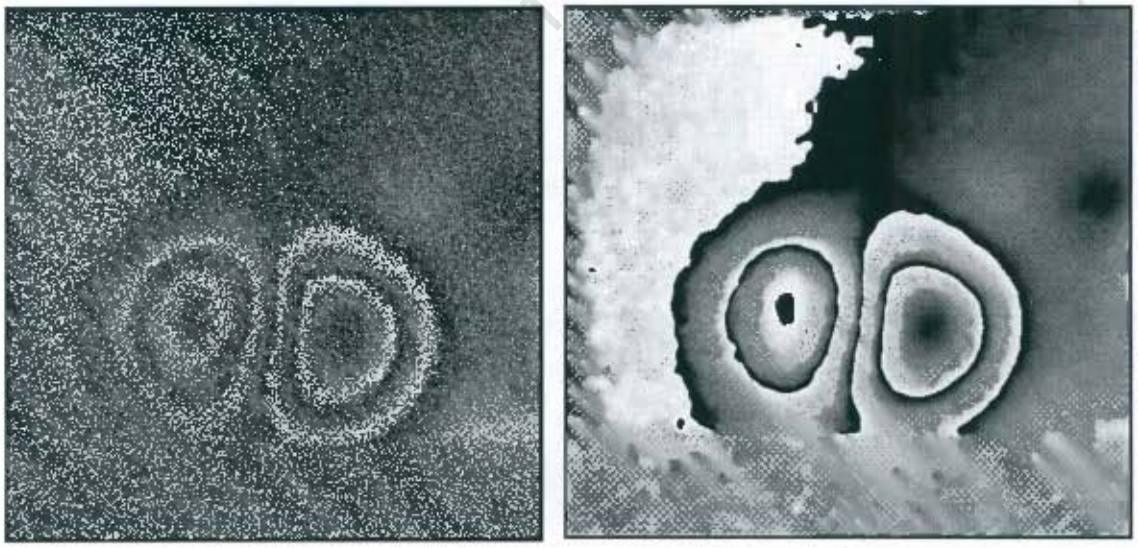

(a) (b)

Figure 2.5: Comparison of an unfiltered and filtered phase fringe pattern

The solution to this problem is to revert back to sine and cosine of the wrapped fringe patterns in equation (2.19) since these trigonometric functions are continuous unlike the tangent function. The sine and cosine are then filtered separately using an average filter, which takes the average value of a group of neighboring $n \times n$ pixels for each pixel in the image, where n is an odd integer number. The filtered sine and cosine are then put back into equation (2.19) so that the phase difference can be recalculated. This process of filtering can be repeated up to 30 times. Figure 2.5(a) shows an unfiltered Phase-stepped image and figure 2.5(b) shows a filtered phase map. It can be seen from figure 2.5, that when a 3×3 average filter is applied the noise is reduced considerably.

2.2.5 Summary

The initial step in Phase-Stepped Shearographic NDE is to extract the phase, $\phi(x,y)$, by measuring the intensity of the speckle at known phase steps. The phase difference, $\psi(x,y)$, can then be calculated by subtracting the unstressed image from the stressed image, which will produce a phase map or a filtered phase map. The flowchart in figure 2.6 illustrates the process.

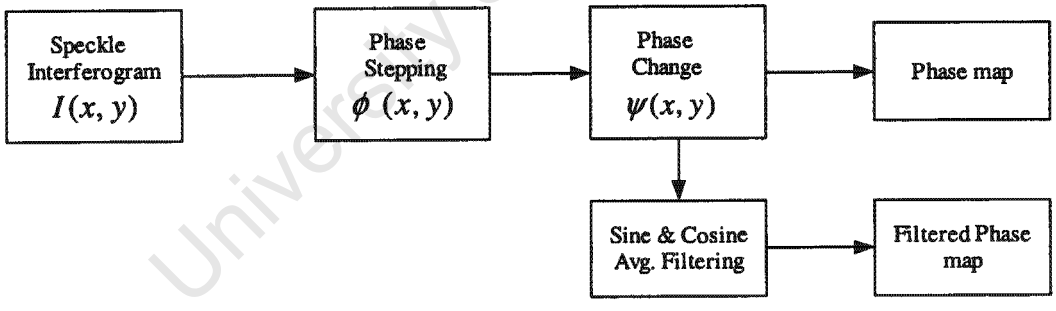

Figure 2.6: Sequence of calculations in Phase-stepping

3. BACKGROUND INFORMATION ABOUT OPTICS

Designing a compact Shearographic prototype requires an in-depth knowledge of optics. All the information concerning optics is contained in appendix A. This section is a summary of where the information can be found in appendix A.

Section 1.1 in appendix A outlines the fundamentals of optics and introduces the reader to the planes and points that characterizes a lens. Section 2.2 in appendix A discusses the formation of images when using a converging lens. There are two ways of finding the position and magnification of an image namely by ray tracing or by applying the thin lens and magnification equations. Only the applications of the thin lens and magnification equations are discussed in section 2.3 of appendix A.

Modulation transfer function (MTF) is discussed in section 2.4 which is an extremely important parameter influencing the resolving power of an imaging lens. MTF plays a key role in providing well contrasted fringe patterns as it measures the ability of a lens to transfer contrast at varying resolution levels.

Finally in section 2.5, aberrations are discussed as they also play an important role in image quality. Aberrations are intrinsic shortcomings of a lens and cannot be totally eliminated even if the lens is made from the best glass and is free from defects. There are several different aberrations, each having a different effect on the image quality.

4. CONCEPTUAL DESIGN

Three design concepts were considered as an approach to designing a compact Shearographic prototype. The subsequent sections discuss these design concepts as well their advantages and disadvantages with regard to the design requirements of this thesis (as discussed in section 1.2.2).

The design concepts below vary only by using different configurations of lenses and different types of lenses. The type of shearing optics used in interferometry is very specific and therefore the type of beam-splitter and mirrors will be the same in all three design concepts. The CCD camera and CCTV lenses are also standard in all three design concepts; section 4.1 gives a brief description of these components. For background information about the fundamentals of optics, formation of images when using a converging lens, MTF and aberrations, refer to appendix A.

4.1 Standard Components

4.1.1 CCTV (Closed Circuit Television) Lens

Three interchangeable CCTV lenses where used during this thesis. Their use depended on object size and position. Also one of the design requirements is that the attachment of different power CCTV lenses must be possible. These CCTV lenses were used to check that the device could in fact use interchangeable CCTV lenses.

Figure 4.1 is a picture of the three CCTV lenses used during testing. All three CCTV lenses are $\frac{2}{3}$ inch format manual iris lenses. Figure 4.1(a) is a picture of 8.5mm focal length Cosimcar CCTV lens with a maximum aperture ratio of 1:1.5 and minimum object distance of 0.2m. Figure 4.1(b) is a picture of a 6mm focal length Cosimcar CCTV lens with a maximum aperture of 1:1.2 and a minimum object distance of 0.2m. Figure 4.1(c) is a picture of 17.5 to 105mm focal Fujinon CCTV zoom lens with a maximum aperture ratio of 1:18 and a minimum object distance of 1.3m.

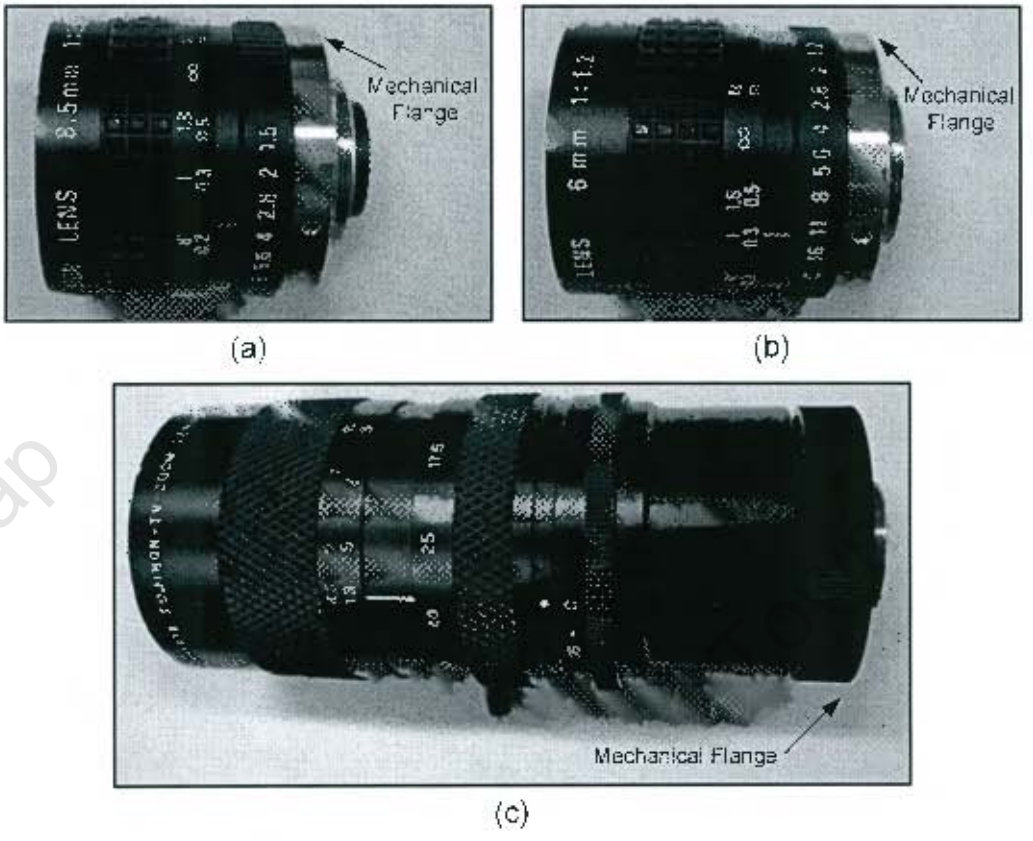

Figure 4.1: (a) Picture of an 8mm CCTV lens, (b) Picture of a 6mm CCTV lens and (c) Picture of a 17.5 – 105mm CCTV zoom lens

In order to incorporate the image shearing optics between the camera's CCD and the CCTV lens one needs to examine how an image is formed in a normal arrangement (as illustrated in figure 4.2). If an object is placed in front of a CCTV lens it will be imaged at its focal plane. The distance between the CCTV lens's mechanical flange and its focal plane is exactly 17.526mm. All CCTV lenses are built to this specification so that when any CCTV lens is attached directly to a CCD Camera its focal plane will lie in the same plane as the detector of the CCD Camera. In this way the image is always captured at the right focus. All lenses have two principal points namely a primary and a secondary principal point. The distance between the secondary principal point and the focal point determines the focal length of a CCTV lens.

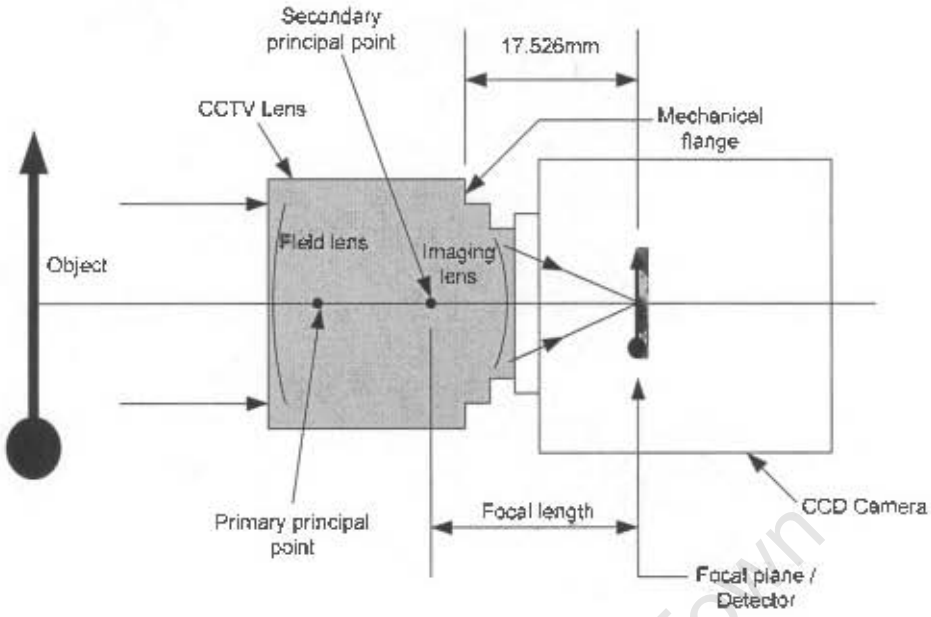

Figure 4.2: Image formation of a CCTV lens

CCTV lenses are usually made up of at least three lenses where the lens closest to the object is known as the field lens while the lens furthest from it is known as the imaging lens. Movement of the center lens, in the horizontal direction, allows an object within a certain range to be continuously focused at the focal plane. If the center lens remains unchanged as the object moves further away or closer to the CCTV lens then its image will not lie on the focal plane. Furthermore the image would move in the horizontal direction according to the position of the object which is governed by the thin lens equation.

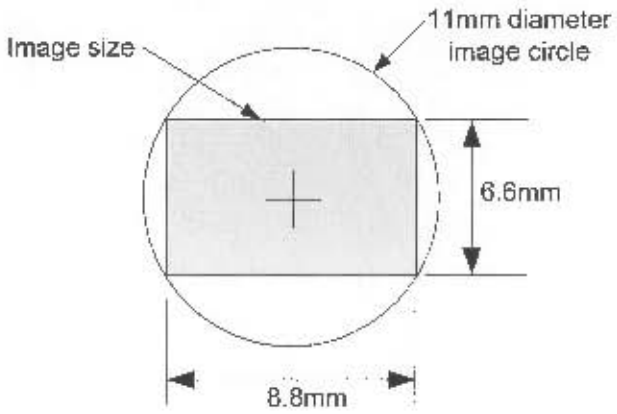

Figure 4.3: Image circle and detector size

It can be seen from figure 4.2 that the image produced is smaller than the object and that it is correctly orientated. The image of the object is reduced (i.e. magnified) in size at the focal plane so that it matches the detector size and is formed within an 11mm diameter circle known as the image circle (as shown in figure 4.3). The detector size in figure 4.3 is an 8.8mm by 6.6mm rectangle which is known as a $\frac{2}{3}$ inch detector. CCD cameras and CCTV lenses come in many different sizes therefore it is important not to mismatch them. Table 4.1 is an image size chart showing the correct match up of detector and image circle.

Table 4.1: Image size chart

Image Sensor	Image Circle	Horizontal	Vertical
Quarter inch	4.0mm	3.2mm	2.4mm
One third inch	6.0mm	4.8mm	3.6mm
Half inch	8.0mm	6.4mm	4.8mm
Two third inch	11.0mm	8.8mm	6.6mm
One inch	16.0mm	12.8mm	9.6mm

If a 1 inch CCTV lens is matched up with a $\frac{2}{3}$ inch detector there will be no problem with the final image since the image circle will be 16mm in diameter and larger than the detector.

However if a $\frac{1}{2}$ inch CCTV lens is matched with a $\frac{2}{3}$ inch detector, then a dark ring will form around the edges of the image, known as mechanical vignetting. This is because the image circle, which is 8mm in diameter, will be smaller than the detector size. The CCD camera used in this thesis has a $\frac{2}{3}$ inch detector and therefore as mentioned earlier only $\frac{2}{3}$ inch CCTV lenses will be used.

4.1.2 CCD (Charged-Couple Device) Camera

The camera is a Pulnix TM-1320-15CL CCD camera with a $\frac{2}{3}$ inch detector, a resolution of 1300 x 1030 and a frame rate of 15 frames per second. The camera has a height of 44mm, a width of 44mm and a length of 63.8mm. Figure 4.4 is a picture of the CCD camera and a schematic of the camera can be found in appendix C.

Figure 4.4: Picture of a CCD camera

4.1.3 Beam-splitter

The beams-splitter is a Tech Spec non-polarizing 25mm "cube" beam-splitter and is manufactured from BK7 glass. It has a laser wavelength range of 430-670nm with 45% ± 5% transmittance, less than 10% absorption and less than 6% polarization. Figure 4.5 is a picture of a 25mm cube beam-splitter.

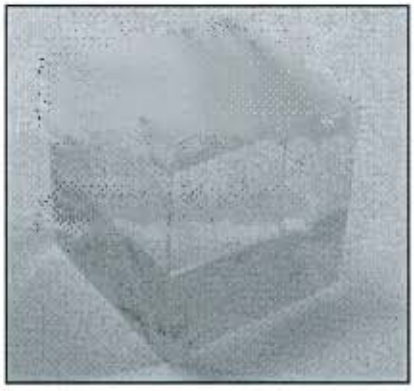

Figure 4.5: A 25mm beam-splitter

4.1.4 Mirror

The mirrors are 25mm by 25mm Tech Spec $\frac{1}{4}$ wave first surface mirrors with an enhanced aluminum coating and a reflectance of 95% + for laser wavelengths of 450-650nm.

4.1.5 Miniature Angle Mirror Mount

The miniature angle mirror mount is designed for a 25mm by 25mm mirror and has a resolution of 0.015 inches per revolution. The angle mount is pictured in figure 4.6 and is manufactured from aluminum-stainless steel.

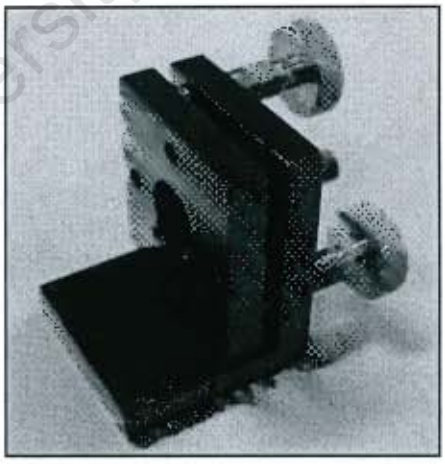

Figure 4.6: A miniature angle mount

4.1.6 Piezo-electrically Driven Mirror

The Piezo-electric transducer uses AHV 150 piezo-electric crystals which are unipolar and have an applied voltage of 0-150 volts causing a displacement of 0-6 micrometers respectively. The Piezo-electrically driven mirror is pictured in figure 4.7.

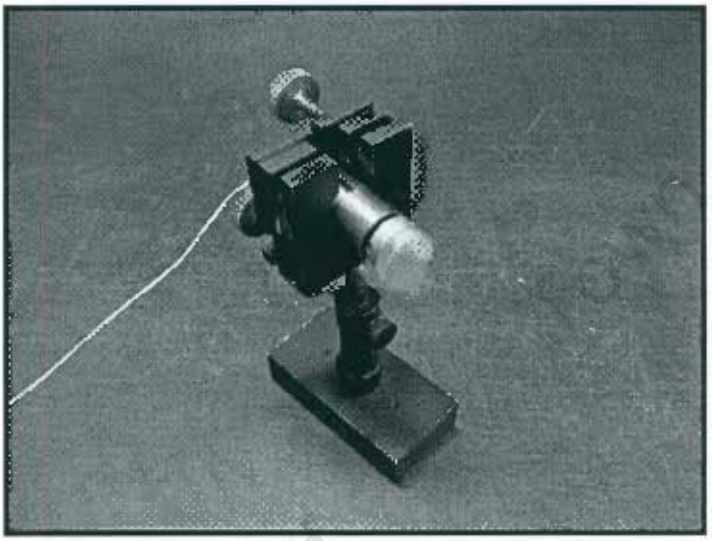

Figure 4.7: Picture of the piezo-electrically driven mirror

4.2 Design Concept A

Design concept A makes use of a single double convex lens which is placed between a CCTV lens and CCD camera in order to engineer enough space to fit the shearing optics. Figure 4.8 illustrates how design concept A works. It can be seen that the CCTV lens creates an image of the object at its focal plane (also called image plane A in figure 4.8) as mentioned earlier.

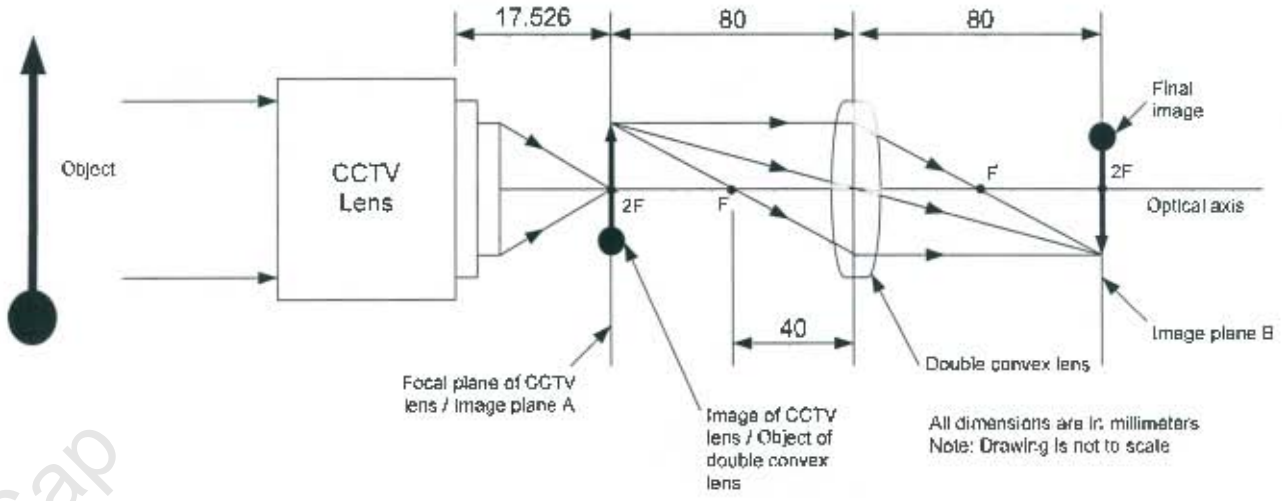

Figure 4.8: Design concept A excluding the shearing optics

This image then becomes the object of the double convex lens which is positioned a distance of 80mm to the right of image plane A. This distance is equivalent to twice the focal length of the double convex and therefore an inverted image will be formed at image plane B. The position of the image (i.e. image produced by the double convex lens) can be calculated using the thin lens equation. If the object distance (d_o) is equal 80mm and the effective focal length (f) is equal to 40mm for the double convex lens then the image distance (d_i), from the center of the double convex lens, can be calculated as follows:

$$\frac{1}{d_o}+\frac{1}{d_i}=\frac{1}{f}$$

$$\Rightarrow \frac{1}{d_i}=\frac{1}{f}-\frac{1}{d_o}=\frac{1}{40}-\frac{1}{80}=\frac{1}{80}$$

$$\therefore d_i = 80mm$$

This means that the final image will be real (referring to table 1.1 in appendix A) and therefore it will be formed 80mm to the right of the double convex lens at image plane B. This lens configuration therefore leaves enough space between the lens and image plane B to fit the shearing optics as shown in figure 4.9. It can be seen that the CCD camera detector is

placed where image plane B would have been. Furthermore the distance traveled from the center of the lens through the Michelson interferometer and up to the detector sums up to 80mm.

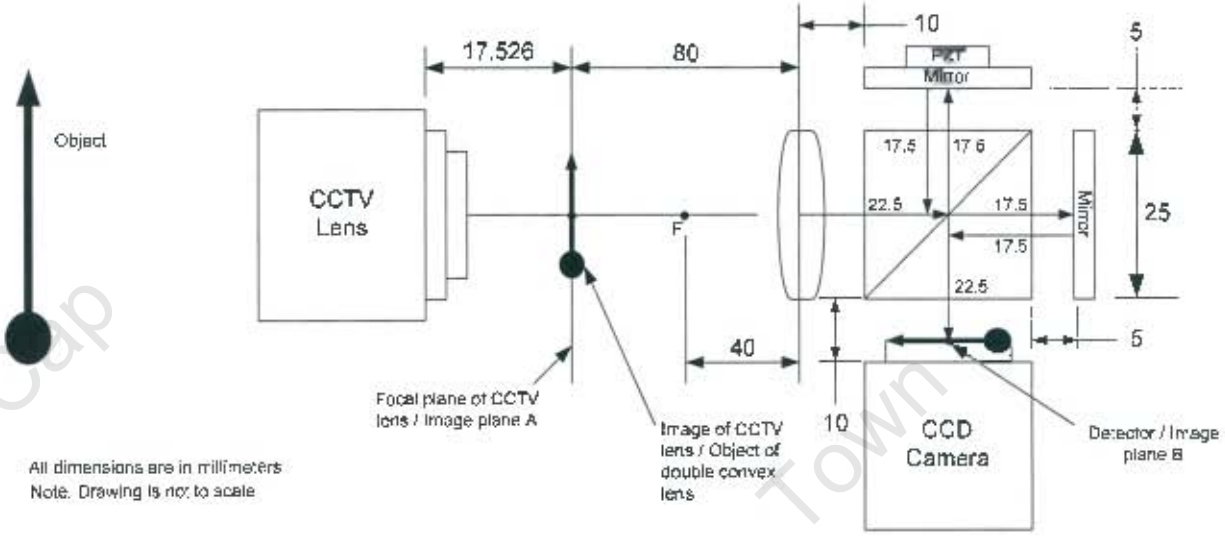

Figure 4.9: Design concept A including the Michelson interferometer

The magnification (m) of the image can then be calculated by using the magnification equation, since both the object and image distances are known.

$$m = -\frac{d_i}{d_o} = \frac{80mm}{80mm} = -1 \tag{5.2}$$

Referring to table 1.1 in appendix A, this means that the image is inverted due to the sign of m being negative, which implies that the CCD camera will capture an image that is upside-down. However this problem can be easily solved by fitting the CCD camera to the device upside-down, therefore an upright image will be displayed on the monitor. The magnitude of the magnification (m) is 1 which means that the magnification ratio is 1:1. Therefore no change in magnification has occurred.

A magnification ratio of 1:1 is important in that if the image were to be enlarged it would be bigger than the detector. Therefore only a small part of the image will be seen, bearing in mind that the CCTV lens has already reduced the image to the detector size. In contrast, if the image were to be further reduced in size, a black ring will form around the edges of the image captured by the CCD camera due to the image being smaller than the detector. Having a perfectly symmetrical optical system also has another advantage in that aberrations such as distortion, coma and lateral color are minimal.

Three different types of lenses were tested for this design concept namely; a 25mm diameter by 40mm focal length double convex lens, a 25mm by 30mm achromat and a 23mm by 40.3mm Hastings triplet. Each of these lenses were simulated in a computer program known as OLIVE (Optical Layout Including Video Elements) which was purchased from Edmund Optics. In the simulation (refer to appendix E for the printout of the simulation), each lens was placed at a distance of twice its focal length away from the object so that it would have a conjugate ratio (i.e. object distance:image distance) of 1:1. Therefore the magnification would also be 1:1. The program then performs real-time ray tracing to calculate the magnitude of spherical aberration, coma, astigmatism, field of curvature and distortion of each of the lenses. Table 4.2 shows the results of the three lenses, where the light blue indicates the lowest value and the light orange indicates the highest value for each aberration when the three lenses were compared.

Table 4.2: Three different lenses with the object at twice the focal length

Type of lens	Spherical aberration	Coma	Astigmatism	Field of Curvature	Distortion
25mm by 40mm Double Convex Lens	0.878	0.011	0.055	0.041	0.004
25mm by 30mm Achromat	0.694	0.197	0.089	0.059	0.006
23mm by 40.3mm Hastings Triplet	0.566	-0.039	0.039	0.045	-0.011

It can be seen that the achromat is the worst lens since it has the highest magnitude for three of the five aberrations. It should be noted that the absolute value of the aberration was taken

when the aberrations were compared, in that the sign of the aberration shows the direction of the aberration and is irrelevant since only the magnitude of the aberration is required. The double convex lens was chosen for this design concept because it had the lowest value for three of the aberrations; therefore it should project the final image with the best image quality.

4.3 Design Concept B

Design concept B also uses a double convex lens, however in this case the lens has an infinite/finite conjugate ratio. Figure 4.10 illustrates how this design concept works. It can be seen that the object is placed far away as compared to the focal length of the double convex lens. In this way, the rays from the object will be collimated when is reaches the lens which then projects an image of the object onto the CCD camera detector, positioned at the secondary focal point of the lens.

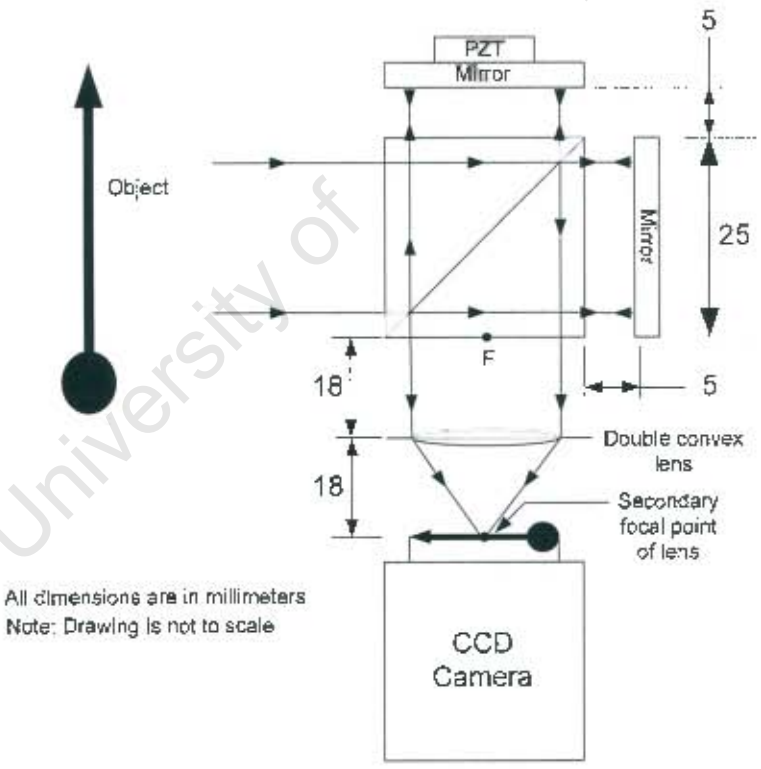

Figure 4.10: Design concept B

The advantage of this design concept is that it does not require a large diameter lens since the light is collimated and therefore lenses between 12-14mm in diameter could be used. Also the focal length should be as short as possible so that when an object is very close to the beam-splitter its rays will still be collimated.

Table 4.3: Three different types of lenses with an infinite/finite conjugate ratio

Type of lens	Spherical aberration	Coma	Astigmatism	Field of Curvature	Distortion
12mm by 18mm Double Convex Lens	0.6497	-0.3333	0.4279	0.4189	0.2318
12.5mm by 14mm Achromat	0.6677	2.2303	8.408	0.8917	38.5116
12.5mm by 20mm Hastings Triplet	0.2431	0.3793	0.6489	0.3875	2.5415

The following three lenses best met this criteria: a 12mm by 18mm double convex lens, a 12.5mm by 14mm achromat and a 12.5 by 20mm Hastings triplet. The three lenses were simulated in OLIVE using an infinite/finite conjugate ratio and the setup is shown in appendix E. Table 4.3 shows the results of the simulation were it can be seen that the double convex lens performs much better than the 12.5mm by 14mm achromat and the 12.5mm by 20mm Hastings triplet and hence was chosen for the design.

4.4 Design Concept C

Design concept C makes use of two Hastings triplets with the first lens working as a field lens and the second as an imaging lens. Figure 4.11 illustrates the optical setup of the system where it can be seen that the CCTV lens projects an image of the object onto its focal plane. This becomes the object of the field lens which is placed a distance of 33.9mm to the right of CCTV lens's focal plane from its primary vertex. The object rays then become collimated since the object is positioned at the primary focal point of the field lens. The collimated light then travels through the Michelson interferometer until it reaches the imaging lens. The latter

produces an image on the CCD camera detector since the detector is positioned at the secondary focal point of the imaging lens. A manual iris is placed in front of the field lens so that the modulation transfer function can be manipulated by changing the size of the iris.

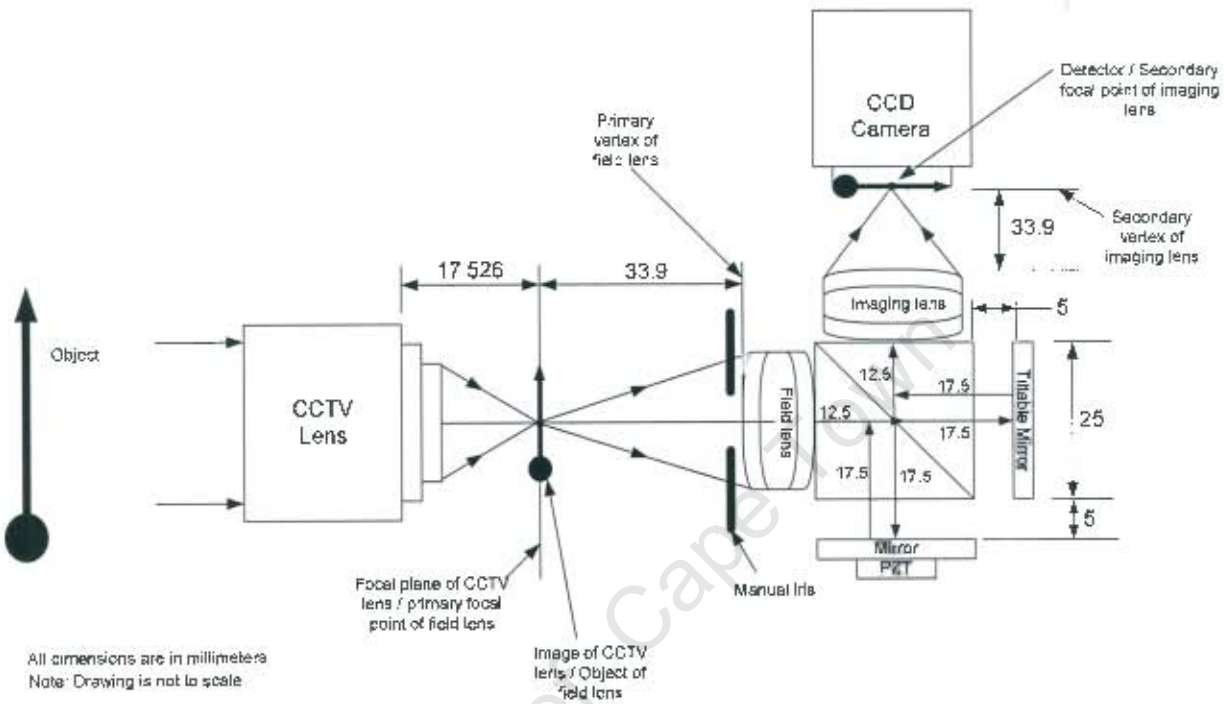

Figure 4.11: Design concept C

Table 4.4 shows the results of the OLIVE simulation for the three different types of lenses so that a lens with minimal aberrations can be found. Appendix E shows the optical setup of the simulation. It can be seen from the results that the Hastings Triplet performed best for all of the aberrations and hence was chosen for this design.

Table 4.4: Results from simulation for design concept C

Type of lens	Spherical aberration	Coma	Astigmatism	Field of Curvature	Distortion
25mm by 40mm Double Convex Lens	2.311	-1.417	1.345	0.329	-1.611
25mm by 30mm Achromat	1.723	1.406	3.093	0.738	6.307
23mm by 40.3mm Hastings Triplet	1.093	-0.711	0.811	0.308	-1.183

This optical setup has two advantages, firstly the magnification ratio between the two lenses is still 1:1 since two identical lenses are being used and therefore distortion, coma and lateral color are minimal. Secondly the light will not diverge or converge as it passes through the interferometer which could cause a loss of light. Furthermore, the design concept allows attachment of various focal length lenses so that adjustment of field of view and zooming is possible, also CCTV lenses have a built-in manual iris so the intensity of laser light can be controlled.

The distance between the lenses can be varied without affecting the position and focusing of the final image, since the rays are collimated. However the minimum distance between the lenses has to be 60mm so as to provide enough space for the Michelson interferometer. Three simulations were done, using the Hastings triplets, by varying the distances between them by 60mm, 70mm and 80mm so that the optimum distance can be found where the aberrations would be minimal (the results are shown in table 4.5).

Table 4.5: Results of simulation when the distances between lenses were varied

Type of lens	Distance apart	Spherical aberration	Coma	Astigmatism	Field of Curvature	Distortion
23mm by 40.3mm Hastings Triplet	60mm	1.093	-0.711	0.811	0.308	-1.183
	70mm	1.092	-0.826	1.093	0.308	-1.768
	80mm	1.092	-0.945	1.435	0.308	-2.577

It can be seen from the table that spherical aberration and field of curvature is not affected by the separation distance of the lenses. However, coma, astigmatism and distortion increase in magnitude as the separation distance increases. Therefore for best image quality the lenses should be positioned at 60mm apart.

4.5 Evaluation of the Design Concepts

In this section the design concepts are evaluated so that the best design concept can be selected. The advantages and disadvantages of each design concept will be discussed and finally a checklist will be drawn-up to establish if all the design requirements are met.

4.5.1 Design Concept A

The major problem in design concept A is that insufficient light travels into the CCD Camera which causes the resulting images to become dark and not well-contrasted. Although the minimum diameter of lens required for this design concept is 11mm (i.e. due to a $^2/_3$ inch CCTV lens, creating an image circle of that size) it is not adequate as a small lens does not transfer enough light. This results in a dark final image, which cannot be easily seen. Even a 25mm diameter lens is not large enough to collect sufficient light to make the image clearly visible. Bringing the lens closer to the image plane A will solve the problem in that the closer the lens is to the image plane, the greater the amount of light that is captured. This is due to the light converging at the focal point of the CCTV lens. However if the lens were to be brought closer to the CCTV lens it would require its focal length to be smaller. Therefore there will be a challenge in incorporating the shearing optics on the right of the double convex lens.

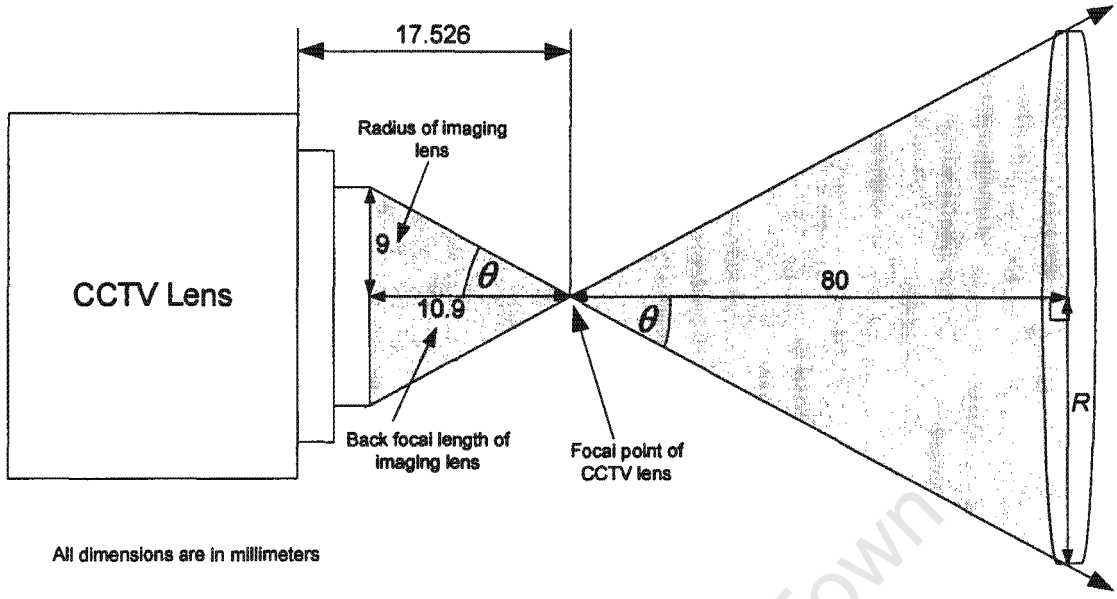

Figure 4.12: Schematic illustrating the cone of light

This problem is illustrated by figure 4.12 where it can be seen that all the light rays collected by a CCTV lens converge and pass through the rear focal point and then diverge as the light rays move right. This is known as the cone of light and it can be calculated by knowing the angle at which the marginal ray (i.e. the outer most rays) subtends the optical axis. This angle is known as the solid angle (θ) and bounds the cone of light exiting the imaging lens of the CCTV lens. The solid angle (θ) can be calculated as follows:

$$\theta = \arctan\frac{radius\ of\ imaging\ lens}{back\ focal\ length\ of\ imaging\ lens} = \arctan\frac{9mm}{10.9mm} = 39.5^{o}$$

The radius of a lens placed 80mm to the right of the focal point can then be calculated such that it intercepts the cone of light and hence allows 100% transmission of light to be achieved. The radius of a lens required to perform this task is denoted as R in figure 4.12. The radius (R) can be calculated as follows:

$$(R) = (\textit{Distance of lens from focal point})(\tan\theta) = (80mm)(\tan 39.5) = 66mm$$

Therefore it can be seen that for 100% transmission of light to take place, a lens diameter of 132mm is required which results in a 25mm diameter lens transmitting only 19% of the light. It should be noted that an 8.5mm focal length CCTV lens was used in this example and that the cone of light will vary slightly with varying focal length. Using a larger diameter lens would increase the percentage of light transmitted but would require the shearing optics to be made larger so that light captured by the double convex lens will not be cut out by the mirrors and beam-splitter due to them being smaller than the lens. This would make the prototype larger and therefore it is disadvantageous. The only viable option is to use a higher power laser so that object illumination can be increased. However a higher power laser requires a larger power supply. This makes the prototype heavy and bulky which is a disadvantage in terms of portability. Table 4.6 lists the design requirements versus the performance of concept design A.

Table 4.6: Check list of the design requirements for design concept A

Design Requirement	Check List
Design a compact Michelson type shearing interferometer	✓
Place the shearing optics between the CCD camera and zoom lens so that the field of view can be increased	✓
The overall dimensions of the interferometer and the CCD camera should be approximately the size of an A5 page.	✓
Attachment of various focal length c-mount CCTV zoom lenses must be possible	✓
An iris should be incorporated into the device so that the laser light intensity can be controlled	✓
One of the mirrors within the Michelson interferometer must be capable of small angle rotations in at least two axes to introduce lateral and longitudinal shear	✓
Phase-stepping must be incorporated into the design of the compact Shearographic interferometer	✓
The prototype must at least be able to inspect an area of 300mm by 200mm so that large objects can be inspected in sections over a short period of time	✓
The formation of fringe patterns must be clearly visible	✗

It can be seen that design concept A fulfills all the design requirements except for the last one which is that the fringes will not be clearly visible since not enough light is transmitted within the optical system. Design concept A was therefore not selected due to this reason as fringe visibility and contrast is very important in Shearography.

4.5.2 Design Concept B

Design concept B worked very well producing fringes that are clearly visible and contrasted. However it does not satisfy all the design requirements. Table 4.7 shows a checklist of the design requirements that were fulfilled by design concept B.

.

Table 4.7: Checklist of the design requirements for design concept B

Design Requirement	Check List
Design a compact Michelson type shearing interferometer	✓
Place the shearing optics between the CCD camera and zoom lens so that the field of view can be increased	✗
The overall dimensions of the interferometer and the CCD camera should be approximately the size of an A5 page.	✓
Attachment of various focal length c-mount CCTV zoom lenses must be possible	✗
An iris should be incorporated into the device so that the laser light intensity can be controlled	✗
One of the mirrors within the Michelson interferometer must be capable of small angle rotations in at least two axes to introduce lateral and longitudinal shear	✓
Phase-stepping must be incorporated into the design of the compact Shearographic interferometer	✓
The prototype must at least be able to inspect an area of 300mm by 200mm so that large objects can be inspected in sections over a short period of time	✓
The formation of fringe patterns must be clearly visible	✓

The major disadvantage of this design is that a CCTV lens cannot be attached to the device making it impractical in that zooming on an object as well as the adjustment of the field of view is not possible. Furthermore, the device is unable to control the intensity of light entering the detector due to the fact that an iris cannot be incorporated easily into the design.

4.5.3 Design Concept C

Design Concept C produces images that are of the same quality as design concept B. However this design concept, unlike design concept B, meets all the design requirements as shown in table 4.8 and was therefore chosen as the design concept used to build the Shearographic prototype. Figure 4.13 is a picture of the Shearographic prototype, destined for portability. A schematic of the compact Shearographic prototype is shown in appendix C.

Table 4.8: Check list of the design requirements for design concept C

Design Requirement	Check List
Design a compact Michelson type shearing interferometer	✓
Place the shearing optics between the CCD camera and zoom lens so that the field of view can be increased	✓
The overall dimensions of the interferometer and the CCD camera should be approximately the size of an A5 page.	✓
Attachment of various focal length c-mount CCTV zoom lenses must be possible	✓
An iris should be incorporated into the device so that the laser light intensity can be controlled	✓
One of the mirrors within the Michelson interferometer must be capable of small angle rotations in at least two axes to introduce lateral and longitudinal shear	✓
Phase-stepping must be incorporated into the design of the compact Shearographic interferometer	✓
The prototype must at least be able to inspect an area of 300mm by 200mm so that large objects can be inspected in sections over a short period of time	✓
The formation of fringe patterns must be clearly visible	✓

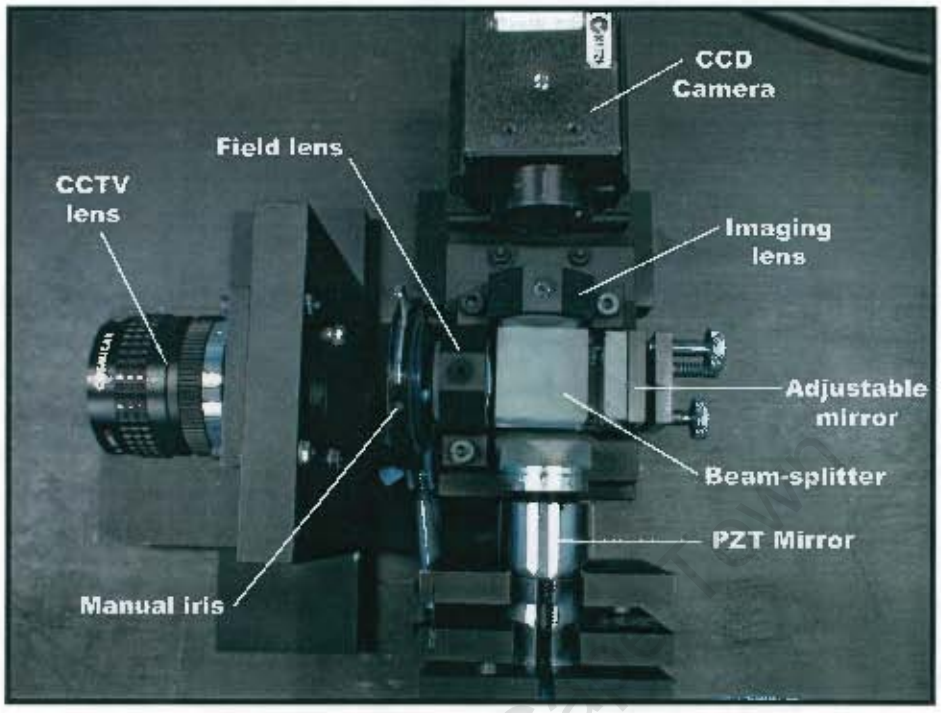

Figure 4.13: Picture of the compact Shearographic prototype

4.6 Specifications of the Hastings Triplet used in Design Concept C

The Hastings triplet has a 23mm diameter and a focal length of 40.3mm. The triple lens system is made up of two concave meniscus lenses cemented to a double convex lens. It is made from BK7 glass and is MgF_2 coated. Figure 4.14 is a picture of the triplet. The lens is held in place by a lens mount. For the schematic of the lens and lens mount refer to appendix C.

Figure 4.14: Picture of the Hastings triplet

5. EXPERIMENTAL DETAILS

The investigation sets out to determine the effectiveness of the Shearographic prototype in detecting the presence and location of defects in a test specimen. This is accomplished by calibrating the device using a calibration test specimen with manufactured defects so that defect size, depth and location are known before testing can commence. Calibration of the device is beneficial in that when tests are done on other specimens with suspected defects, interpretation of the fringe patterns will be made easier since the user will know which anomalies in the fringe pattern would show the presence of a defect.

Subsequent to calibrating the device, tests are carried out by varying the design parameters of the prototype to determine the effect it would have on the resulting fringe patterns. The design parameters that are varied are namely; the distance of the light source and aperture size of the field lens. This is done to find the optimum settings of the device so that clear and prominent fringes can be produced when the object distance ranges from 0.2m to 1.5m.

The final stage of testing is the implementation stage where an engineering component namely an Oryx main rotor helicopter blade is inspected. The blade was rejected by the South African Air Force after it had incurred damage during operation and deemed unsafe by their NDT personnel. Although the Air Force inspected the blade, position and number of defects were unknown when it arrived at the NDT laboratory at the University of Cape Town. The helicopter main rotor blade is first inspected using the compact Shearographic prototype and then the results are verified by cutting the blade at the indicated areas. This helped to determine how effective the prototype is at detecting flaws.

5.1 Experimental Procedure

This section describes the setup and procedure used to obtain results during testing. The setup of the Shearographic equipment is pictured in figure 5.1 and comprises of the following items:

1) A continuous wave 30mW Helium-Neon (HeNe) laser with a wavelength of 632.8nm and coherence length of 100mm. A continuous wave laser is used as it is characterized by the continuous (steady-state) emission of coherent light at relatively low power.
2) A Microsoft XP personal computer with an Intel Pentium 4 processor. Custom written software is installed on the computer. The PC is also fitted with a digitizer card and an expansion card.
3) A SVGA monitor to view fringe patterns.
4) The Shearographic prototype.
5) Test specimen with magnets to fix it in place.
6) Domestic hairdryer to perturb the specimen.
7) Beam expander to disperse the laser light so that the entire inspection area is illuminated.
8) Adjustable mirror to guide the laser through the beam expander.

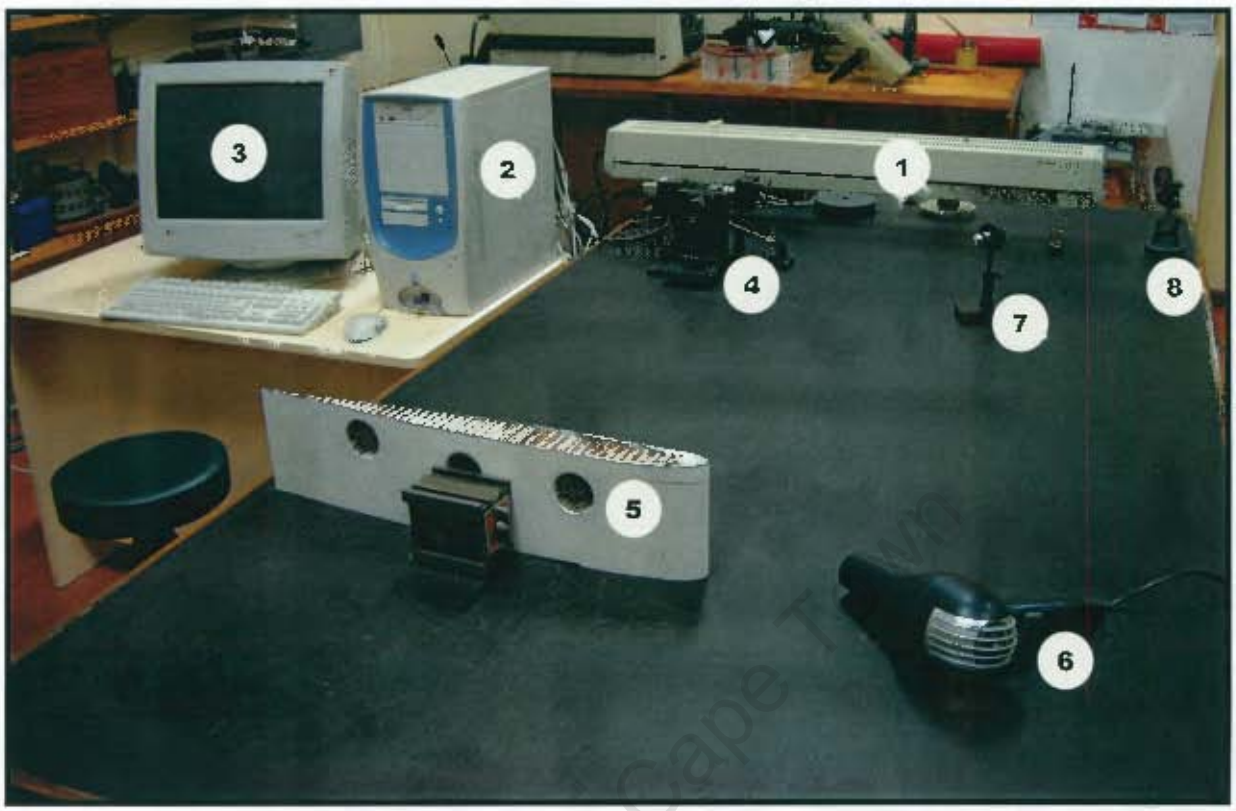

Figure 5.1: Setup of the equipment

5.1.1 Testing Environment

The inspections took place at the University of Cape Town's optical laboratory on a vibration free optical table, although vibration isolation is not a requirement for Shearography. The table's surface is a 25mm steel plate which lies on inflated rubber tubes that rests on a solid rubber base. The test specimens were fixed in place with magnets and all the optical equipment also had magnetic bases.

5.1.2 Connecting the CCD Camera

The CCD camera has two cables which are both connected to the PC. One cable supplies power to the CCD camera from the computer. The other cable, known as a Camera Link Cable connects to the frame grabber or digitizer card on the computer and transmits up to 1.2 GB of data per second from the CCD camera to the computer. Furthermore, the Camera Link

Cable also transmits data from the computer to the CCD camera so that the gain of the camera can be controlled using GUI software since the camera has a built-in LUT (look-up table) for dynamic range control. This allows the user to manipulate the contrast and brightness of the CCD camera detector directly.

5.1.3 Starting up the PC and Focusing of the CCD Camera

As mentioned above the CCD camera is powered by the computer and therefore when the computer is started up the camera will simultaneously be switched on. Once the custom software is opened and loaded a Windows style interface allows the user to view the live video of the specimen under inspection. This allows the user to focus the CCD camera by adjusting the focusing controls and zoom on the CCTV lens. The quintessential features of the software are that it controls the digitizer card, the expansion card, real-time image acquisition and subtraction processes for fringe generation.

5.1.4 Applying Shear

Once the camera is focused, shear is introduced by adjusting the two screws on the miniature angle mount. As discussed in chapter 2, the greater the amount of shear, the greater the sensitivity of the interferometer. However this reduces maximum area that can be inspected. Focusing of the camera should always be done first as it is difficult to discern whether the CCD camera is focused or not when the image on screen is sheared.

5.1.5 Adjusting the Aperture of the CCTV lens

The Helium Neon laser is powered and the beam expander is adjusted so that the dispersed laser light illuminates the desired area of the specimen under inspection. Subsequent viewing of the specimen's surface at this point will appear "grainy" due to speckle. The speckle can be manipulated (i.e. made bigger or smaller) by adjusting the aperture of the CCTV lens. As discussed in chapter two, reducing the speckle size allows the device to detect smaller displacements. However speckle size is limited by the resolution of the CCD camera and therefore when the speckle reaches a certain size it can no longer be resolved. The resolution

of the Pulnix CCD camera is 1300 x 1030. A small test can be done by lightly pushing down on the vibration isolation table to determine whether the speckle will "twinkle". If the black and white spots (i.e. speckle) on the specimen look like they are moving around when the table is depressed, then the speckle should be able to detect minimal displacements. The aperture does not only affect speckle size but it is also adjusted so that the right amount of light will enter the detector of the CCD camera. However the amount of light and speckle work together so if the speckle can be clearly seen then that is the correct amount of light.

5.1.6 Switching the Custom Software to Shearography Mode

Viewing of the interferogram can be done by pressing the Shearography button on the right of the viewing screen on the user interface. Subsequent to pressing the button the software will capture or grab an image of the live video so that an unstressed image of the object can be stored in the computer. This will be used in the subtraction process to generate fringe patterns.

5.1.7 Switching the Custom Software to Phase-stepped Shearography Mode

The user has the choice of going either into Shearography mode or Phase-stepped Shearography mode depending on which mode the user would like to perform the inspection in. If the user wants to stay in Shearography mode this step should be skipped, but if the user wants to go into Phase-stepped Shearography mode step 5.1.6 should be skipped.

To get into Phase-stepped Shearography mode, the user has to press the Phase-stepped Shearography button on the right side of the viewing screen on the user interface. Phase-stepped Shearography will only work if the piezo-electric transducer is connected to the expansion card on the computer. The software controls the piezo-electric transducer by sending a binary number to the expansion card. The binary number is converted into a voltage by a digital to analogue converter and sent to the piezo-electric transducer via the cable that connects it to the computer so that a calibrated micro-displacement can occur. When the button is pressed, an image of the unstressed object is stored in the computer for use

in the fringe generation routines. A clicking sound will then be heard as the piezo-electric transducer goes through its micro-displacements.

5.1.8 Stressing of the Object

The object can be stressed by using one of the following forms of object stressing: (1) thermal stressing (2) mechanical stressing (3) vacuum or pressure stressing and (4) vibration stressing. The manner of stressing is dependant on operator's choice. All inspection procedures during this investigation were carried out by thermally stressing the object as this method works particularly well with composite structures. Heat is provided and applied by a conventional hairdryer for approximately five seconds. Heating the surface of the object generates a thermal wave that propagates through the material. Defects within the material will disturb the generated temperature gradient and lead to localized strains and therefore the presence of a flaw can be identified. In general, thermal stressing causes time-varying changes in surface displacement and it is therefore best used with a CW (continuous wave) laser.

As soon as the object is stressed, fringe patterns will appear on the viewing screen. The computer performs the subtraction process near real-time and constantly updates the viewed video feed. This is due to the fact that the frame grabber is set on continuous grab and therefore the entire process of formation and later the degradation of the fringe patterns can be observed. The degradation of the fringe patterns can occur due to two reasons; (1) the heat supplied to the object has dissipated or (2) too much heat has been provided which will cause the fringes to run over one another hence canceling the fringes.

5.1.9 Adjusting the Brightness and Contrast

Whilst the user stresses the object under inspection and views the resulting fringe patterns, he/she has the option of adjusting the brightness and contrast. This is done by moving the respective sliders on the user interface so that clear and prominent fringe patterns can be observed. The brightness and contrast slider on the user interface act independently of the GUI software controlling the CCD camera and changes the brightness and contrast of the video feed after being retrieved from the CCD camera.

5.1.10 Storing of the Fringe Patterns

Once the user is satisfied with the brightness and contrast of the fringe patterns, the option exists to pause the live viewing of the fringe patterns by pressing the pause button on the user interface. Then the live video which is now a frozen image can be carefully scrutinized or stored for later use.

5.1.11 Filtering of the Fringe Pattern

In Phase-stepped Shearography, once the fringe pattern is paused the user has the option of filtering the image by pressing the filter button on the right hand side of the interface. Before doing this, the user can adjust the number of loops of the filter by moving the number of loops slider left or right. This prevents the image from becoming over filtered causing vital information to be lost. Once the image is filtered it can also be stored for later use.

5.2 Calibration of the Compact Shearographic Prototype

Results obtained for this section of the investigation follow the general experimental procedure documented above.

5.2.1 Calibration of the Device by varying the Defect Depth

The purpose of this test is to firstly determine whether the compact Shearographic prototype can point out the presence and location of a defect. The second reason for performing this test is to establish how varying the depth of a defect affects the resulting fringe patterns. This test is accomplished by inspecting a calibration specimen with three manufactured defects with known position and varying depth. The calibration specimen and manufacturing of the defects are discussed in greater detail in the next section.

5.2.1.1 The Depth varying Calibration Specimen

The test specimen used to calibrate the compact Shearographic prototype is an Oryx main rotor helicopter blade. A section of the blade is used as the calibration specimen with holes cut into it to manufacture defects. Another section of the blade will be inspected during the final stage of testing to determine if the Shearographic prototype is an effective device in detecting flaws within structures and materials.

Figure 5.2: Oryx main rotor helicopter blade

A picture of the Oryx helicopter main rotor blade is shown in figure 5.2. The helicopter blade is made from a composite honeycomb core or matrix with a carbon fiber skin construction. The blade is manufactured by first shaping the honeycomb according to the blade profile and then the multiple layers of carbon fiber skin is glued onto the structure. At the trailing edge the upper and lower skins are glued together and riveted. Aircraft grade aluminium skin is then wrapped and bonded around the leading edge to prevent wear. The helicopter blade is then balanced by adding aluminium strips to the trailing edge.

Figure 5.3:Test Specimen with three manufactured defects

A 140mm length of helicopter blade was cut off from the main section of the blade to manufacture the test specimen. Three equi-distant 52mm diameter holes were cut out on the bottom surface of the blade using a 52mm circular hole-saw, to create the defects. The hole closest to the leading edge was cut to a depth of 22mm; the middle and trailing edge holes were cut to a depth of 28mm and 17mm respectively. The honeycomb was extracted using sand paper. The thickness of the blade at those 3 points starting at the leading edge is 54mm, 49mm and 30mm. Therefore the hole closest to the leading edge is the furthest away from the inspected surface (i.e. the top surface of the blade) at a depth of 32mm.

Table 5.1: Cross-sectional thickness and inspection depth of the manufactured defects

Position of Manufactured Defect	Cross-sectional Thickness (mm)	Depth of Cut (mm)	Distance from inspected Surface (mm)
Leading Edge Hole	54	22	32
Middle Hole	49	28	21
Trailing Edge Hole	30	17	13

The middle and trailing edge holes are 21mm and 13mm in depth from the inspected surface, making the trailing edge defect easiest to detect. The cross-sectional thicknesses of the blade and inspection depth of the three manufactured defects are tabulated in table 5.1. The blade was then spray painted white to increase the reflectivity of the laser light so as to improve light efficiency. Figure 5.3 is a picture of the depth varying calibration specimen with the three manufactured defects.

5.2.2 Calibration of the Device by inspecting a Manufactured Delamination

The purpose of this test is to determine the characteristics of a fringe pattern produced when a delaminated area of a composite structure is inspected. This information will also be useful when the damaged main rotor blade is inspected in the final stage of testing as the researcher will know what characteristics in the fringe pattern point to a delamination. The manufacturing of the delamination calibration specimen is discussed in the next section.

5.2.2.1 The Delaminated Calibration Specimen

Another 420mm length of the Oryx main helicopter blade was cut off to manufacture the delaminated calibration specimen. The delamination was created by pushing a steel ruler between the honey comb structure and the carbon fiber skin and thereby breaking the bond between. The delaminated calibration specimen is pictured in figure 5.4.

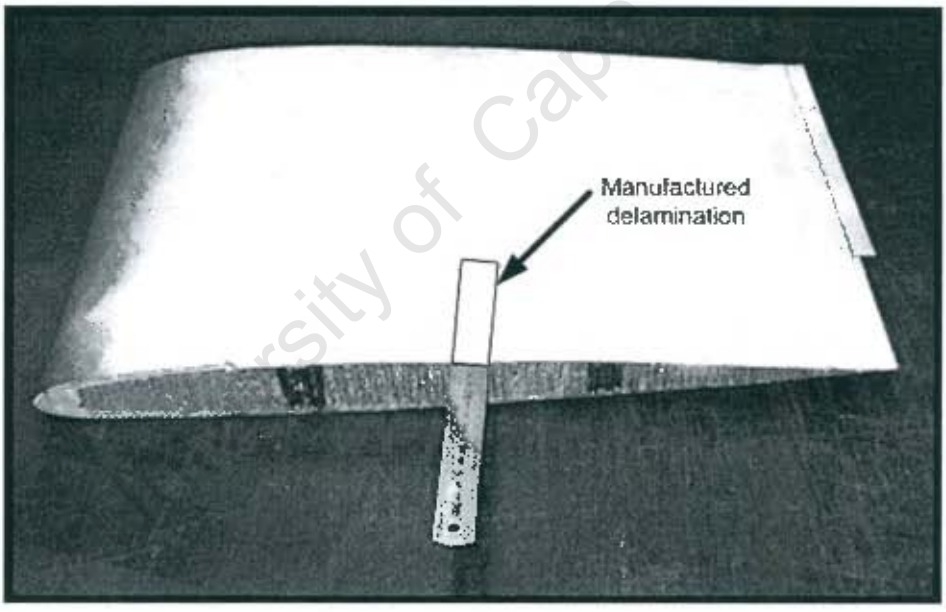

Figure 5.4: Delaminated calibration specimen

5.4 Inspection of a section of the Main Rotor Helicopter Blade

Once the compact Shearographic prototype was calibrated and configured to work at optimum performance the final stage of testing was ready to commence. The same experimental procedure was once again followed to obtain the results.

6. RESULTS AND ANALYSIS

This chapter presents fringe patterns that were produced during the various experiments performed. Typical Conventional Shearographic, Phase-stepped Shearographic and Phase filtered fringe patterns are shown.

6.1 Varying Depth Defect

The calibration specimen, with defects at various depths from the inspecting surface, was first tested using conventional Shearography. The custom software was set to real-time mode so that the response of the calibration specimen to stressing could be observed almost instantaneously. The tests in this section were performed using lateral shear (i.e. shear along the x-axis).

Figure 6.1: Image of leading edge and middle defect obtained by Conventional Shearography

Figure 6.1 depicts the Shearographic fringe pattern that was produced whilst inspecting the defects at the leading edge and approximately at the middle of the aerofoil section. The upper surface of the helicopter blade was inspected, where the defects obviously could not be seen.

The presence and location of the manufactured defects are clearly identified by the two "double bull's eyes". The double bull's eye on the left of figure 6.1 locates the leading edge defect whereas the double bull's eye to the right locates the middle defect. It can be seen that the middle defect has produced four fringes whereas the leading edge defect has produced two fringes, due to the middle defect being 11mm closer to the inspection surface. The number of fringes in an area where a defect is located does usually indicate the amplitude of the localized displacement induced, which is influenced by the size of defect and its depth. The comparison of depth or size of defects can only be made if the two defects are perturbed uniformly for the same period of time and if the fringe patterns are captured at exactly the same time as was attempted in this test. Analysis of the results will be incorrect if the two rules are not followed since the leading edge defect can produce the same amount of fringes as the middle defect if it is captured a few seconds later. In this section of testing the calibration specimen was perturbed for 2 seconds with a domestic hairdryer. The fringe patterns were then captured 10 seconds later.

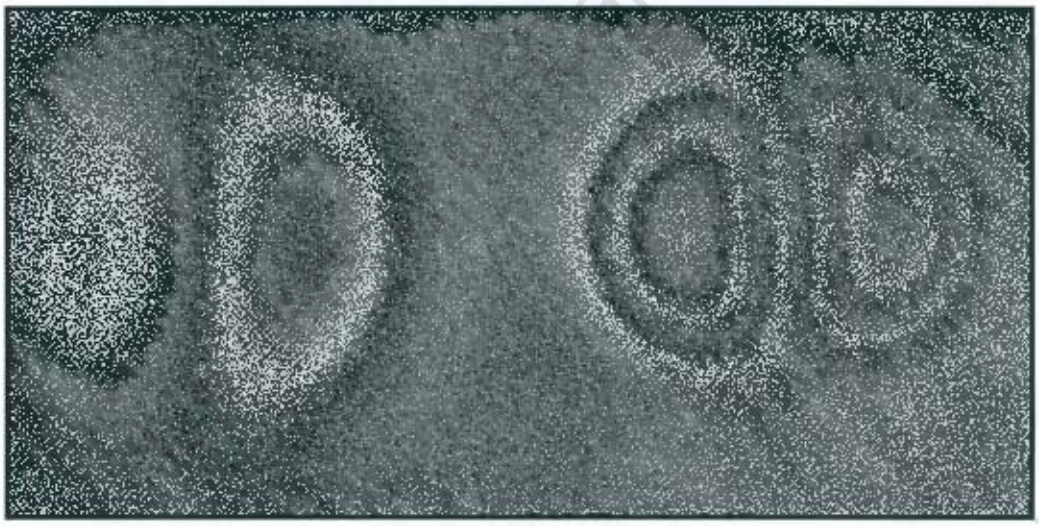

Figure 6.2: Image of leading edge and middle of the blade located defects, unfiltered, obtained by Phase-stepped Shearography

Figure 6.2 shows the unfiltered Phase-stepped Shearographic fringe pattern of the leading edge and middle of the aerofoil defects. The two "double bull's eye" can be seen once again revealing the presence and location of the manufactured defects. Furthermore, even in Phase-

stepped Shearography the number of fringes produced by the middle defect is more than the leading edge defect confirming that the amplitude of displacement is influenced by depth. The Phase-stepped Shearographic fringe patterns appear much more clear and prominent due to the reduction in noise accomplished by capturing and comparing four speckle images at known phase steps, instead of one, as in Conventional Shearography. The 2π discontinuities can also be seen in figure 6.2 where there is an abrupt change from black to white and vice versa.

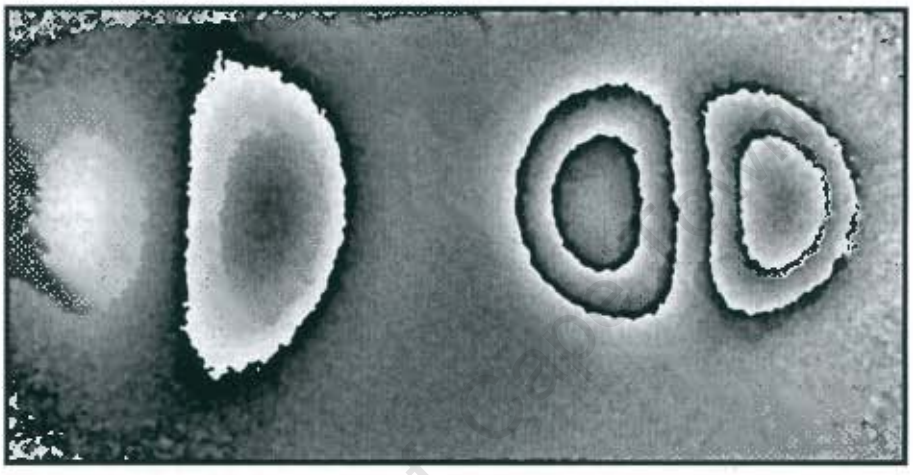

Figure 6.3: Filtered image of the leading edge and middle defect obtained by Phase-stepped Shearography

Figure 6.3 depicts the Phase-stepped Shearography results obtained after the image had been filtered using a 3×3 sine and cosine average filter. It can be seen that the fringe patterns are even more prominent and the grayscale is much smoother due to the filter averaging pixels in a 3×3 neighborhood. Moreover, filtering the image makes the 2π discontinuities more visible.

Figure 6.4: Over filtered image of the middle defect

Figure 6.4 shows the fringe pattern of the middle defect which has been over filtered and therefore smearing of the dense spaced fringes has occurred. Over filtering can be prevented by reducing the number of repetitions of the filter or by applying other filtering methods.

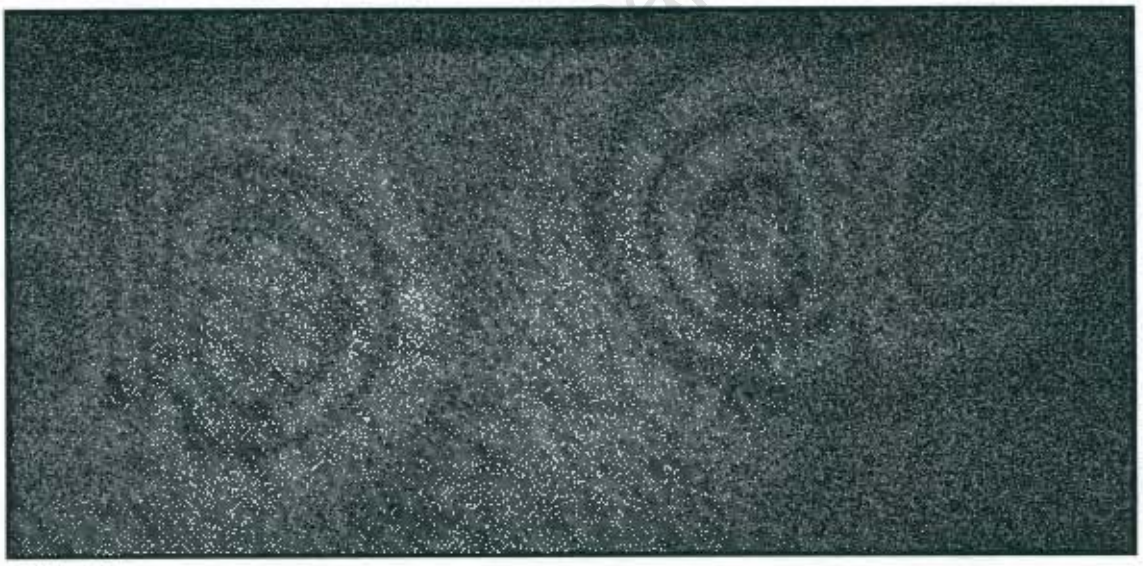

Figure 6.5: Fringe pattern of the middle and trailing edge defect obtained by Conventional Shearography

Figure 6.5 depicts the Conventional Shearography fringe pattern that was produced when inspecting the defects at the middle and trailing edge of the aerofoil. The "double bull's eye" on the left in figure 6.5 is the middle defect where as the "double bull's eye" to the right is the

trailing edge defect. It can be seen that the middle defect has produced two and a half fringes, while the trailing edge defect has produced three fringes. This is due to the trailing edge defect being 8mm closer to the inspection surface than the middle defect. However, the difference in the number of fringes between the two defects in figure 6.5 is not as conspicuous as in figure 6.1. There can be two explanations for these results. The first explanation, which is the more likely one, is that depth difference between the defects in figure 6.1 is greater than the depth difference between the two defects in figure 6.5. In other words, the depth difference between the leading edge and middle defect is 11mm, whereas the depth difference between the middle and trailing edge is 8mm. This smaller depth difference results in the difference in the number of fringes of the two defects being smaller, which is expected. The second explanation for such a small difference in the number of fringes occurring is due to subjective heating. Subjective heating comes about due to the specimen not being uniformly stressed which is possible when using the domestic hairdryer. Therefore the middle defect could have been perturbed for a slightly longer period than the trailing edge defect causing it to produce more fringes. This would reduce the magnitude of the fringe number difference.

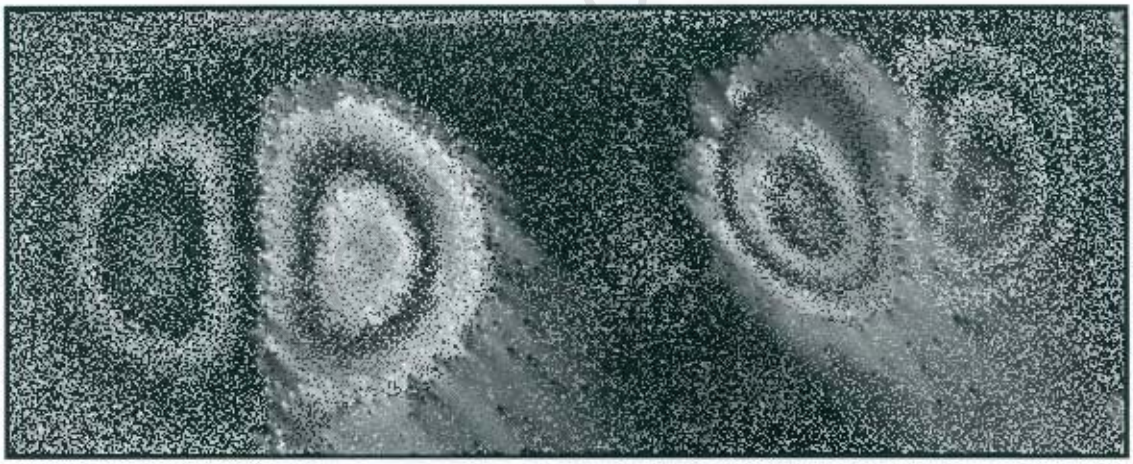

Figure 6.6: Fringe pattern of the middle and trailing edge defect obtained by Phase-stepped Shearography

Figure 6.6 is a fringe pattern of the defects at the trailing edge and the middle of the aerofoil obtained by using Phase-stepped Shearography. It can be seen from the figure that while using Phase-stepped Shearography, the trailing edge defect once again produces more fringes than the middle defect.

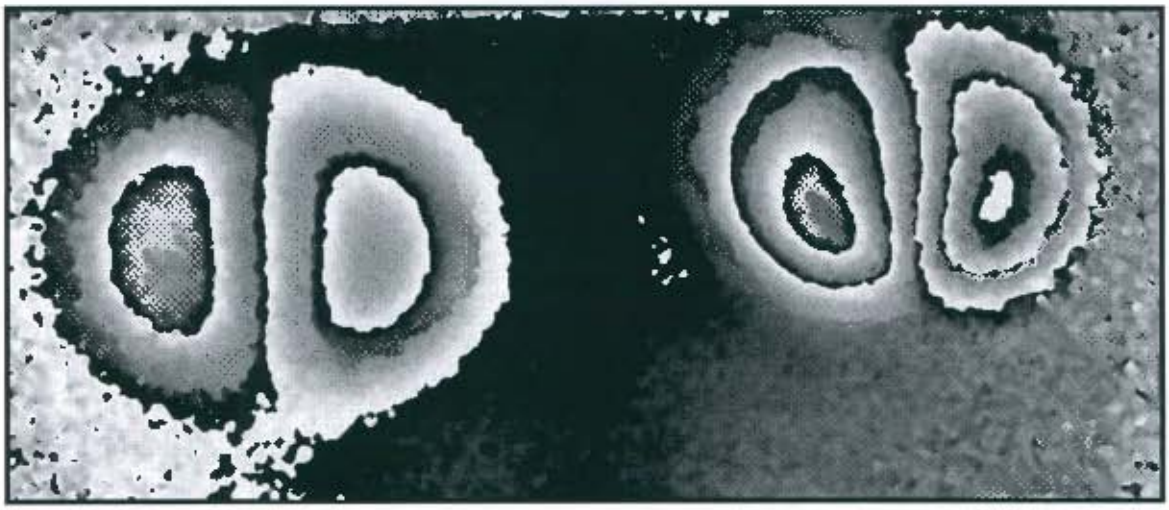

Figure 6.7: Filtered fringe pattern of the middle and trailing edge defect

Figure 6.7 is a filtered image of the Phase-stepped Shearographic NDE fringe pattern of the middle and trailing edge defects. It can be seen that the middle defect has manifested two fringes while the trialing edge defect has manifested three fringes.

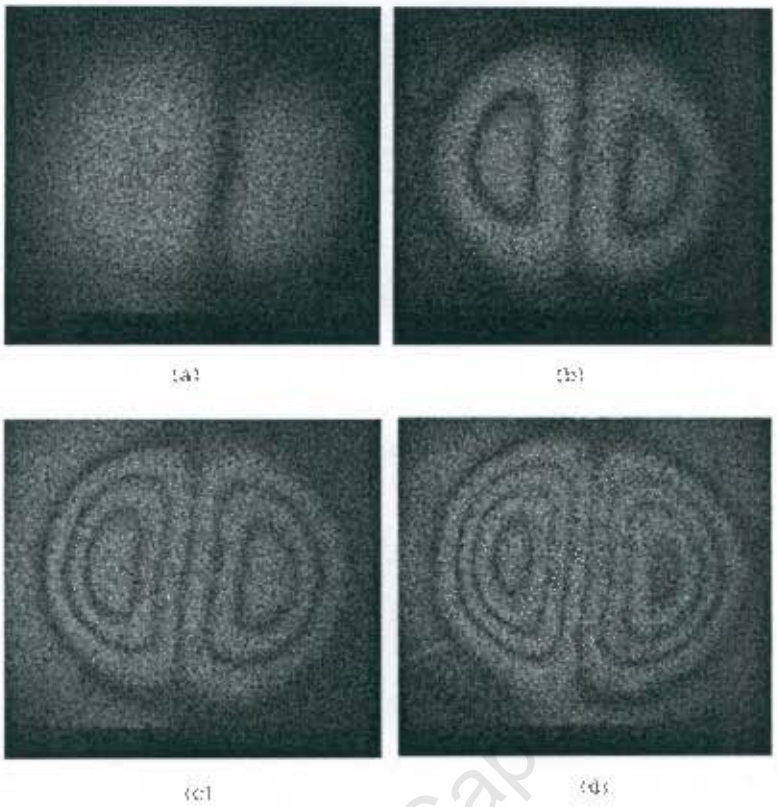

Figure 6.8: Results obtained during different stages of cooling using Conventional Shearography on the same defect. Image 8(a) was captured after 15 seconds of cooling, with a single fringe manifesting, image 8(b) was captured after 22 seconds of cooling, with two fringes manifesting, image 8(c) was captured after 30 seconds of cooling, with three fringes manifesting and image 8(d) was captured after 42seconds of cooling, with four fringes manifesting.

During testing it was realized that the best results can be obtained during the cooling down process. Figure 6.8 depicts the Conventional Shearography fringe patterns obtained during the different stages of cooling. It can be observed that if the specimen is perturbed for approximately five seconds and left to cool, it will manifest more and more fringes as time goes by and provides more information about the defect. However if too many fringes are formed, decorrelation will occur causing the outer fringes to break down and smear the fringe pattern. Therefore the correct moment to capture the fringe patterns appears to be a function of the user's experience.

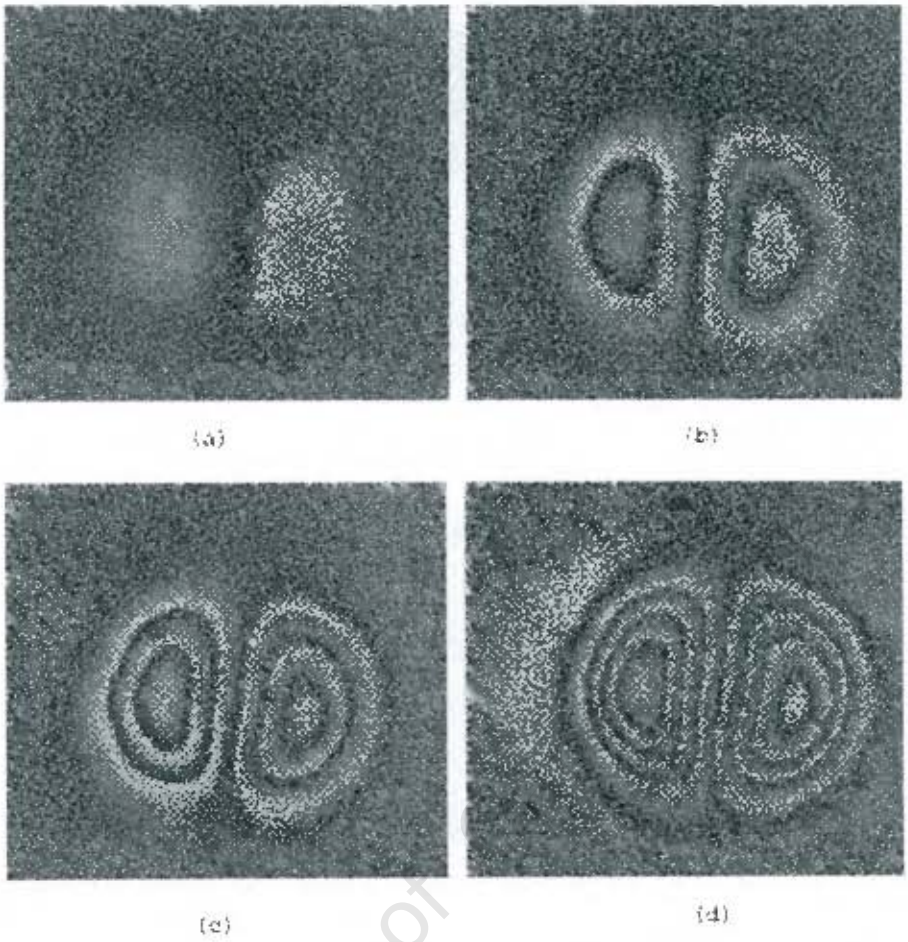

Figure 6.9: Images of the cooling process using Phase-stepped Shearography on the same defect. (a) One fringe after 15 seconds of cooling, (b) two fringes after 22 seconds of cooling (c) three fringes after 30 seconds of cooling, (d) four fringes after 42 seconds of cooling.

Figure 6.9 depicts the results obtained by Phase-stepped Shearography during the cooling process following a similar time period as the images in figure 6.8. Once again it can be seen that if the specimen is left to cool for a longer period of time more fringes will be formed. For completeness, figure 6.10 depicts the four images in figure 6.9 after being filtered.

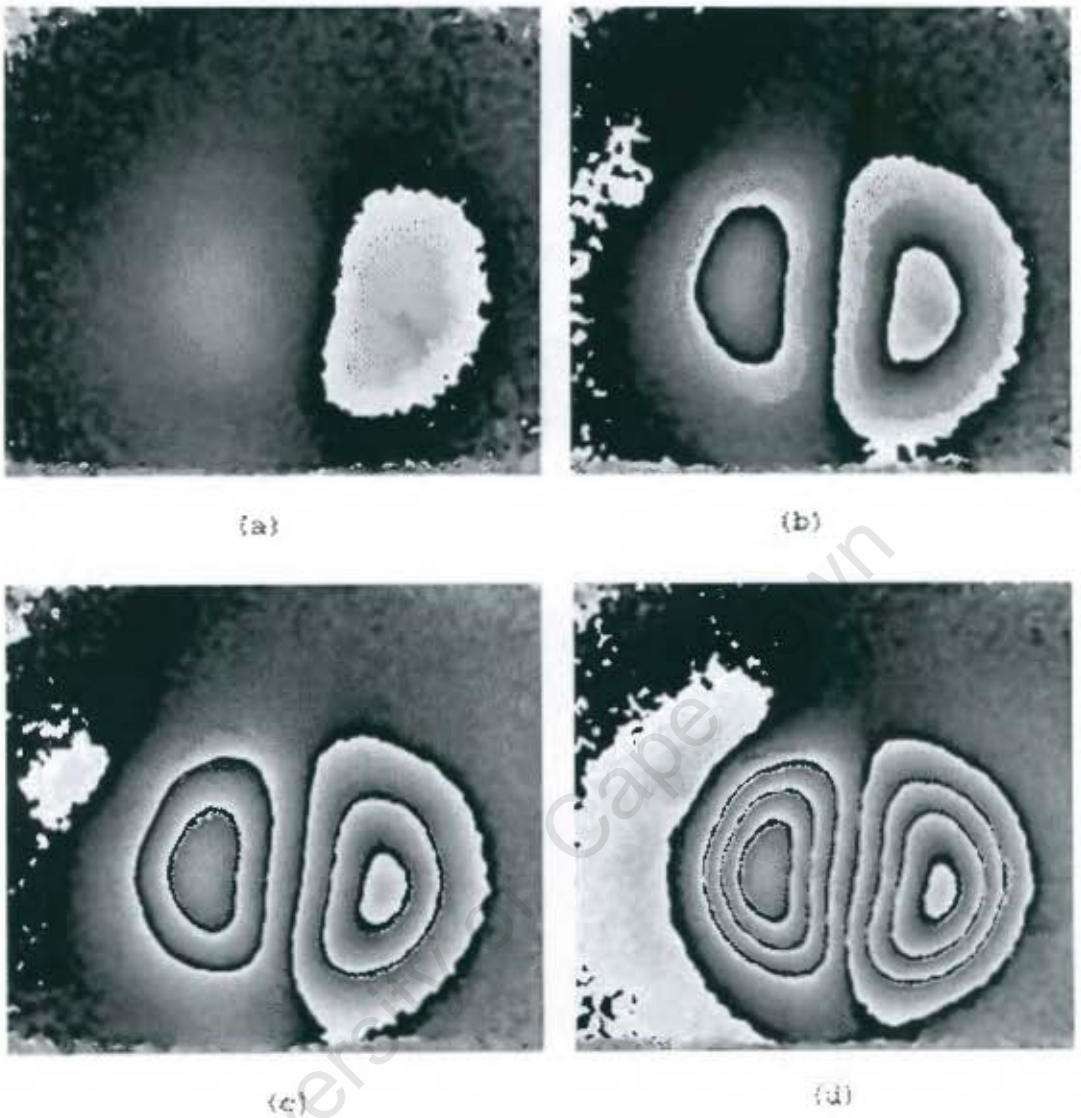

Figure 6.10: Filtered images of the cooling process using Phase-stepped Shearography. (a) One fringe after 15 seconds of cooling, (b) two fringes after 22 seconds of cooling (c) three fringes after 30 seconds of cooling, (d) four fringes after 42 seconds of cooling

6.2 Delamination Defect

The Shearographic fringe pattern of the defect known to be a delamination is depicted in figure 6.11(a). It can be seen that the fringes at the top of the picture are dense with the elongations pointing towards the bottom of the image. The delamination defect was produced by a steel ruler being inserted between the carbon-fiber and honeycomb structure from the bottom end of the helicopter blade as illustrated by the white dashed line in figure 6.11(b). The width of the steel ruler is 25mm and was inserted to a depth of 60mm.

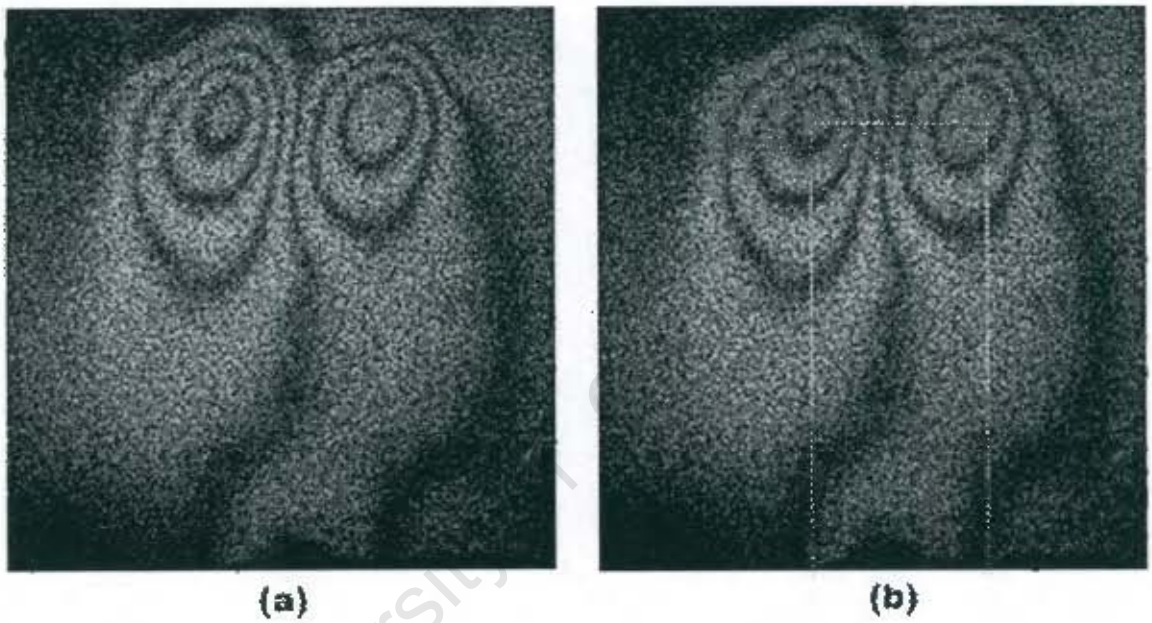

Figure 6.11: Shearographic fringe pattern of: (a) a delamination; and (b) a delamination with an indication where the defect was created.

The localized displacement gradient occurs only at the top of the picture since there is a temperature gradient producing a strain between the edge of the delaminated piece of carbon-fiber and the rest of the carbon fiber that is still glued to the honeycomb structure. Fringes do not occur in quantity within the white rectangle in figure 6.11(b) since this section is totally delaminated resulting in the delaminated section absorbing all the heat. This is because there is a discontinuity in the heat conduction as a result of the separation between the honeycomb and carbon fiber. It can also be seen from figure 6.11(b) that a vertical fringe has formed on

the left hand side of the rectangle as well as to the right of the rectangle; these fringes show the width of the delamination.

Figure 6.12: Phase-stepped Shearographic fringe pattern of the delamination

Once again it can be seen in the Phase-stepped Shearographic fringe pattern (as shown in figure 6.12) that the densest fringes occur at the top of the delamination. The vertical fringes showing the width of the delamination are also clearly visible. The filtered Phase-stepped Shearographic fringe pattern is shown in figure 6.13.

Figure 6.13: Phase filtered image of the delamination

6.3 Varying the Intensity of the Laser Light

The correct intensity of laser light when inspecting an object is vital so that the displacement gradient measurement can be obtained. This means that if the intensity of the laser light is too high it will saturate some or all the pixels of the CCD camera which means that those saturated pixels will not contribute to the measurement of the displacement gradient. In contrast, if the laser brightness is too low it will be impossible to extract the phase from the intensity measurement. The intensity of illumination of a camera pixel can be defined by the equation below, as stated in section 2.1.3.2 of chapter two.

$$I = I_O + I_M \cos\phi$$

An acceptable displacement gradient measurement with the appropriate intensity of object illumination would have a high modulation intensity I_M and a total intensity I that is below saturation so that the phase can be extracted.

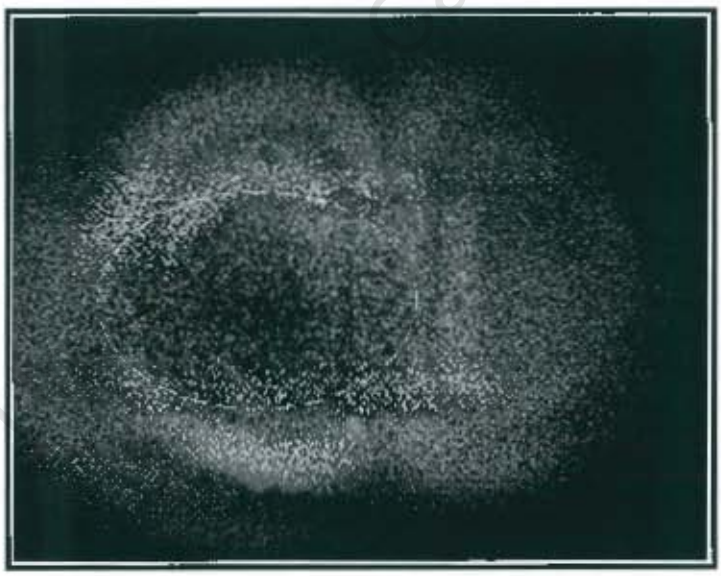

Figure 6.14: Fringe pattern of middle defect with high object illumination

Figure 6.14 is a fringe pattern of the middle defect when the object was positioned 1.5m from the compact Shearographic prototype with the CCTV zoom lens zooming into an area of

100mm by 90mm. The beam expander is 300mm away from the inspection surface and the CCTV zoom lens's manual iris is fully open allowing all the light to enter the detector of CCD camera. It can be seen from figure 6.14 that saturation of the camera pixels has occurred in the area circled by the white dashed line. It can also be seen that pixels outside the circle are not saturated in that fringes are still visible here. This shows that when the object illumination is too high, saturation of the pixels will occur, resulting in black pixels being formed instead of a good displacement gradient measurement. Black pixels are produced since both the reference image and the stressed object image intensity are at saturation. Therefore when they are subtracted a black pixel will be the result.

Figure 6.15: Fringe pattern of the middle defect with insufficient light

Figure 6.15 is a fringe pattern of the same defect but this time the manual iris of the zoom lens is almost closed. It can be seen from figure 6.15 that the fringe pattern does show signs of a displacement gradient (i.e. fringes are present) however due to the lack of light the fringes are not well contrasted and defined.

Figure 6.16 is a fringe pattern of the middle defect but this time the manual iris is slightly closed so that the modulation intensity is high but not too high as to saturate the pixels or too low as to cause loss of fringe definition, which results in well contrasted fringe pattern.

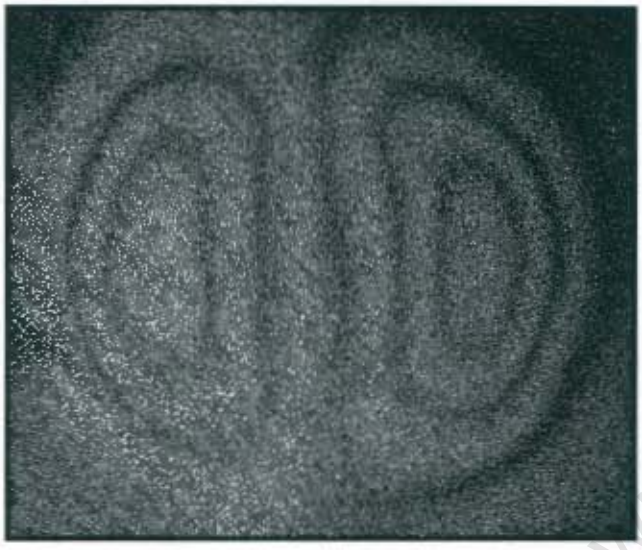

Figure 6.16: Fringe pattern of middle defect with the appropriate amount of light

Figure 6.17 (a)-(f) depicts Conventional Shearographic NDE fringe patterns produced while the beam expander is moved further and further away from the object under inspection. It can be observed that as the beam expander is moved away from the object, the resulting fringe patterns become dark as expected and also lose definition. The aim of this test was to find the optimum position of the beam expander so that well contrasted fringe patterns can be produced continuously. Looking at the fringe patterns in figure 6.17 it can be seen that the best quality fringe patterns are produced when the beam expander is at 300mm. If the beam expander is positioned any closer it will be in the field of view of the camera. Furthermore, at 300mm the manual iris of the CCTV lens is slightly closed which shows that positioning the beam expander slightly further back will also still produce good quality fringe patterns. At 500mm the fringe patterns are still well contrasted and no visible differentiation can be made between this fringe pattern and the one produced at 300mm. This shows that when the beam expander is between 300-500mm good quality Shearographic fringe patterns will be produced. It is clearly visible that the fringe patterns at 700mm and 900mm are darker and that the fringe patterns are disappearing into the background. In figure 6.17 (e) and (f) the contrast is even worse with the fringes being barely visible.

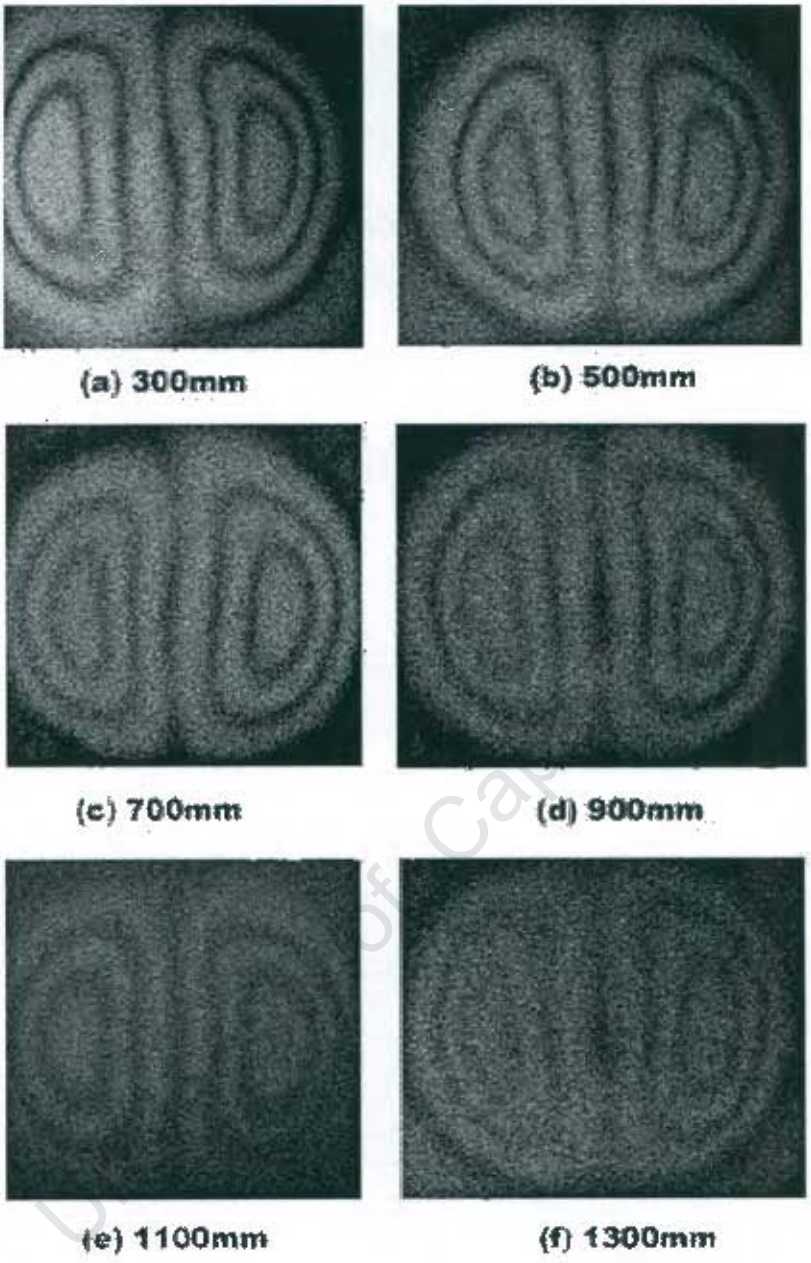

Figure 6.17: Varying the distance of the laser light using Conventional Shearography

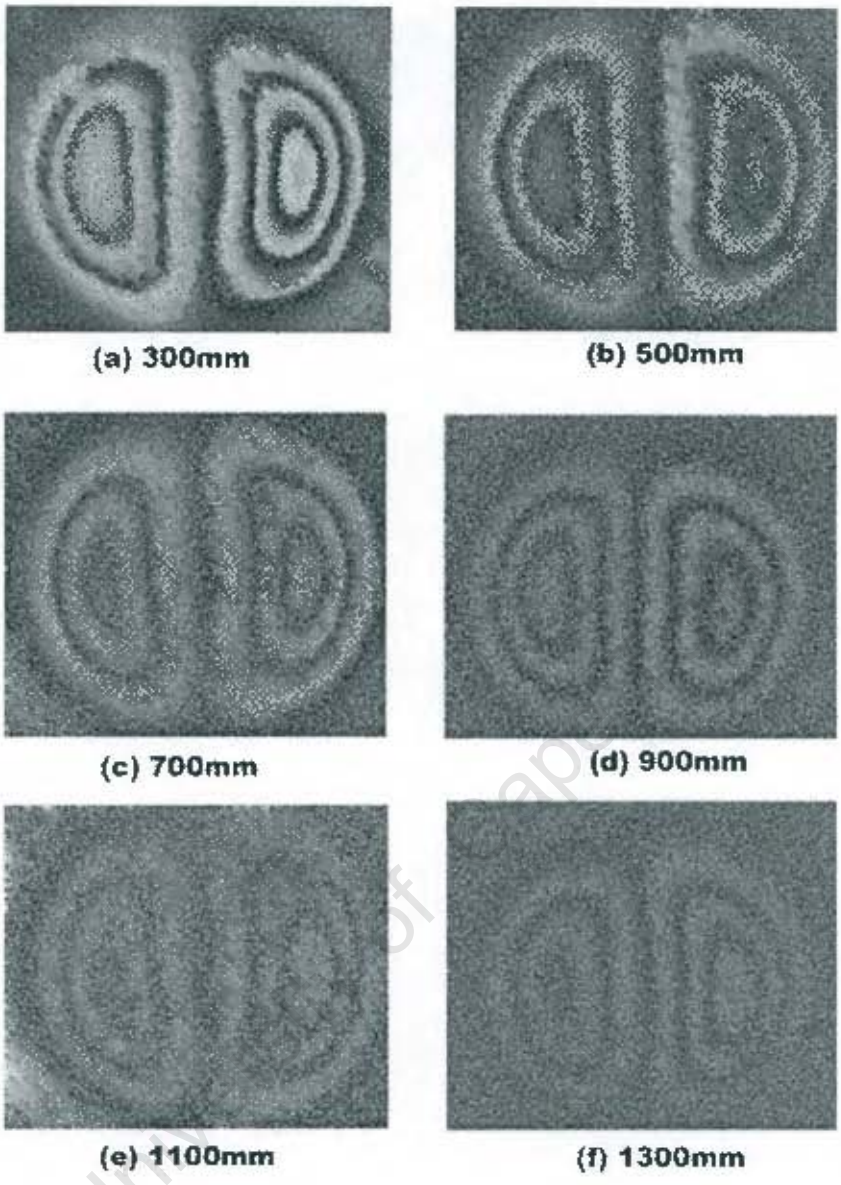

Figure 6.18: Varying the distance of the laser light using Phase-stepped Shearography

Figure 6.18 (a)–(f) depicts the fringe patterns produced when using Phase-stepped Shearographic NDE. It can be seen from figure 6.18 (a)-(f) that there is a gradual deterioration in fringe quality. However, in Phase-stepped Shearography the fringes are still more clearly visible than in conventional Shearography.

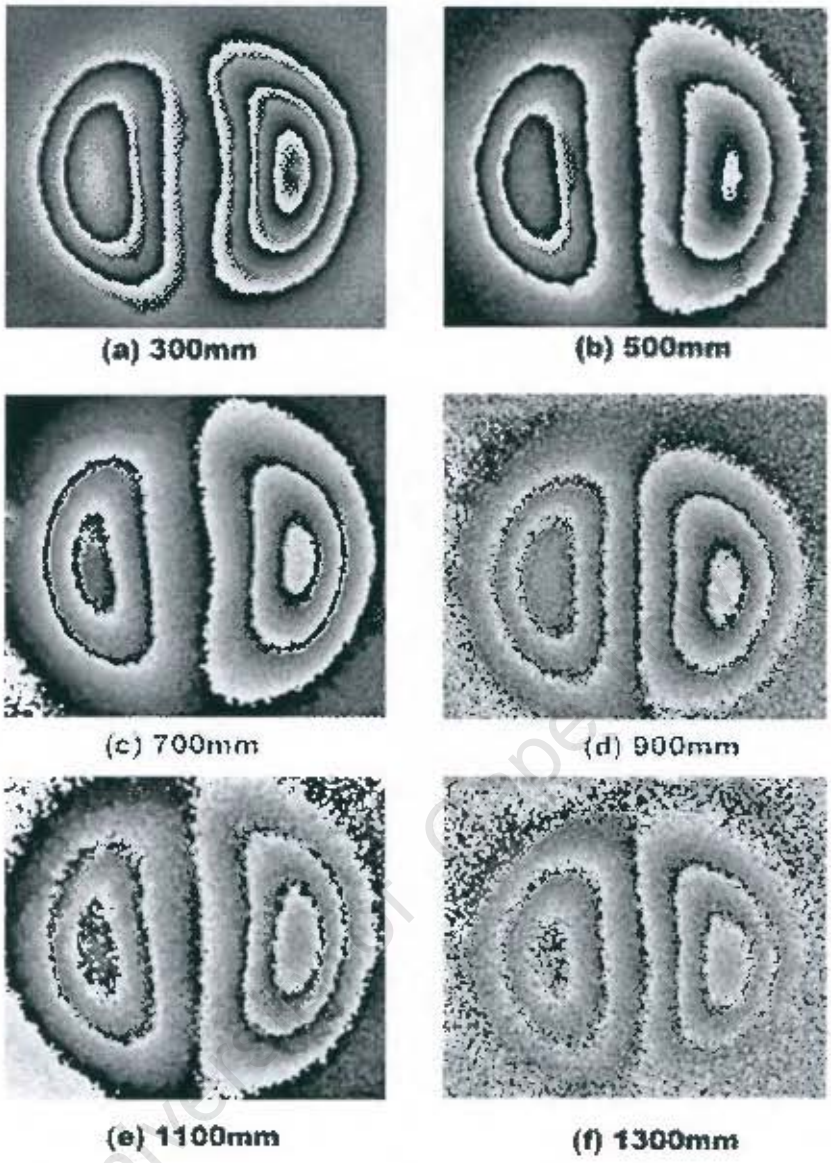

Figure 6.19: Varying the distance of the laser light, filtered Phase-stepped images

Figure 6.19(a)-(f) are the filtered Phase-stepped fringe patterns where the effects of varying the light intensity are clearly discernible. It can be seen from figure 6.19(a) that the boundaries of the fringes (i.e. the 2π discontinuities) are very smooth as compared to the rest of the images, therefore the irregularities on the fringe boundaries point to a lack of laser light. Moreover, it can be seen that these irregularities on the fringe boundaries become worse with diminishing light.

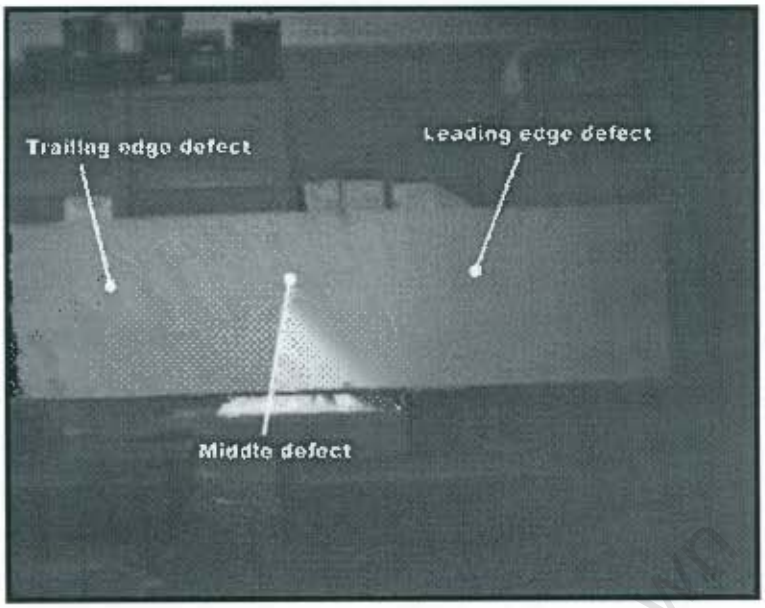

Figure 6.20: Field of view of the compact Shearographic with an 8.5mm CCTV lens

The area that can be covered in one inspection (i.e. one image) is very important in that when inspecting a large object it will take longer if the field of view of the device is small. Therefore a fairly large inspection area is a preferred characteristic for a compact Shearographic system to have, since it will take less man hours for testing.

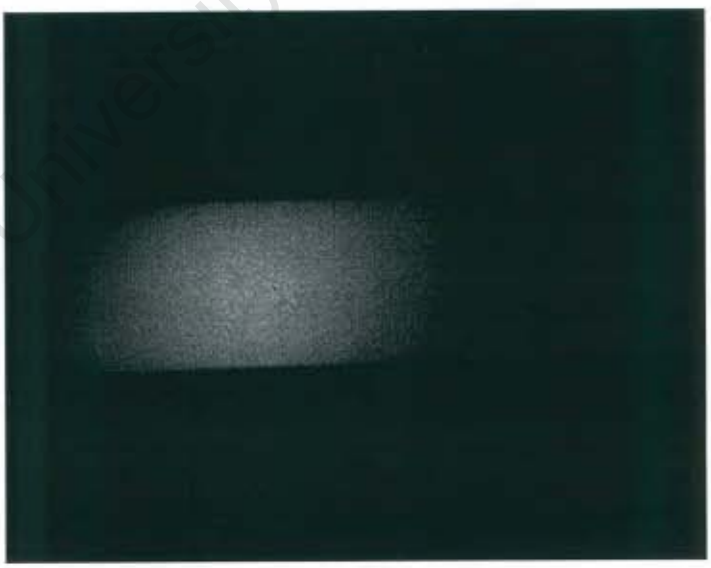

Figure 6.21: Illumination area of the expanded laser beam

The inspection area of the compact Shearographic system is a function of two things namely; the optical configuration of the device and the illumination area of the laser light. Figure 6.20 is an image captured by the compact Shearographic system showing the field of view of the device in normal light with an 8.5mm CCTV lens. It can be seen from figure 6.20 that the CCTV lens has a wide field of view and that almost the entire length of the blade can be seen.

Figure 6.21 is an image of the blade, in the same position as shown by figure 6.20, captured when the laboratory lights are switched off and the helium-neon laser is switched on. It can be seen that the laser power is insufficient to illuminate the entire length of the blade and covers an area of approximately 18cm in diameter. However when viewing the blade directly it can be seen that the laser light is able to illuminate the entire blade.

The reason for seeing only a small portion of the blade as depicted figure 6.21 is that the laser has a Gaussian distribution with only the most intense rays of laser light make it to the CCD detector and the rest of the rays either being reflected or absorbed by the optical components. Therefore only the inner rays of the expanded laser light which are the most intense make it into the detector of the CCD camera forming an 18cm area of illumination. The other reason for loss of laser light is that the Michelson interferometer only captures 50% of the laser light in that the rest of the laser light is guided out of the device by the beam-splitter through the field lens.

The optics that have been selected for the prototype have the best transmission (i.e. the lenses and beam-splitter) and reflection (i.e. the mirrors) efficiencies within the allocated expenditure. Therefore it is clear that the inspection area of the prototype can only be increased by using a higher power laser and that the optical configuration allows for a larger area to be inspected. The inspection area of the Shearographic system using the 30mW Helium-neon laser is 220mm by 220mm with the help of the custom software making the image brighter. Figure 6.22(a)-(c) depicts the conventional Shearography, Phase-stepped Shearography and Phase filtered image of the fringe patterns taken using the 8.5mm CCTV lens with the object at the same position as in figure 6.20 and 6.21.

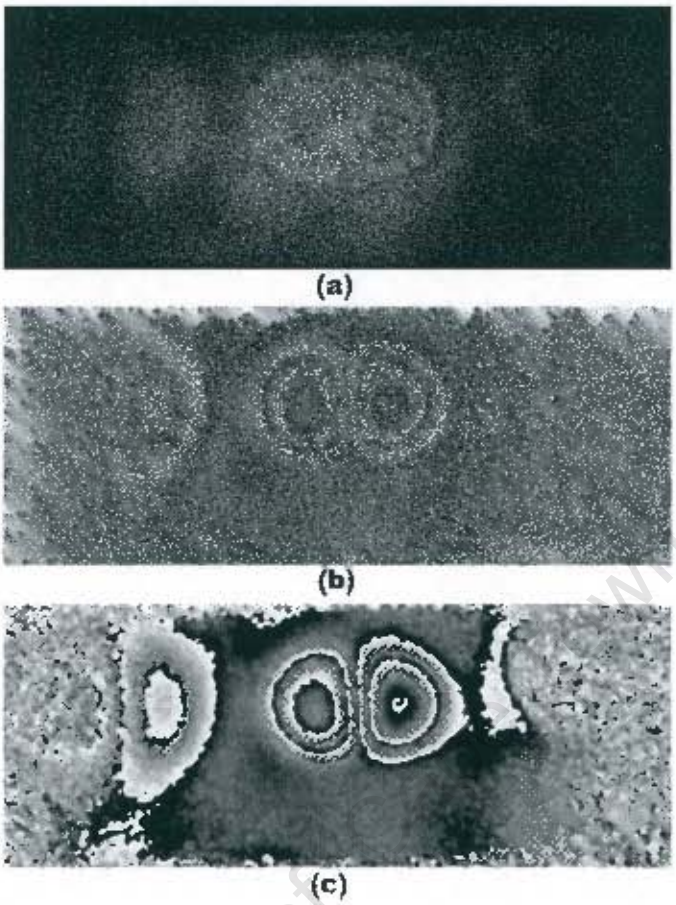

Figure 6.22: Inspection of all three defects (a) Fringe pattern using Conventional Shearography, (b) fringe pattern using Phase-stepped Shearography and (c) Filtered Phase-stepped fringe pattern.

It can be seen from figure 6.22 that it is impossible to inspect all three defects at the same time due to the lack of laser power. The distance between the leading edge and the trialing edge defect is 35cm and therefore only two of the three defects can be inspected at a time.

6.4 Varying the Aperture of the Field Lens

Contrast and clarity of fringe patterns are extremely important in Shearography in that the lack of fringe definition will hinder the ability of the compact Shearographic system in detecting the presence and location of flaws in an object. The contrast and resolution of resulting fringe patterns can be controlled by the device by adjusting the size of the manual iris in front of the field lens. Reducing the size of the manual iris increases the numerical aperture of the lens

thereby reducing the amount of light that enters the lens which subsequently increases the MTF of the lens, hence producing fringe patterns that are well resolved and contrasted.

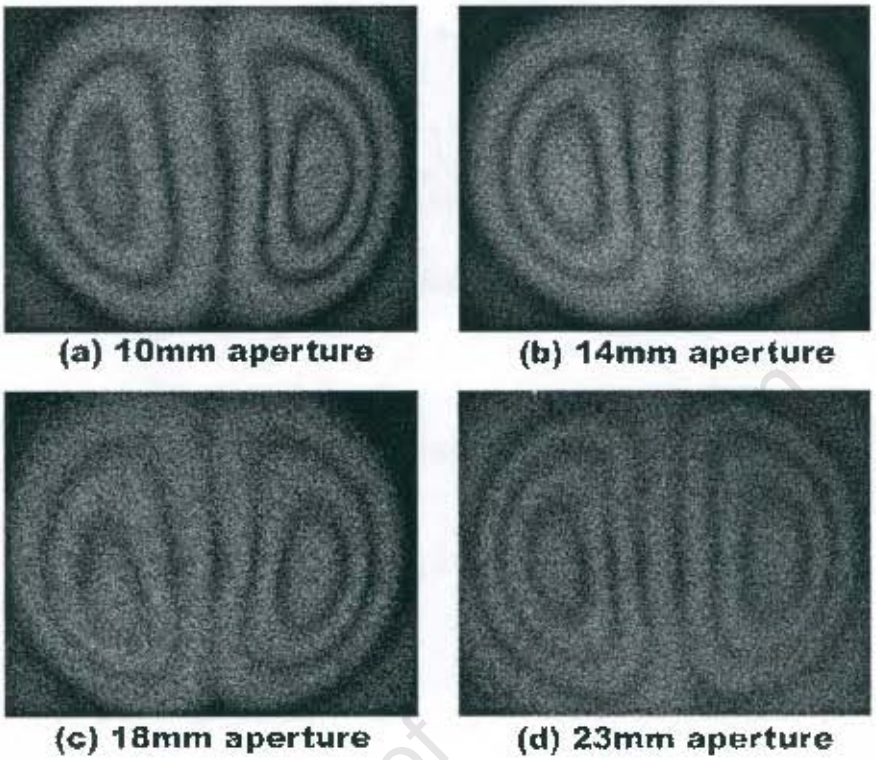

Figure 6.23: Varying the diameter of the manual iris using Conventional Shearography

Figure 6.23(a)-(d) depicts Conventional Shearography fringe patterns that were produced while varying the diameter of the iris of the field lens. It can be seen from figure 6.23(a)-(d) that as the diameter of the iris increases the contrast and resolution of the fringes starts to decrease. In all instances the object was perturbed for 2 seconds with the fringe pattern being captured 10 seconds after stressing.

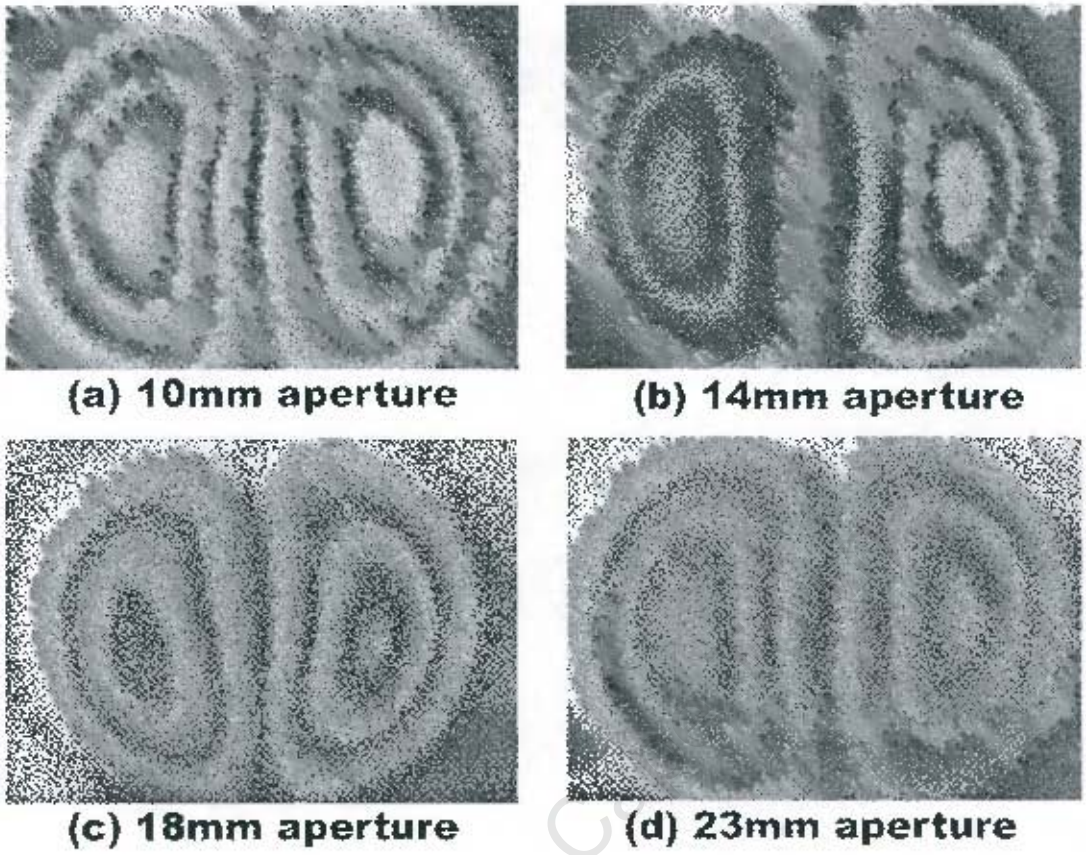

Figure 6.24: Varying the diameter of the manual iris using Phase-stepped Shearography

Figure 6.24(a)-(d) depicts the fringe patterns that were manifested using Phase-stepped Shearography. Once again, although not as apparent as conventional Shearography, it can be seen that there is degradation in fringe definition.

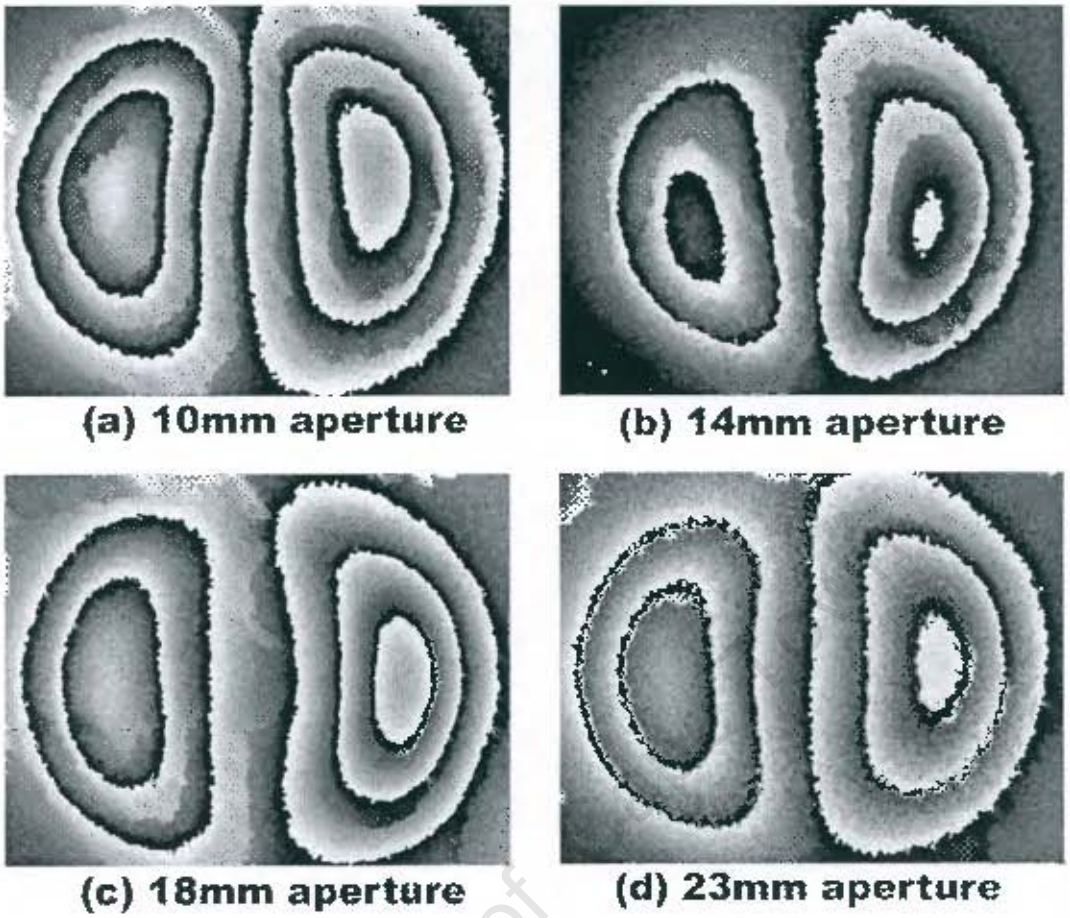

Figure 6.25: Varying the diameter of the manual iris phase-filtered images

Figure 6.25(a)-(d) are the filtered images of figure 6.24(a)-(d). It can be seen that once the images are filtered no clear distinction between the images can be made, except that the outer fringes seem to become rougher/noisy as the iris diameter is increased.

The MTF (Modulation Transfer Function) curves for the 23mm diameter Hasting triplet lens with a 10mm, 14mm and an 18mm aperture is shown in appendix D and an explanation of MTF can be found in appendix A . The spatial frequency, measured at the image plane (i.e. at the position of the detector of the CCD camera), is plotted on the x-axis whereas the MTF is plotted on the y-axis. The spatial frequency of the compact Shearographic system is approximated to be five cycles per millimeter and therefore the 10mm aperture has 83% MTF rating, the 14mm aperture has a 55% MTF rating and the 18mm aperture has a 34% MTF

rating. Therefore the reason for the degradation in fringe contrast is due to the MTF rating (i.e. the ability to transfer contrast) decreasing with increase in aperture size. Although the field lens's ability to transfer contrast improves with a decrease in aperture, the ability of the Shearographic device to inspect a large area diminishes due to less light entering the CCD camera. Hence a compromise between MTF and inspection area has to be made for a given laser's illumination power.

6.5 Inspection of a Section of the Main Rotor Helicopter Blade

The Shearographic system is capable of inspecting objects without any surface preparation; however spray painting an object increases reflectivity and thereby makes it easier to find anomalies in the resulting fringe patterns. Therefore, the blade section was spray-painted matt-white before testing could commence. During initial testing Conventional Shearography was used to locate the presence and location of defects. Once this was accomplished Phase-stepping and filtering were used to better observe the irregularities. Figure 6.26 is a schematic showing side A of the blade as well as the location and the phase filtered fringe patterns of each of the anomalies that occurred when the blade was inspected.

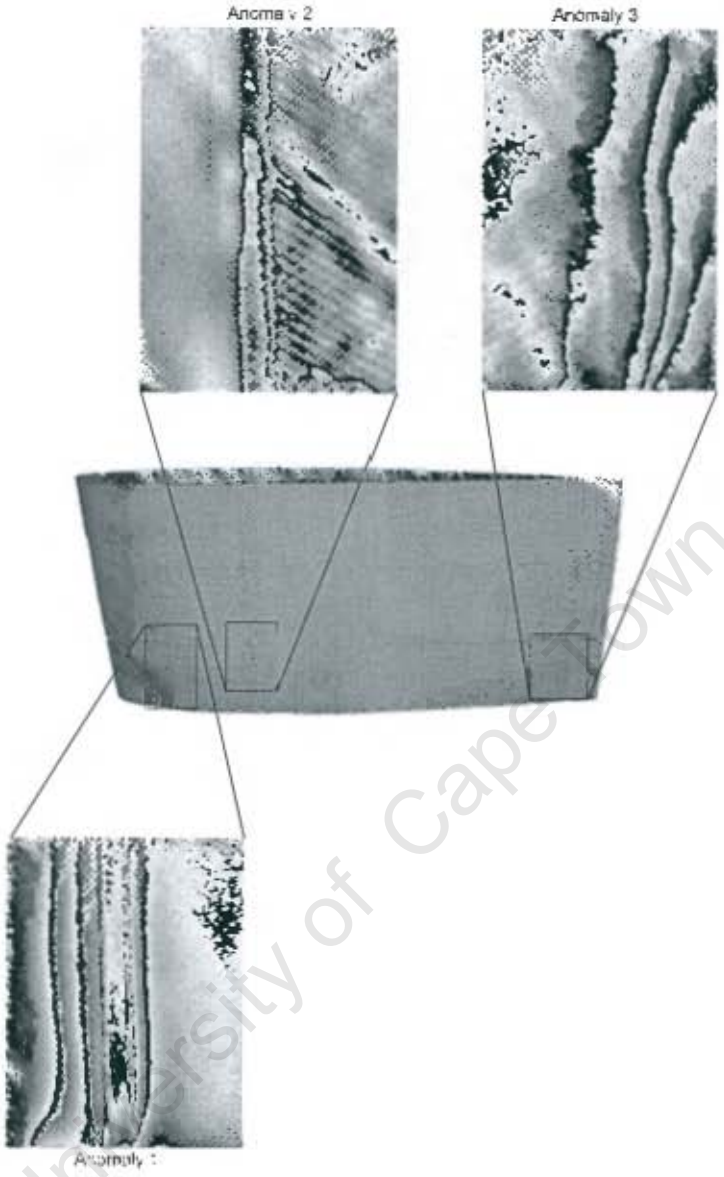

Figure 6.26: Schematic showing the locations of anomalies, side A of the blade

Figure 6.27 depicts the location and the corresponding Phase filtered fringe patterns of the anomalies when side B of the blade was inspected. Each of the anomalies will be discussed in greater detail in the sections that follow.

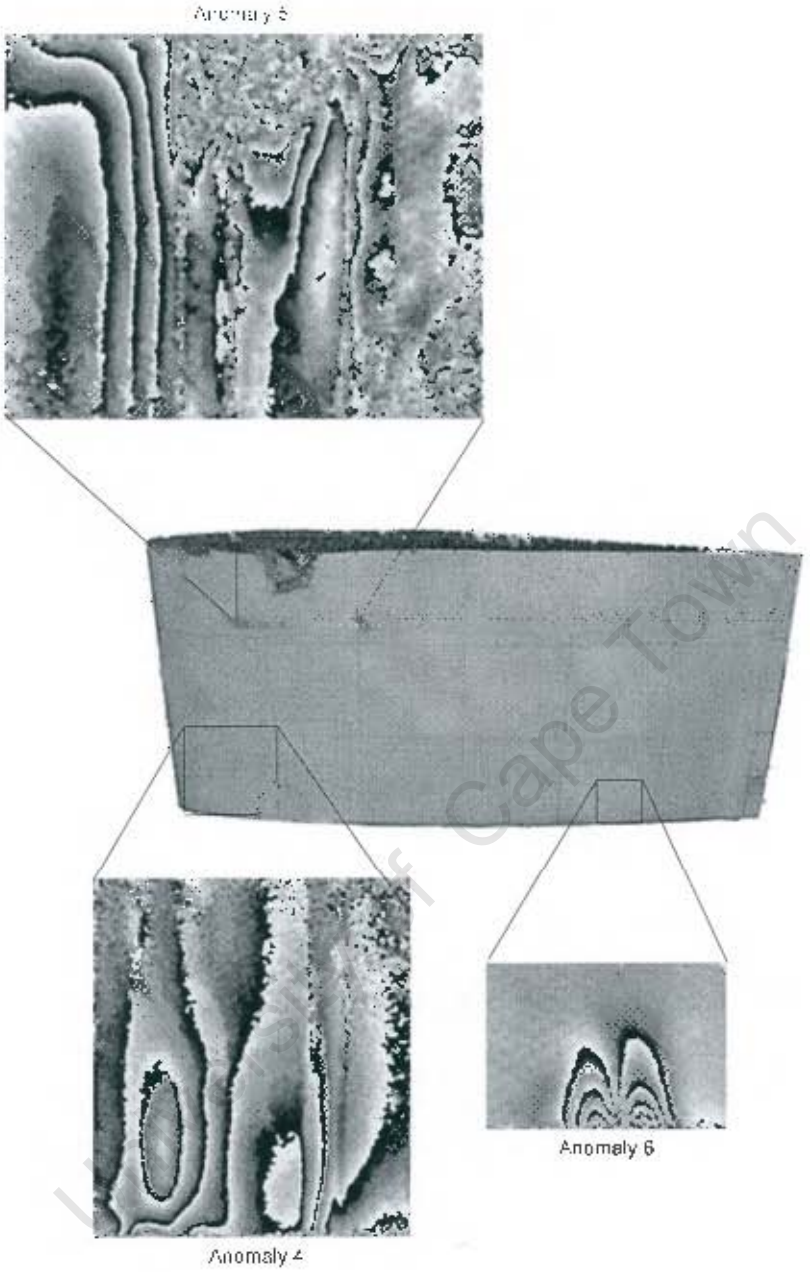

Figure 6.27: Schematic showing the locations of anomalies, side B of the blade

6.5.1 Inspection of a Defect Free Area

It is important to observe the fringe patterns or lack of them when inspecting an unflawed area of the helicopter blade so that the reader can gauge the simplicity of locating fringe pattern

anomaly using Shearography. Figure 6.28(a) is a "fringe pattern" obtained when inspecting a defect-free area of the blade. Figure 6.28(b) and (c) are the Phase-Stepped Shearographic fringe pattern and phase filtered of the defect-free area.

Figure 6.28: Fringe patterns of a defect free area using: (a) Shearography, (b) Phase-Stepped Shearography and (c) Filtering of phase image

It can be seen from figure 6.28(a) that speckle is being observed and no fringe patterns have formed since there is no change in the displacement gradient. Figure 6.28(b) and (c) show the Phase-stepped Shearography and Phase filtered "fringe patterns" respectively. It can be seen from these images as well that no fringe patterns have formed.

6.5.2 Anomaly One

Anomaly number one occurred along the entire length of the blade section, 115mm away from the leading edge as shown in figure 6.29. The fringe patterns shown in figure 6.30(a)-(c) are from the bottom edge of the blade as shown in figure 6.26.

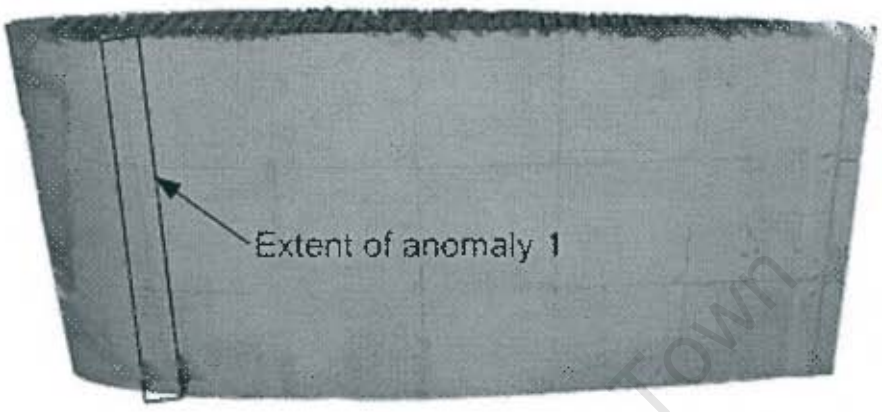

Figure 6.29: Location and extent of anomaly one, on side A of the blade

It can be seen from the Shearographic fringe pattern in figure 6.30(a) that the fringes are perfectly vertical indicating that the strain is uniformly distributed and that the anomaly is symmetrical. However at the bottom of the image, which is the bottom of the blade, a slight divergence of the fringes is visible. The divergence of the fringes is more evident in the Phase-stepped Shearographic and Phase filtered images in figure 6.30(b) and (c) respectively, which appears to be a delamination that was probably caused when the blade was cut. The same type of fringe pattern as shown in figures 6.30(a)-(c) was observed when the entire length of the blade was inspected excluding the divergence of the fringes.

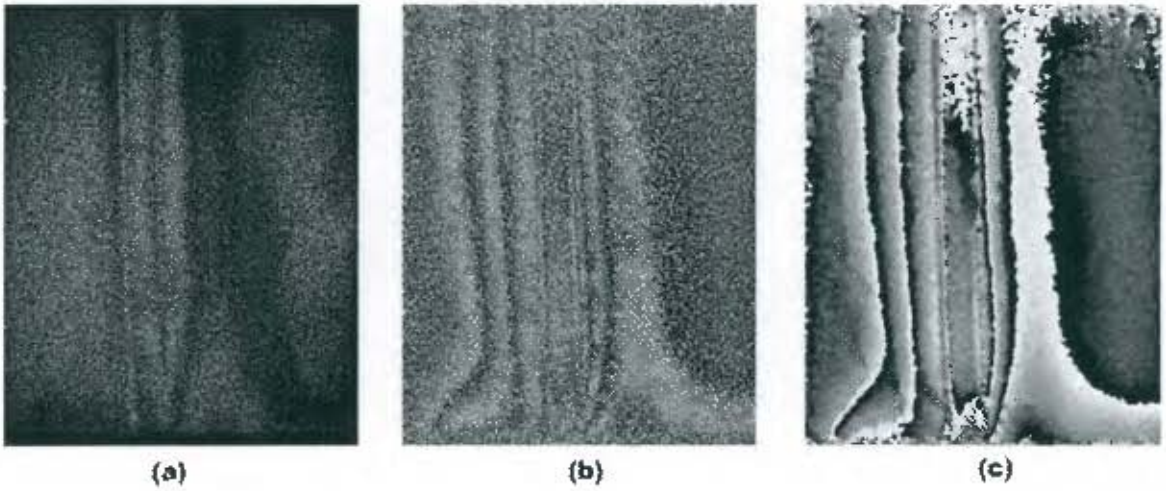

Figure 6.30: Fringe patterns of anomaly one, side A, using: (a) Shearography, (b) Phase-stepping and (c) filtering

The same anomaly was observed on the reverse of the blade at exactly the same position which in other words means that the anomaly is relatively large or that it is sensed across the entire cross-section of the blade. Figure 6.31(a) depicts the Shearographic fringe pattern while figures 6.31(b) and (c) depict the Phase-stepped Shearographic and Phase filtered fringe pattern of anomaly number one discerned on side B.

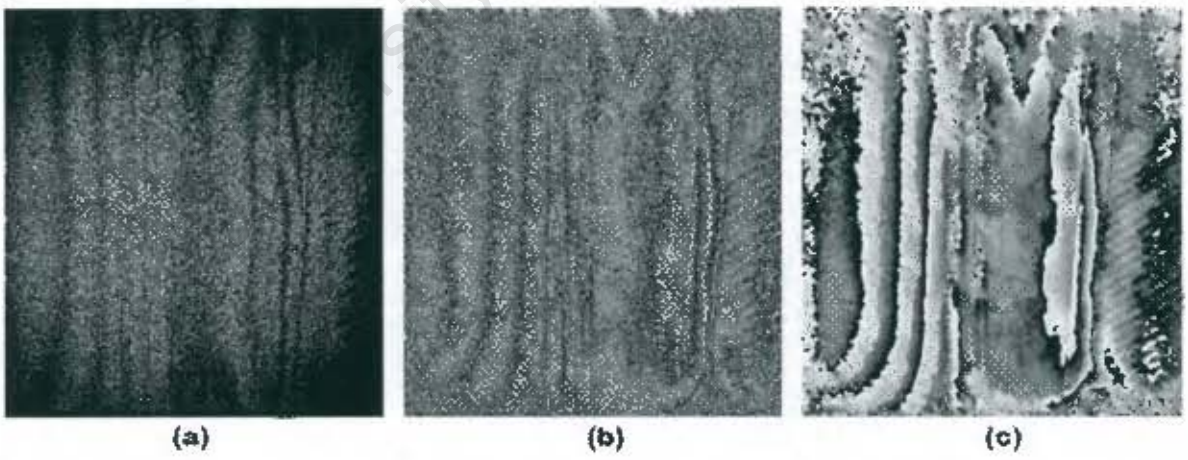

Figure 6.31: Fringe patterns of anomaly one, side B, using: (a) Shearography, (b) Phase-stepping and (c) filtering

It can be seen from the pictures that there are two localized displacements gradients, the one on the left is anomaly number one and looks exactly like the fringes on side A. The dense fringes on the right is anomaly number two which is also visible on both sides of the blade and runs parallel to anomaly number one.

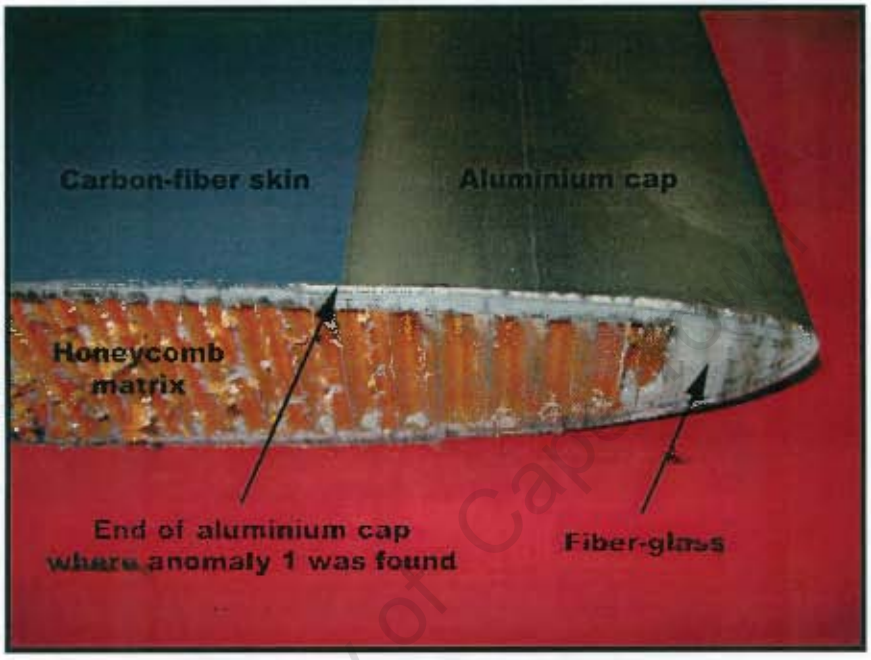

Figure 6.32: Picture of the aluminium cap on the leading edge of the blade

After scrutinizing the cut out cross-section of the blade it was realized that the anomaly occurred due to the way the blade was manufactured. The leading edge of the blade is made of four different materials namely; aircraft grade aluminium, fiber-glass, carbon-fiber and a honeycomb matrix. The aluminium piece is C-shaped and covers the leading edge to prevent abrasion and ends exactly where anomaly number one was found as shown in figure 6.32. This also explains why the anomaly runs across the entire length and on both sides of the blade in that the aluminium cover does the same. Therefore the Shearographic system picked a change in material which is exactly how a defect would react when perturbed.

6.5.3 Anomaly Two

Anomaly number two occurred 200mm away from the leading edge and was also found to run along the entire length of the blade on both side A and B as shown in figure 6.33.

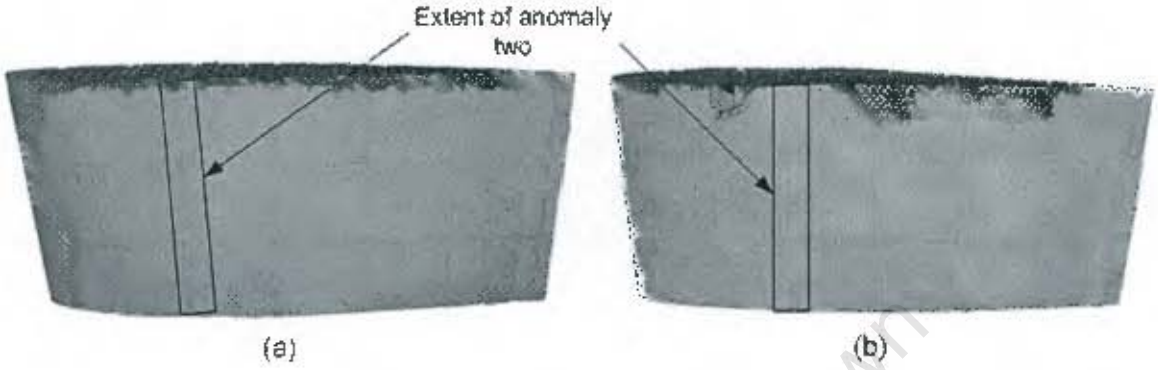

Figure 6.33: Extent of anomaly two on: (a) side A and (b) side B of the blade

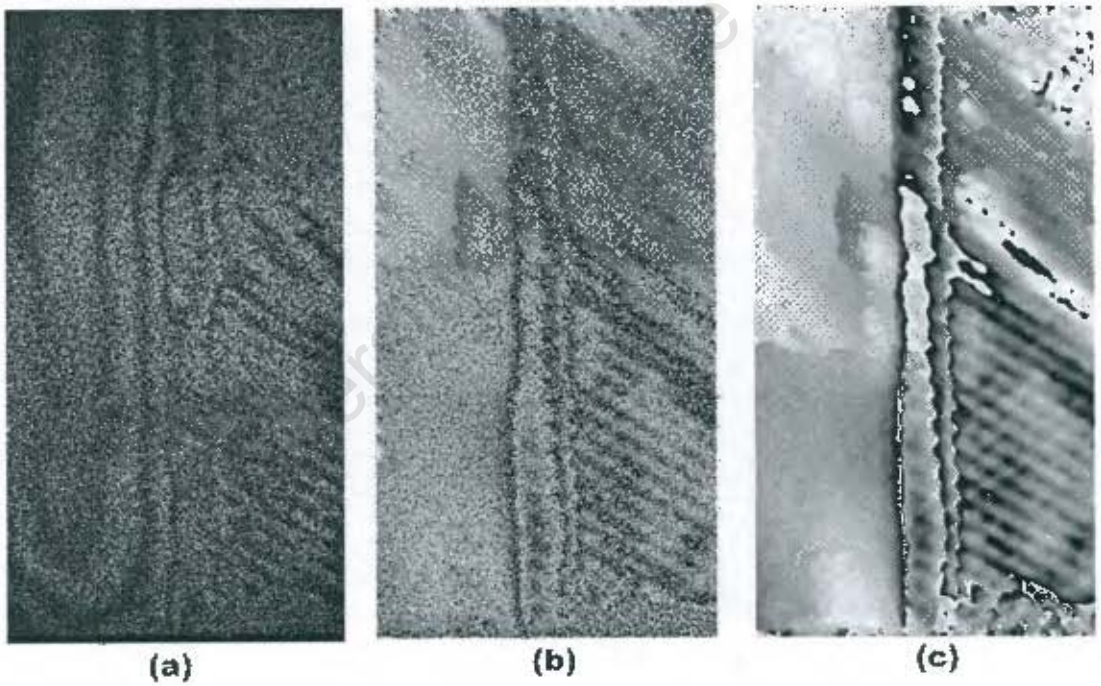

Figure 6.34: Fringe patterns of anomaly two, side A, using: (a) Shearography, (b) Phase-stepping and (c) filtering.

Figure 6.34(a) depicts the Shearographic fringe pattern of anomaly two. It can be seen that the fringes are dense in the center of the image and look very similar to the fringe patterns of anomaly one. Figure 6.34(b) and (c) show Phase-Stepped Shearographic and phase filtered fringe patterns of anomaly two on side A. The fringe patterns of anomaly two on side B can be seen in figure 6.31(a)-(c).

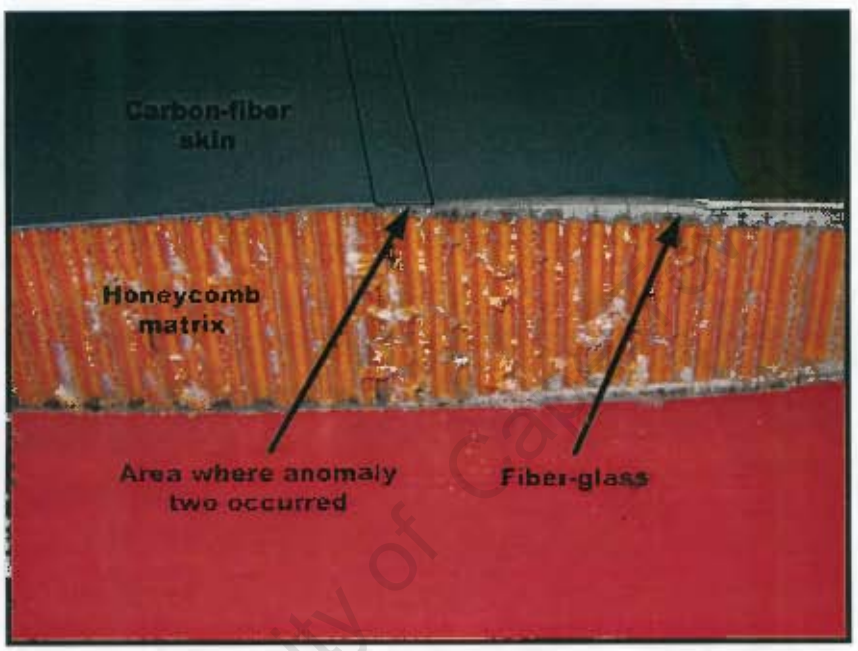

Figure 6.35: Picture showing the change in composition of the blade, where anomaly two occurred.

This anomaly occurs on both sides of the blade and is perfectly perpendicular to the bottom edge of the blade. Therefore, it is highly unlikely that it is a defect in that it is so well shaped. Under close inspection, it was realized that anomaly two occurs where the composition of the blade changes in that the leading edge is filled with fiber glass to increase strength and also covers approximately a quarter of the blade's surface. It can be seen from figure 6.35 that anomaly two occurs where the fiber-glass sheet stops therefore producing an anomaly that is perpendicular to the width of the blade.

6.5.4 Anomaly Three

Anomaly three occurred along the entire length of the trailing edge, on both sides of the blade and is due again to a change in composition. Figure 6.36 shows the extent of the anomaly.

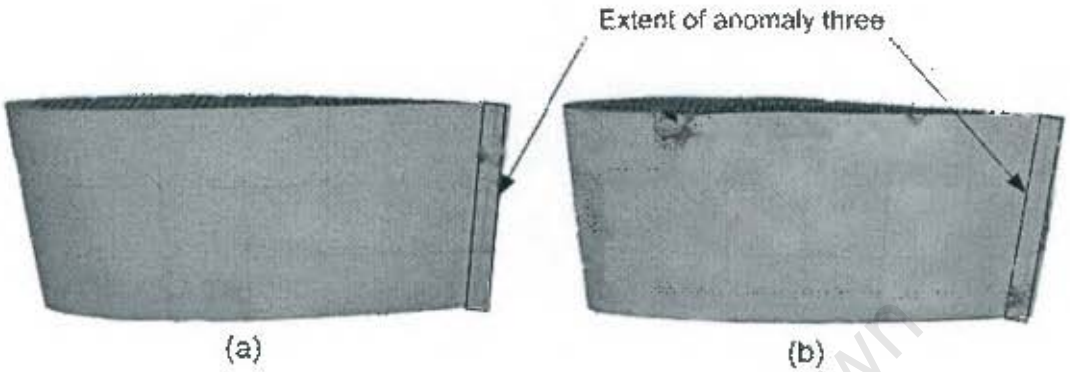

Figure 6.36: Extent of anomaly three on: (a) side A and (b) side B of the blade

The Shearographic fringe pattern of anomaly three on side B is shown in figure 6.37(a). It can be seen that there is localized displacement gradient running parallel to the trailing edge of the blade. Furthermore, the fringes become denser two thirds from the bottom of the picture. The increase in density of fringes at this point is due to a stress concentration which results from a spacing between the aluminium strips that balance the blade as shown in figure 6.38.

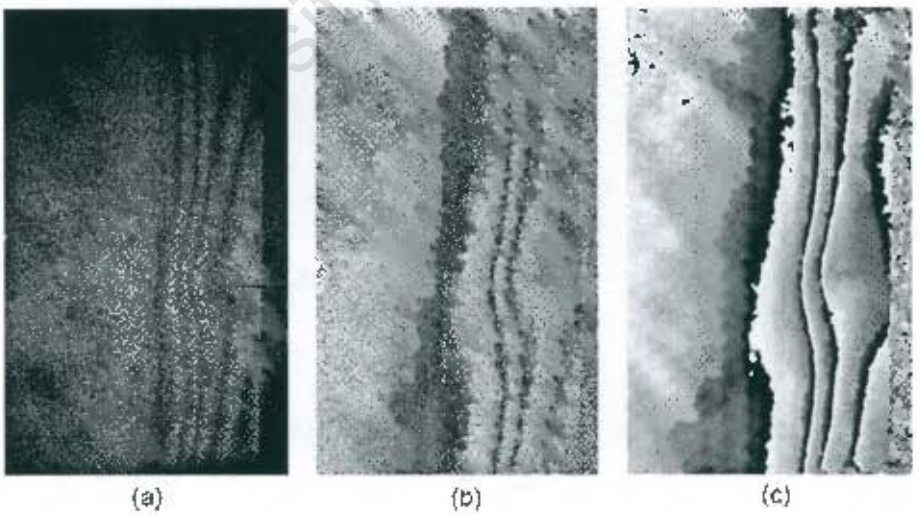

Figure 6.37: Fringe patterns of anomaly three, side B, using: (a) Shearography, (b) Phase-stepping and (c) filtering.

Figure 6.37(b) and (c) depicts the Phase-stepped Shearography and phase filtered fringe patterns of anomaly three respectively. The bulging of the fringes and the increase in frequency at the stress concentration can be clearly seen from the fringe patterns of figure 6.37(b) and (c). This illustrates how Shearography can also be used to find stress concentrations in manufactured parts as it measures the strain of the material not the displacement.

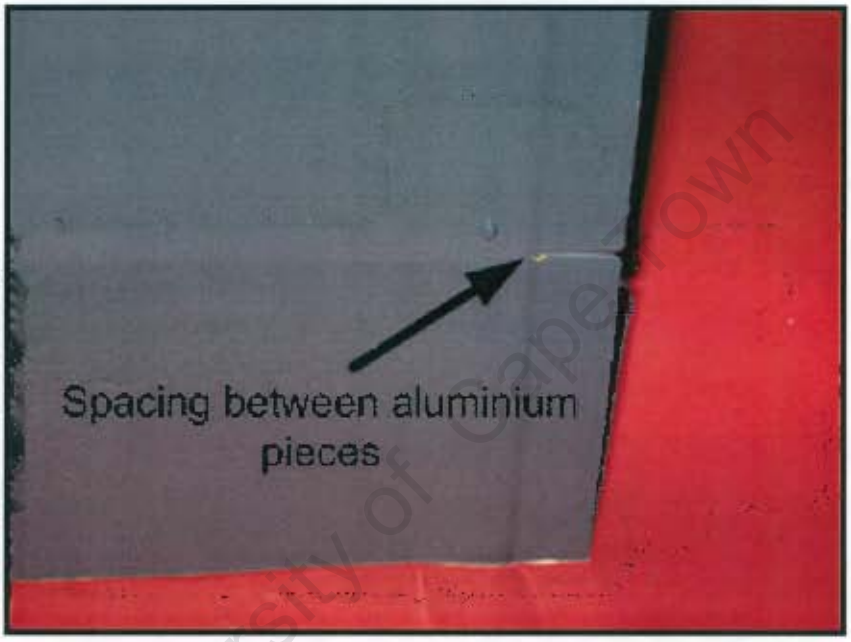

Figure 6.38: Picture of the spacing between aluminium strips on the trailing edge of the blade.

The manifestation of the fringes occurred once again due to a change in composition of the blade. The trailing edge of the blade tapers with the blade first being made up of aluminium and fiber-glass and then narrowing down into aluminium only as shown in figure 6.39. This also explains why there are so many fringes in that the aluminium is a thin plate absorbing a lot of heat resulting in a high temperature gradient when reaching the thicker part of the blade containing fiber-glass.

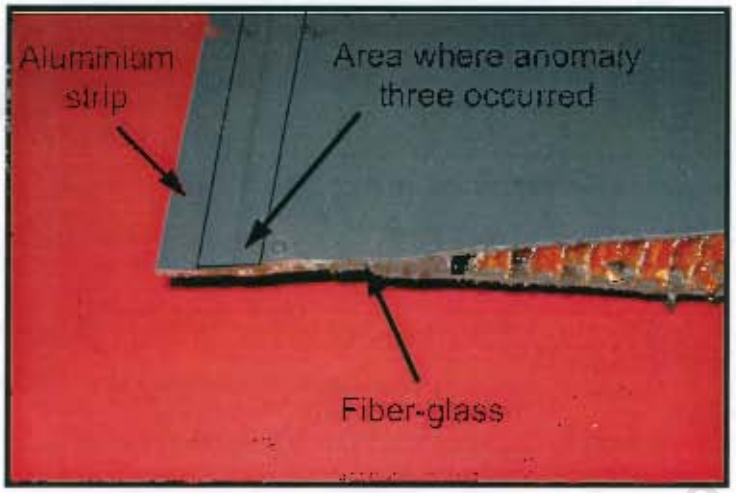

Figure 6.39: Picture showing the change in composition of the blade, where anomaly three occurred.

6.5.5 Anomaly Four

Anomaly four occurred along the entire length of both sides of the blade at approximately 400mm away from the leading edge. The extent and position of the anomaly is shown in figure 6.40.

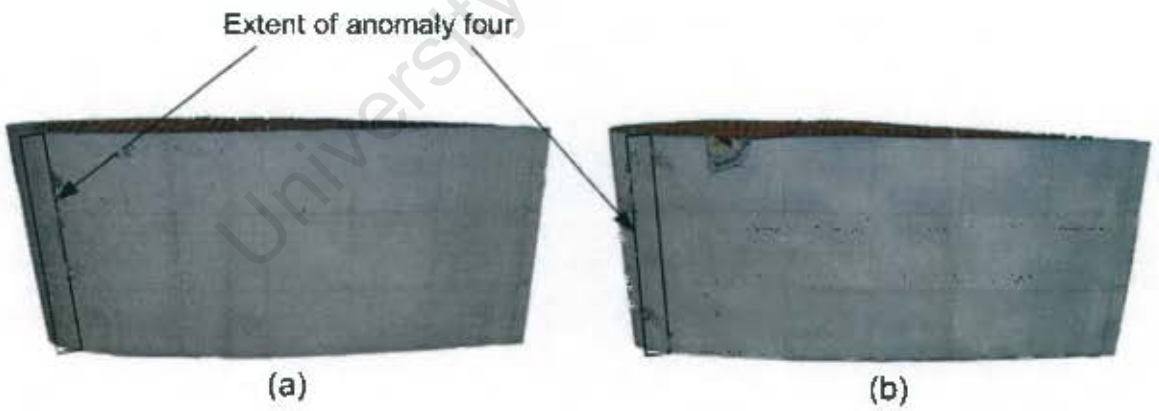

Figure 6.40: Extent of anomaly four on: (a) side A and (b) side B of the blade

Figure 6.41(a) depicts the Shearographic fringe pattern of anomaly four. It can be seen that the fringes are elliptical in shape with the complete elliptical fringe marking the cause of the anomaly. Small half circles can be seen at the bottom of the picture distorting the large

fringes, which is due to delaminations that where brought about when the blade was cut. The minor delaminations as well as the large elliptical fringe can be seen more clearly in figure 6.41(b) and (c).

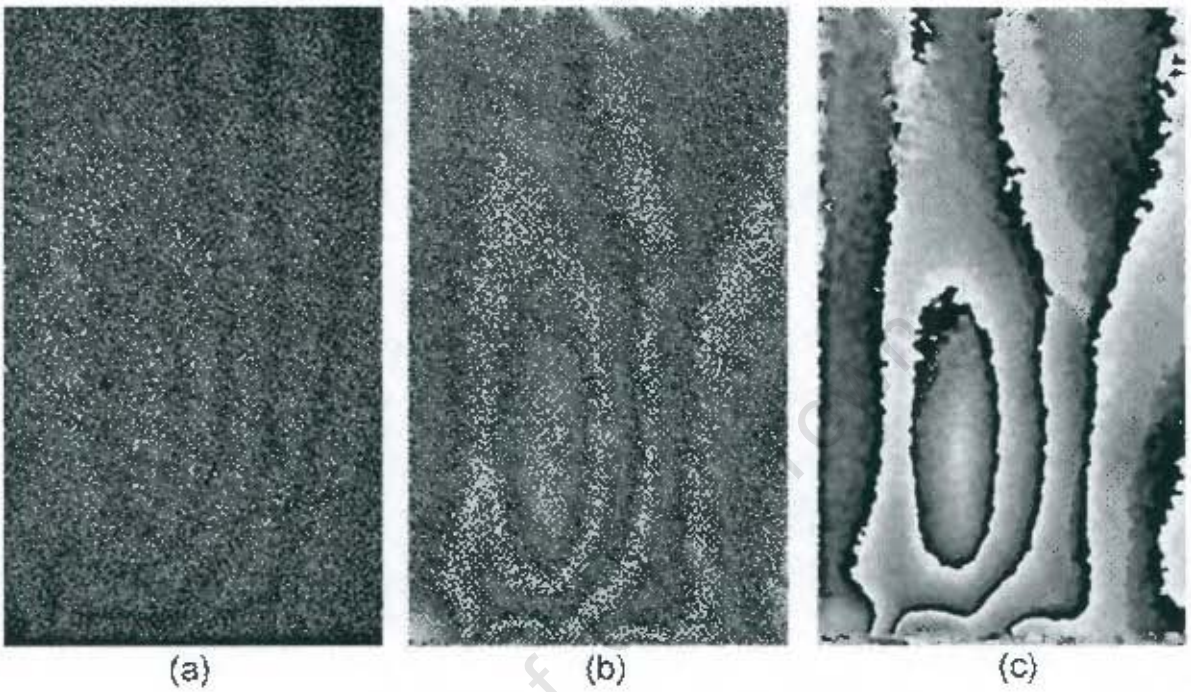

Figure 6.41: Fringe patterns of anomaly four, side A, using: (a) Shearography, (b) Phase-stepping and (c) filtering.

Subsequent to cutting around the anomaly it was found that it was caused due to a large piece of fiber-glass that fills in the leading edge of the blade. This helps to strengthen the blade against impact damage. Figure 6.42 is a picture of the cut piece of the blade. It can be seen from figure 6.42 that the wall of the leading edge is relatively thick making it difficult to detect a change in composition resulting in elliptical fringes rather than vertical fringes as in anomalies one and two.

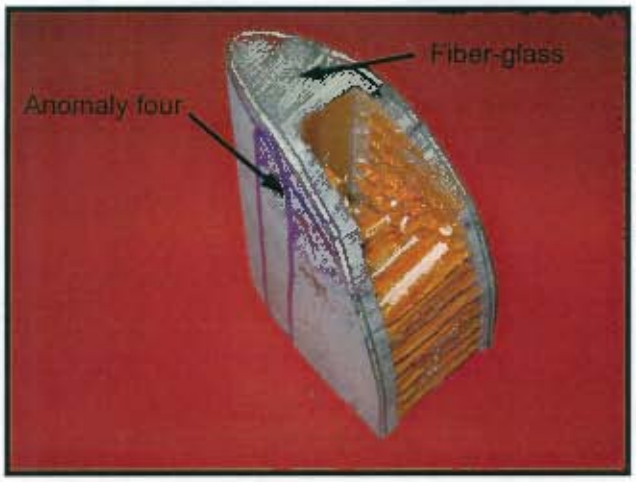

Figure 6.42: Picture of the leading edge showing the fiber-glass fill

6.5.6 Anomaly Five

Anomaly five was a result of the visible defect on side B of the blade as shown in figure 6.43.

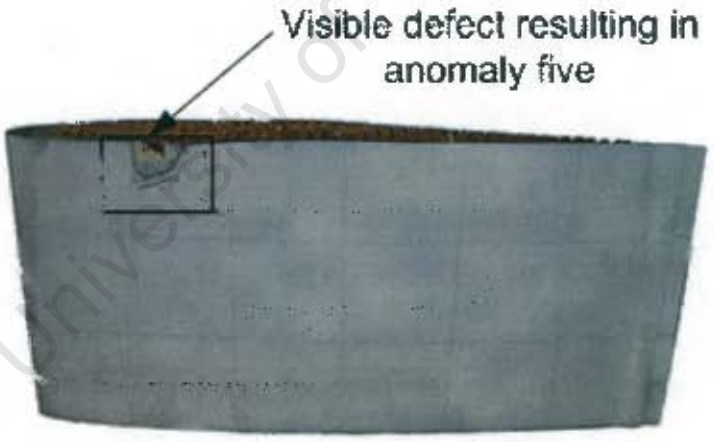

Figure 6.43: Picture showing the visible defect on side B of the blade

Figure 6.44: Fringe patterns of anomaly five, side B, using: (a) Shearography, (b) Phase-stepping and (c) filtering.

Figure 6.44(a) depicts the Shearographic fringe pattern of anomaly five. The fringes in the center of the picture point to the visible defect. The full extent of the fringes of the defect cannot be seen as it lies between anomaly one and two. The vertical dense fringes on the left and right of the defect are anomalies one and two respectively. In figure 6.44(b) and (c) the dense and irregular shaped fringes can be seen more clearly indicating the position of the defect. Judging from the pictures no internal damage was caused by the impact.

6.5.7 Anomaly Six

Anomaly six is a delamination which probably resulted from the cutting the blade, as it is found on the bottom of the blade as shown in figure 6.27. Figure 6.45(a) depicts the Shearographic fringe pattern of the delamination. The half elliptical fringes can be seen in figure 6.45(a) with three fringes forming in the Phase-Stepped Shearographic and phase filtered images of figure 6.45(b) and (c) respectively. Close examination of the defect area showed no signs of the defect being anything else but a delamination.

Figure 6.45: Fringe patterns of anomaly six, side B, using: (a) Shearography, (b) Phase-stepping and (c) filtering.

7. CONCLUSIONS

The following conclusions can be made based on the results of the investigation:

1. The compact Shearographic system is capable of detecting the presence and location of defects in composite structures. Furthermore, the device can differentiate between defects of varying depth by manifesting the appropriate number of fringes.

2. The number of fringes that can be manifested by a flaw is dependant on the period of stressing (when using heating or cooling techniques) as well as the amount of time before the fringe pattern is captured by the user. Therefore when a comparison between defects is made, it is important to uniformly stress the object. It is also important to capture the images after stressing in the same period of time, otherwise the comparison will be incorrect.

3. The correct amount of laser illumination is important when measuring the displacement gradient of an object. An abundance of laser light saturates the pixels of the CCD detector resulting in those pixels not contributing to the measurement of the displacement gradient. On the other hand, insufficient laser light makes it difficult for the phase to be extracted resulting in fringes that are not well contrasted and not clearly visible.

4. The field of view of the Shearographic system is a function of the optical configuration and the available laser illumination. The Shearographic system is capable of using CCTV lenses of different focal lengths and has an optical field of view of 57 degrees when using the 8.5mm focal length CCTV lens. Therefore the only variable that limits the field of view of the device is the available laser illumination. Laser light is normally available in collimated "pencil like" beams. This beam must be expanded using suitable optics to cover the required surface area. However, the more one expands the beam, the lesser the illumination intensity becomes, a fact that can only be remedied by using a higher laser power.

5. The MTF rating of a lens, which can be manipulated by adjusting the aperture of a lens, affects the contrast and fringe definition of a fringe pattern. Reducing the size of the aperture of a lens increases the MTF and improves the contrast and resolution of a fringe pattern.

8. RECOMMENDATIONS

In view of the results and conclusions, the following recommendations can be made:

1. The compact Shearographic system has been successfully tested under laboratory conditions; further work should be done to make the device fully portable so that testing can be done under field conditions to confirm that the results will be still satisfactory.

2. The only variable that limits the field of view of an inspection area, using the proposed Shearographic system is the laser power. Therefore, further studies should be done to determine if two lasers of the same power can be used simultaneously or if a higher power laser can be made portable to improve light distribution and intensity.

3. Another method of increasing the field of view of inspection is to use a CMOS (Complementary Metal Oxide Semiconductor) camera[32] instead of a CCD camera. The CMOS camera allows the user to program the dynamic range of each pixel independent of each other whereas the CCD camera has a limited dynamic range, which means that a CMOS-sensor can gather more light than a conventional CCD-detector under the same illumination conditions. Therefore a comparative study should be done to determine the light efficiency and image quality of the fringe patterns, when using a CMOS camera and a CCD camera.

REFERENCES

1. D Findeis, J Gryzagoridis, *Inspection of Aircraft Components with the aid of Portable digital Shearography*, www.ndt.uct.ac.za (2005).

2. D Findeis, J Gryzagoridis, *Inspecting Glassfibre Reinforced Plastic Piping using Portable ESPI and Shearography*, www.ndt.uct.ac.za (2005).

3. D Findeis, J Gryzagoridis, *The feasibility of Optical Interfernce-based NDE Methods to Inspect Helicopter RotorBlades* , www.ndt.uct.ac.za (2005).

4. Y Y Hung, *Digital Shearography versus TV-holography for Non-Destructive Evaluation*, Optics and Lasers in Engineering volume 26 (1997), pp 421-436.

5. Y Y Hung, *Application of Digital Shearography for Testing of Composite Structures*, Composites: Part B 30 (1999), pp 765-773.

6. T Mayer, D Scherling, J Sun, *Shearography Testing on Aerospace CFRP Components*, NDT.net vol. 8 No.2 (2003).

7. R Krupa, T Walz, A Ettemeyer, *Industrial Applications of Shearography for Inspection of Aircraft Components*, NDT.net Vol. 8 No.2 (2002).

8. D Findeis, J Gryzagoridis, *Non-Destructive Testing of Composites using Portable Laser Based Methods*, www.ndt.uct.ac.za (2005).

9. Y Y Hung, *Shearography: A novel and practical approach for non-destructive testing*, Journal of Nondestructive Testing Vol. 8(2) (1989), pp 55-67.

10. W H Steel, *Interferometry, 2nd Edition*. Cambridge University Press, 1967.

11. P Hariharan, *Optical Interferometry*, Academic Press Australia,1985.

12. Various authors, *ASM Handbook vol. 17: Non-destructive Evaluation and Quality Control*, American Society for Metals, 1989.

13. J R Myles, *Electronic Speckle Pattern Interferometry (ESPI) NDE of Cracks in Pressure Vessels with FEA Modeling*, University of Cape Town Library, 1997.

14. Y Y Hung, *A phase shift technique for automation of phase determination in Digital Shearography*, Proceedings of 1994 SEM Spring Conference (1994), pp 233-240.

15. A Andhee, D Findeis, J Gryzagoridis, *Comparison of Normal and Phase Stepping Shearographic NDE*, Proceedings of SPIE volume 5767 (2005), pp 37-47.

16. Y Bar-Cohen, *In-Service NDE of Aerospace Structures – Emerging Technologies and Challenges at the End of the 2nd Millennium*, NDT.net Vol. 4 No. 9 (1999).

17. L X Yang, Y Y Hung, *Digital Shearography for Nondestructive Evaluation and Application in the Automotive and Aerospace Industries*, NDT.net (2005).

18. M Kalms, W Jueptner, *Mobile Shearography*, NDT.net Vol. 10 No.4 (2005).

19. S Waldner, S Brem, *Compact Shearography System for the Measurement of 3D Deformation*, Proceedings of SPIE vol. 3745 (1999), pp 141-148.

20. R Jones, C Wykes, *Holographic and Speckle Interferometry,2nd Edition*. Cambridge University Press, 1989.

21. C M Vest, *Holographic Interferometry*, John Wiley & Sons, Inc.,1979.

22. P K Rastogi, *Digital Speckle Pattern Interferometry and Related Techniques*, John Wiley & Sons, LTD,2001.

23. L Angel, MTebaldi and R Henao, *Phase-stepping Technique with an Electro-optic Crystal in Digital Speckle Pattern Interferometry*, Optics Communications 149 (1998), pp 235-238.

24. Ad AM Maas, PM Somers, *Two-Dimensional Convolution Applied to Phase-stepped Shearography*, Optics and Lasers 26 (1997), pp351-360

25. P A A M Somers, H van Brug, *Implementation of the Temporal Phase Unwrapping in a Real-time Phase Stepped Shearing Speckle Interferometer*, Proceedings of SPIE Vol.3993.

26. H A Aebischer and S Waldner, *A Simple and Effective Method for Filtering Speckle-Interferometric Phase Fringe Patterns*, Optics Communication 162 (1999), pp 205-210.

27. Melles Griot, *Optics Guide 4*,Copyright Melles Griot,1988.

28. J R Meyer-Arendt, *Introduction to Classical and Modern Optics*, 2^{nd}*Ed.*, Prentice-Hall International, Inc.,1972.

29. J D Cutnell, K W Johnson, *Physics fourth edition, John Wiley & Sons Inc.*,1997.

30. E Hecht, A Zajac, *Optics*, 2^{nd}*Ed.*, Addison-Wesley Publishing Company Inc.,1974.

31. F W Sears, M W Zemansky, *College Physics*, 3^{rd}*Ed.*.Addison-Wesley Publishing Company Inc.,1971.

32. H Manzke, M Kalms, E Rau, E Grauvog, *Improvement of the Applicability of Shearography under Aircraft Production and Maintenance Conditions*, NDT.net (2005).

BIBLIOGRAPHY

1. Y Y Hung, *Shearography and Applications in Nondestructive Evaluaution*, NDT.net (2005).

2. E J Tucholski, *Nondestructive Evaluations of Aromatic Polymide Insulated Aircraft and Spacecraft wiring*, NDT.net (2005).

3. G Tober, D Schiller, *NDT in Aerospace – State of Art*, NDT.net (2005).

4. J P Monchalin, *Optical and Laser NDT: A Rising Star*, NDT.net (2005).

5. K Habib, *Thermally induced deformations measured by Shearography*, www.sciencedirect.com (2005).

6. L Angel, M Tebaldi, R Henao, *Phase stepping in Lau interferometry*, Optics Communications vol. 164 (1999), pp247-255.

7. N Metchkarov, V Sainov, P Boone, *High-accuracy surface measurement using laser-diode phase-stepping interferometry*, Vacuum vol. 58 (2000),pp464-469.

8. D Findeis, J Gryzagoridis, *Comparison of the capabilities of portable Shearography and portable Electronic Speckle Interferometry*, Proceedings of SPIE vol. 5393 (2004), pp41-49.

9. M J Huang, C Lai, *Phase Unwrapping Based on Parallel Noise-immune Algorithm*, Optics and Laser Technology vol. 34 (2002), pp 457-464.

10. M Young, *Optics and Lasers*, 4th Edition, Springer-Verlag Berlin Heidelberg, 1977.

11. K J Gasvik, *Optical Metrology*, John Wiley and Sons, 1987.

APPENDIX A

1. Optics Background Information

1.1 Fundamentals of Optics

This section defines the necessary planes and points that are required to characterize a lens. Figure 1.1 below is a schematic of a lens having spherical surfaces and surrounded by air. Under these conditions the distances labeled f are equal even if the lens was not symmetrical. However f_f (front focal length) and f_b (back focal length) will only be equal if the lens is symmetrical.

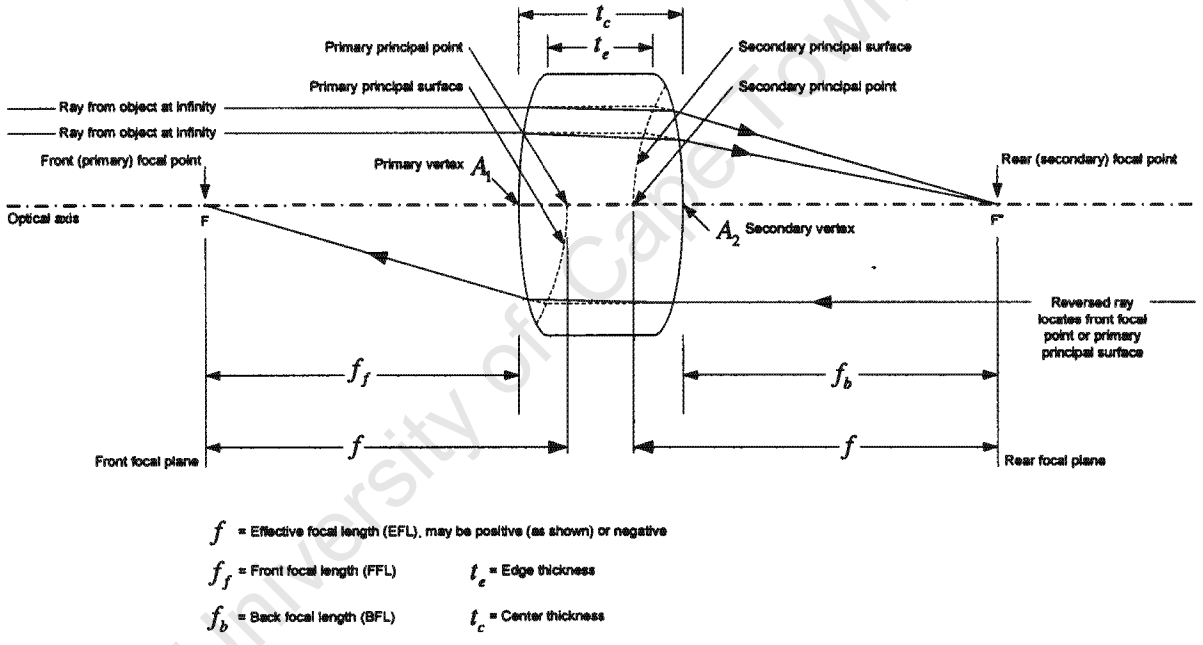

Figure 1.1: The important planes and points that characterizes a lens[27]

1.1.1.1 Focal Length

There are two distinct types of focal lengths namely; effective focal length (EFL) and the back focal length (BFL). The EFL, which is the more important of the two, is used to calculate magnification and is frequently used in all lens formulas. The effective focal length (denoted as *f*) is the distance between the principal point and the focal point as shown in figure 1.1. The principal point, as seen in figure 1.1, is usually inside the lens and therefore it is more practical to use the back focal length, which is the distance between the rear focal point and the secondary vertex of the lens. The front focal length (FFL) is the same as the back focal length except that the front of a lens is defined as the side of the lens that is closest to the object plane.

1.1.1.2 Focal Point

Parallel rays originating from one side of a lens will always traverse the focal point on the other side of it. This fact is the basis of locating the focal point.

1.1.1.3 Primary Principal Plane (or Surface)

The principal plane is a hypothetical surface and is defined as the loci where refraction is assumed to occur without reference as to where it actually does occur[28]. The point where the primary plane, which is actually a slightly curved surface, intersects the optical axis is known as the primary principal point. The secondary principal plane (or surface) is analogous to the primary principal plane. However, the primary principal plane is always the plane closest to the object plane.

1.2 Image Formation by a Converging Lens

The position of an image plane as well as the magnification of an image is dependant on the distance of the object from the focal point of a lens. It can be seen from figure 1.2 that if the object is beyond the *2f* point (i.e. a distance of two times the focal length) then the image will be real, inverted and smaller than the object.

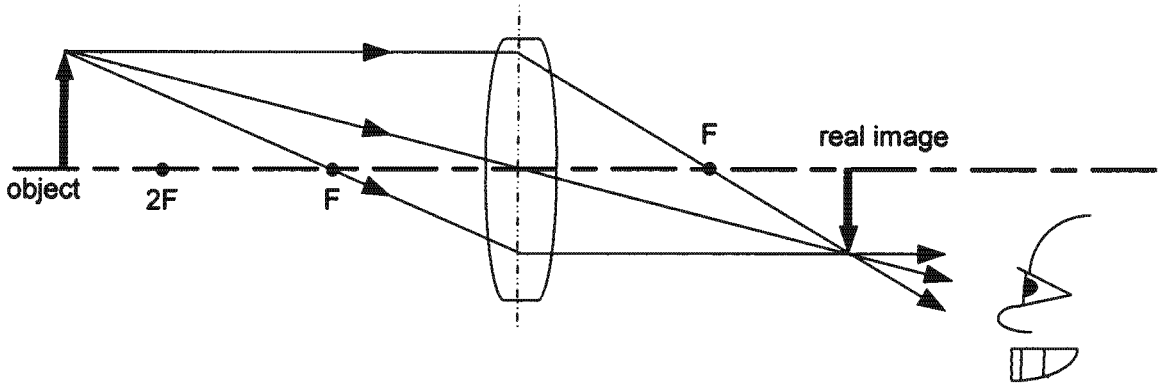

Figure 1.2: Object is placed beyond 2F [29]

If the object is between *f* and *2f* as shown by figure 1.3, then the image will still be real and inverted, but the image will be larger than the object.

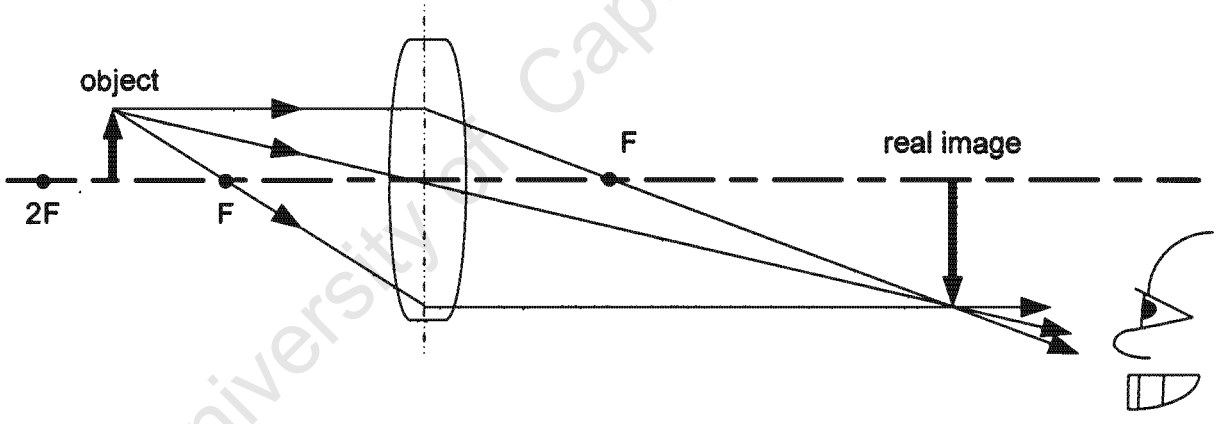

Figure 1.3:Object is placed between 2F and F [29]

Objects located between the focal point and the lens as shown by figure 1.4 will form a virtual image that is larger than the object. The virtual image is formed due to the rays diverging after traversing the lens. To a person viewing these diverging rays, they would appear to come from an image behind the lens, as in the case of a magnifying glass.

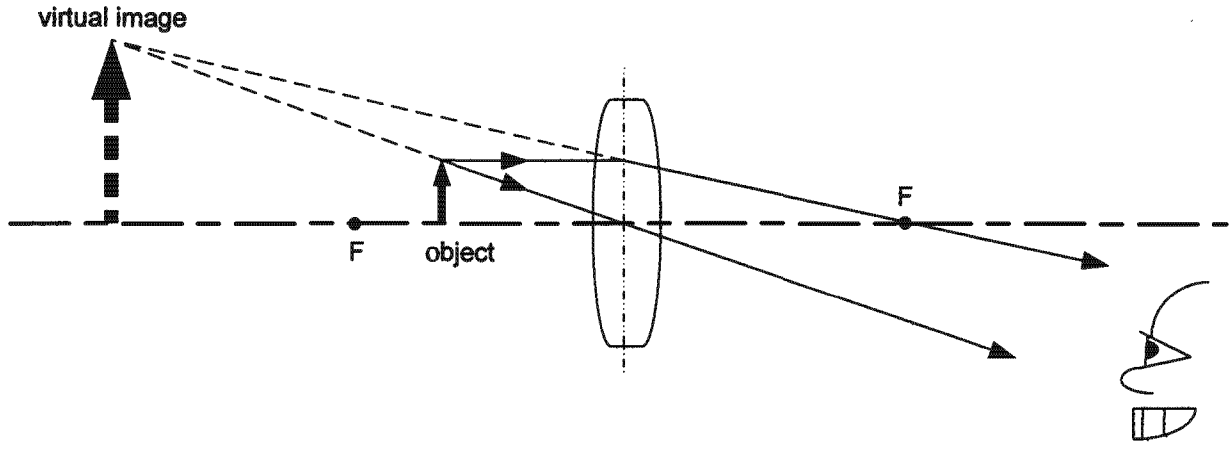

Figure 1.4: Object is placed between F and the lens[29]

Each point on an object emits light in all directions in a form of spheres with the rays being perpendicular to these spheres. However, when an object is infinitely far away in comparison to the focal length of the lens, the rays become parallel or collimated and will come to focus at the focal plane (as shown in figure 1.5). Figure 1.6 shows that the reverse is also true, that if light originates at the focal point then it will become collimated. The collimated rays can only be refocused if another lens is placed on the left of figure 1.6 (i.e. in the parallel ray field) so that the rays will converge (as shown in figure 1.5) and create an image in the focal plane of the added lens.

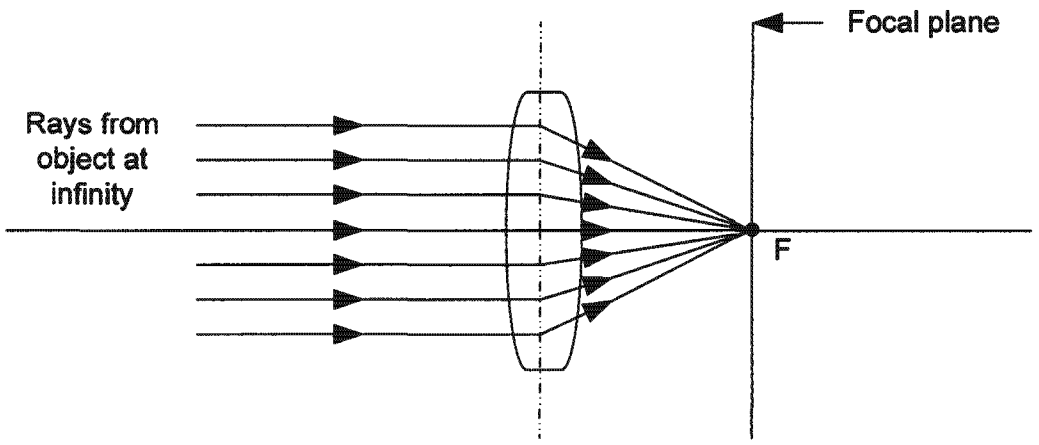

Figure 1.5: Object at infinity

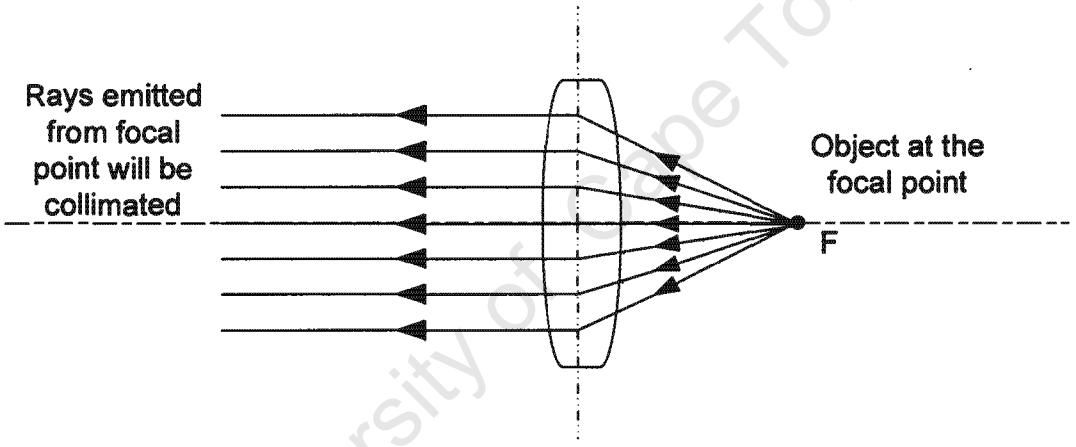

Figure 1.6: Object at the focal point

1.3 The Thin-Lens Equation and the Magnification Equation

For an object in front of a thin-lens, it is possible to determine the location, size and nature of the image by using the technique of ray tracing or by applying the thin-lens and magnification equations. A lens is defined as thin if its thickness is much less than the radii of curvature of its two surfaces. Ray tracing can only be done with the use of Snell's law which is used to calculate the angle of refraction of light as it travels through media of differing density and is

the fundamental principle upon which the thin-lens and magnification equations are based. Snell's law is discussed in greater detail in section 1.5. The thin-lens equation is as follows[29]:

$$\frac{1}{d_o}+\frac{1}{d_i}=\frac{1}{f} \tag{2.1}$$

Where d_o is the object distance, d_i is the image distance and f is the effective focal length of the lens. These variables are illustrated more clearly in figure 1.7. It can be seen from equation (2.1) that if the object distance and the effective focal length are known then the image distance can be calculated. The magnification equation is as follows[29]:

$$m=\frac{image\ height}{object\ height}=\frac{h_i}{h_o}=-\frac{d_i}{d_o} \tag{2.2}$$

The magnification can be calculated either by using the object and image height or the object and image distance. The thin-lens and magnification equations can be used for thin-lenses or for paraxial rays, which are rays that are very close and parallel to the optical axis. In this region lens surfaces are always very nearly normal to the optical axis and hence all angles of incidence and refraction are small. Furthermore in equation (2.1) it is assumed that the lens is in air and therefore the thin-lens equation cannot be used if the lens is placed in a different medium (e.g. water).

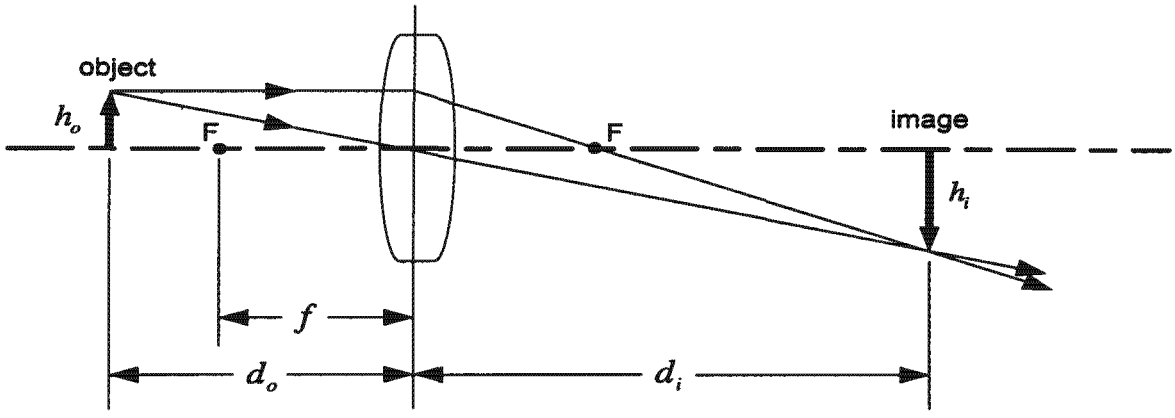

Figure 1.7: Schematic of the variables in the thin-lens equation[29]

Certain sign conventions accompany the use of the thin-lens and magnification equations so that values calculated are correct and have better meaning. The sign convention is shown in table 1.1 and applies to light traveling from left to right for a real object.

Table 1.1: Summary of sign conventions for lenses[29]

Summary of Sign Conventions for Lenses
Focal length
f is + for a converging lens
f is – for a diverging lens
Object distance
d_o is + if the object is to the left of the lens (i.e. real object), as is usual
d_o is – if the object is to the right of the lens (i.e. virtual object), this only arises in combinations lenses
Image distance
d_i is + for an image (real) formed to the right of the lens by a real object
d_i is – for an image (virtual) formed to the left of the lens by a real object
Magnification
m is + for an image that is upright with respect to the object
m is – for an image that is inverted with respect to the object

1.4 Modulation Transfer Function (MTF)

The modulation transfer function (MTF) is an extremely important parameter influencing the resolving power of an imaging lens. The MTF of an imaging lens incorporates both contrast and resolution. Moreover it is a measure of the lens ability to transfer contrast at varying resolution levels from the object plane to the image plane.

The derivation of MTF can be explained by first defining contrast and it is defined by the following mathematical equation[30]:

$$Contrast \equiv \frac{I_{\max} - I_{\min}}{I_{\max} + I_{\min}} \tag{2.3}$$

Where I_{max} and I_{min} are the maximum and minimum intensities of light emitted from an object. If it is assumed that an object has a sinusoidal irradiance distribution, where irradiance is the power per unit area of light that is reflected of the object, then scanning across the object for a period of time will produce a sequence of alternating maximum and minimum irradiance as shown in figure 1.8. The mean irradiance can then be defined as follows[28]:

$$a = \left[\left(I_{\max} - I_{\min} \right) / 2 \right] + I_{\min} \tag{2.4}$$

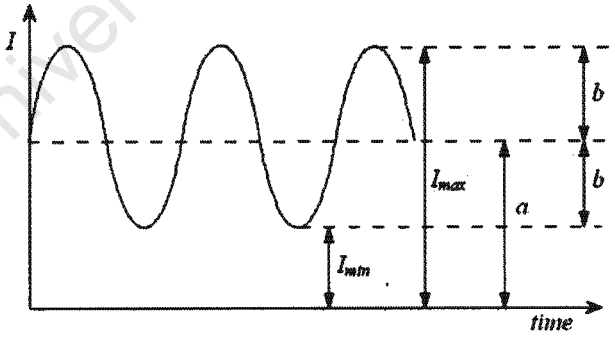

Figure 1.8: Sinusoidal irradiance distribution as a function of time[28]

The variation of the mean irradiance is as follows:

$$b = I_{max} - a \tag{2.5}$$

Modulation M can then be calculated as the ratio of a and b, and is mathematically described by equation (2.6), which is the variation of the mean irradiance over the mean irradiance.

$$M = \frac{b}{a} \tag{2.6}$$

However, when testing for performance one is not interested in the modulation of the object but rather in how much modulation is transferred from the object to the image. Hence it is the *modulation transfer factor* that counts. The modulation transfer factor T can be described by equation (2.7).

$$T = \frac{M_{image}}{M_{object}} \tag{2.7}$$

If the image modulation is half the object modulation, as depicted in figure 1.9, then T is equal to a half. The modulation transfer function however, is not a single value and varies with spatial frequency R. Therefore it is not called a transfer factor T but a transfer function $T(R)$ known as the modulation transfer function (MTF).

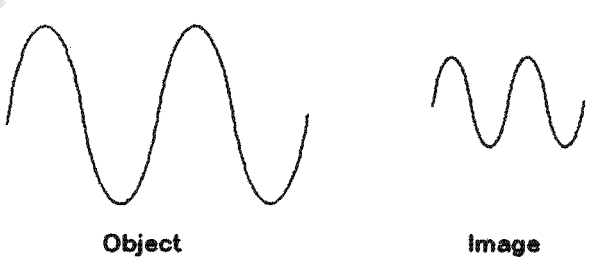

Figure 1.9: Contrast variation from object to image[28]

Spatial frequency refers to the number of line pairs per millimeter, where a line pair is a black and a white line. No lens at any resolution, even theoretically, can fully transfer contrast to an image due to the diffraction limit. Furthermore as the line pairs per millimeter increase (i.e. as the spatial frequency increases) it becomes increasingly difficult for contrast to be transferred as shown by figure 1.10. It can also be seen that image contrast is measured as a percentage of object contrast. Furthermore, black and white is 100% contrast and gray on gray is 0% contrast.

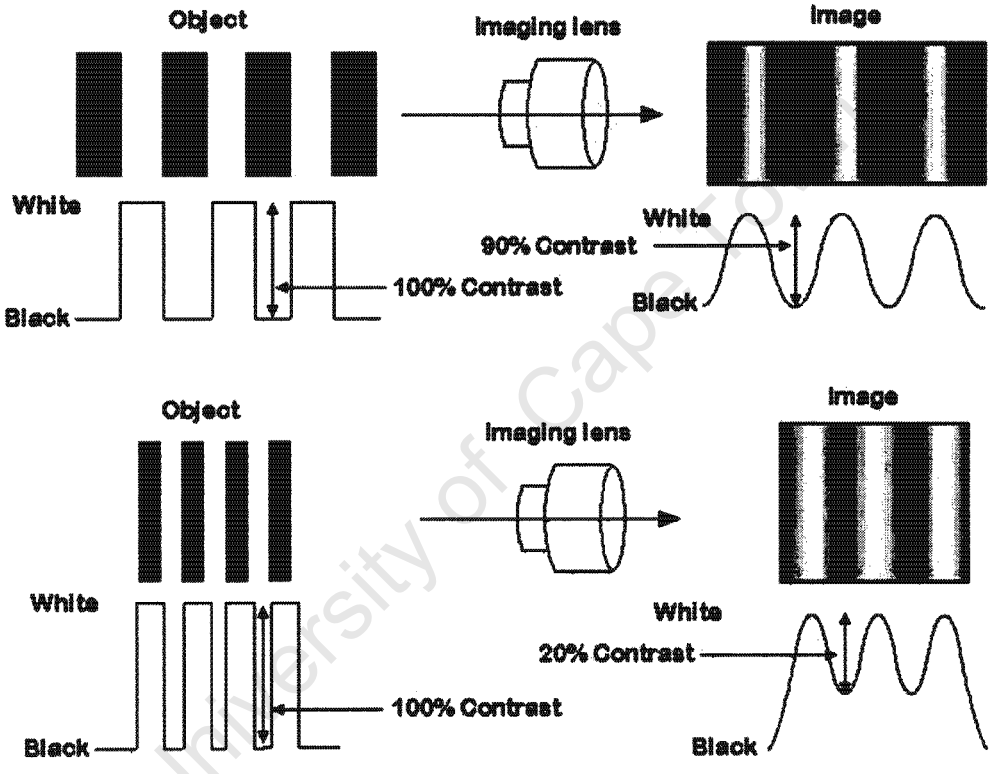

Figure 1.10: Increased frequency causes a lack of contrast

MTF graphs for commercial lenses can be obtained from companies like Edmund Industrial Optics who use an Optikos VideoMTF measurement system to plot MTF graphs of various lenses. A typical MTF graph is shown in figure 1.11 where the *y*-axis is the percentage of contrast and the *x*-axis is the frequency of the lines. It can be seen that the contrast drops as

the frequency increases; also the frequency is measured from image plane and not from the object surface.

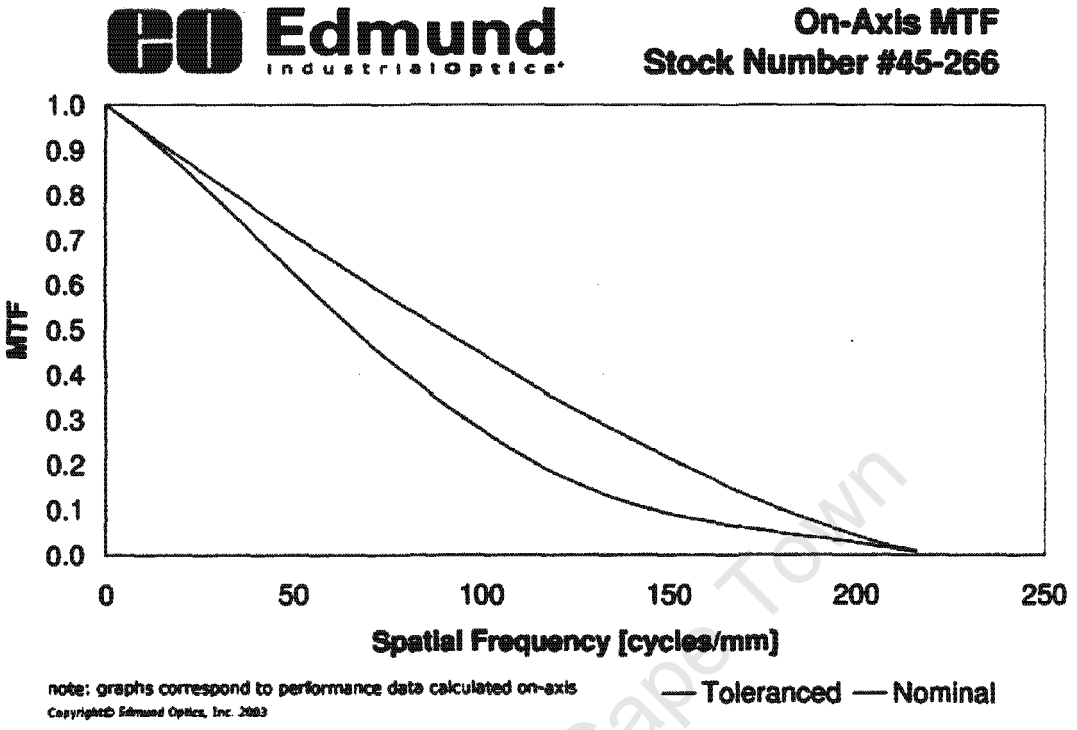

Figure 1.11: A typical MTF curve

MTF of a lens can however be manipulated by varying the aperture size and wavelength. The wavelength of light will not be taken into consideration as this investigation only uses monochromatic light. It can be seen from the MTF graphs in appendix D that a decrease in aperture size of a lens increases the contrast whereas larger apertures reduces the contrast. Other factors such as atmospheric haze, poorly manufactured lenses, scratches and contamination such as dust and fingerprints reduce resolution and contrast.

1.5 Aberrations

Aberrations are intrinsic shortcomings of a lens, even if the lens is made from the best glass and is free from manufacturing and other defects. This is due to the fact that in general, spherical lenses yield perfect imagery only in the paraxial region. However, by careful manipulation of a system's physical parameters (e.g. power, shape, thickness, glass type, the distance between lenses and the location of stops) these aberrations can be minimized[1]. Most aberrations occur with monochromatic or single wavelength light and are called *monochromatic aberrations*. Examples of monochromatic aberrations are spherical aberration, coma, oblique, astigmatism, curvature of field and distortion. The rest of the aberrations occur with polychromatic light or light that contains at least two wavelengths and examples of these are chromatic aberrations and lateral color. Monochromatic aberrations can be further divided into two categories namely; aberrations that cause blurring such as spherical aberration, coma and oblique astigmatism and those that cause dislocations such as curvature of field and distortion. Furthermore aberrations such as spherical and chromatic aberrations can act in two different directions (i.e. in the axial and lateral directions) and have their own causes and corrections.

For numerical analysis, aberrations can be handled along two general lines, considering either the rays or the wavefronts. In paraxial-ray tracing the imaging characteristics of a lens in a system can be determined by tracing many rays through the system and by applying Snell's Law at each interface that is encountered. The direction of a light ray after refraction at an interface between two homogenous, isotropic media of differing index of refraction is given by Snell's Law in equation (2.8) [27].

$$n_1 \sin\theta_1 = n_2 \sin\theta_2 \tag{2.8}$$

Where θ_1 is the angle of incidence θ_2 is the angle of refraction, and both angles are measured from the surface normal as is shown in figure 1.12. This means that in practice we can estimate the image quality of most optical systems by using certain approximations. The sine function in Snell's Law can be mathematically represented by the Taylor series expansion,

$$\sin\theta_i = \theta_i - \frac{\theta_i^3}{3!} + \frac{\theta_i^5}{5!} - \frac{\theta_i^7}{7!} + \frac{\theta_i^9}{9!} - \ldots\ldots\ldots \qquad (2.9)$$

Where the θ's are given in radians. However if only the first term is retained (i.e. it is assumed that $\sin\theta_i = \theta_i$), for simplification purposes, then this is known as first-order theory or paraxial theory. An aberration free optical system would form its image at a point and to the size indicated by the paraxial theory; though it is well known that this is an over simplification and that a perfect optical system does not exist. Paraxial theory is however used to determine system focal length, magnification, conjugate distances ...etc[27]. So another definition of aberrations would be how much the image differs from the paraxial prediction. Another way of getting a more accurate prediction is to take the third order terms of equation (2.9) into account and this is known as third-order theory. This theory was extensively investigated by Seidel and therefore third-order lens aberrations are called Seidel aberrations[27].

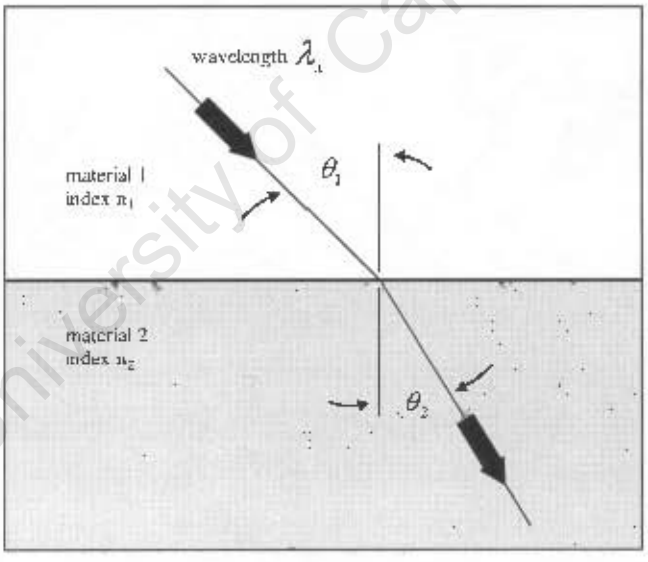

Figure 1.12:Schematic depicting Snell's Law[27]

If aberrations are numerically analyzed using wavefronts then it should be noted that wavefronts should be spherical to converge toward a point. However in terms of aberrations caused by image-blur, the light does not converge toward a point which means that the

wavefronts are not perfectly spherical: they are distorted. The distance by which the ideal reference sphere departs from the actual sphere, measured along the radius of the reference sphere, is called the *wave aberration*[28].

In curvature of field and distortion, the wavefronts are spherical but the spheres are displaced; the wavefronts come together but at the wrong point. Applying wave aberrations is advantageous in that the path difference of one surface can be directly added to the path difference of another surface in the optical system to find the total aberration present.

1.5.1 Spherical Aberrations

Spherical aberrations are caused by rays coming together at different foci as well as rays passing these foci at varying heights above the optical axis. Figure 1.13(a) illustrates how an aberration free lens focuses collimated light. It can be seen that all the rays pass through the focal point, but in reality these single element lenses do not behave in such a manner. It can be seen from figure 1.2(b) that the rays close to the optical axis, known as *paraxial rays*, come together at the focal point just like the aberration free lens. However, the outer rays of the lens known as the *marginal rays* come together before reaching the focal point. This means that the lens is *under-corrected* and if the marginal rays came together after the focal point then the lens will be *overcorrected*.

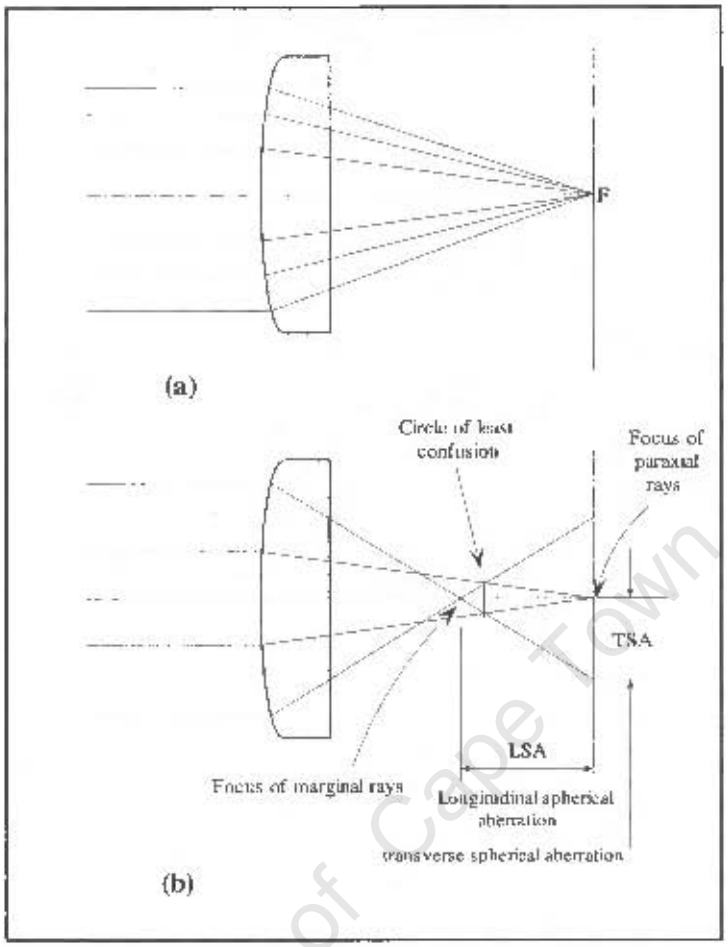

Figure 1.13: Spherical aberration of a plano-convex lens[27]

The distance along the optical axis between the intercept of the marginal rays and paraxial rays is known as the *longitudinal spherical aberration* (LSA) [30]. The *transverse spherical aberration* (TSA) is defined as the height above or below the optical axis where the marginal ray intersects the plane of paraxial focus[1]. The transverse spherical aberration is related to the longitudinal spherical aberration by the following equation[28],

$$TSA = LSA \tan \gamma \tag{2.10}$$

Where γ refers to the slope of the marginal ray. If a screen were to be put in place at the focus of the marginal rays one would observe that the marginal rays are in focus. The

paraxial rays at the same plane will form a diffuse disk as these rays are out of focus. The reverse will occur at the focus of the paraxial rays. The cross section of light with a minimum diameter between the marginal focus and the paraxial focus is called the circle of least confusion and this is where the sharpest image can be found.

To bring a set of parallel rays to the same focal point requires a lens surface of varying curvature since $\sin\theta$ is not truly equal to θ except at $\theta = 0^{\circ}$. High surface quality lenses are manufactured by grinding and polishing techniques, which can only produce spherical or cylindrical surfaces. Aspherical lenses are the only lenses with varying radii and are produced by molding. The disadvantage of this process is that these lenses have an inferior surface finish. Spherical aberration is dependent on the shape of a lens, its orientation and the conjugate ratio that is used. Furthermore, under certain conditions combining two or more spherical lenses can virtually eliminate spherical aberration. This can be done by combining simple positive lenses, which are under-corrected, with negative lenses, which are overcorrected for spherical aberration. Spherical aberration will be negligible in a system if the negative and positive elements within the system are nearly equal but opposite in magnitude in terms of spherical aberration. This is done in doublets where positive and negative lenses are cemented together to virtually eliminate spherical aberration.

1.5.2 Astigmatism

Astigmatism is an aberration that only occurs off-axis. Any object point that is a substantial distance away from the optical axis will cause a cone of rays starting at that point to strike the lens asymmetrically, giving rise to astigmatism. The word astigmatism comes from two Greek words namely: *a-*, which means not and *stigma-*, which means spot or point. The meaning of the word astigmatism therefore perfectly describes this aberration since the focal point of the lens develops into a three-dimensional focal figure known as a *conoid*.

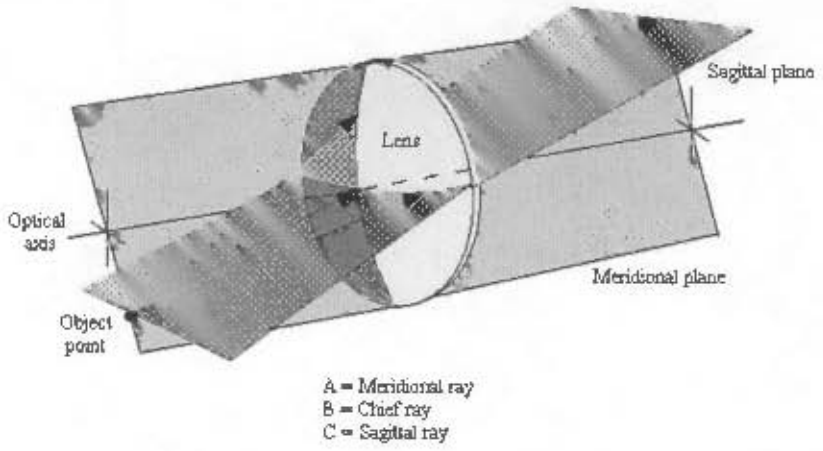

Figure 1.14: Imaging of an off-axis point[30]

Figure 1.14 above is a schematic of an optical system imaging an off-axis point. It can be seen that the *tangential* or *meridional plane* contains the optical axis and the object point. The rays radiating from the object point that lie on this plane are known as *tangential* or *meridional rays* except for the *chief ray* which starts from the object point and goes through the center of the lens. The *sagittal* or *radial plane* also contains the chief ray and is perpendicular to the meridional plane. All rays lying on the sagittal plane are known as skew or sagittal rays. The meridional plane's angle of slope stays constant as the meridional rays travel through the lens. However the sagittal planes slope changes as the chief ray is deviated at various elements. Therefore to be more accurate, one should imagine several sagittal planes with each plane illustrating the deviation of the chief ray at various elements.

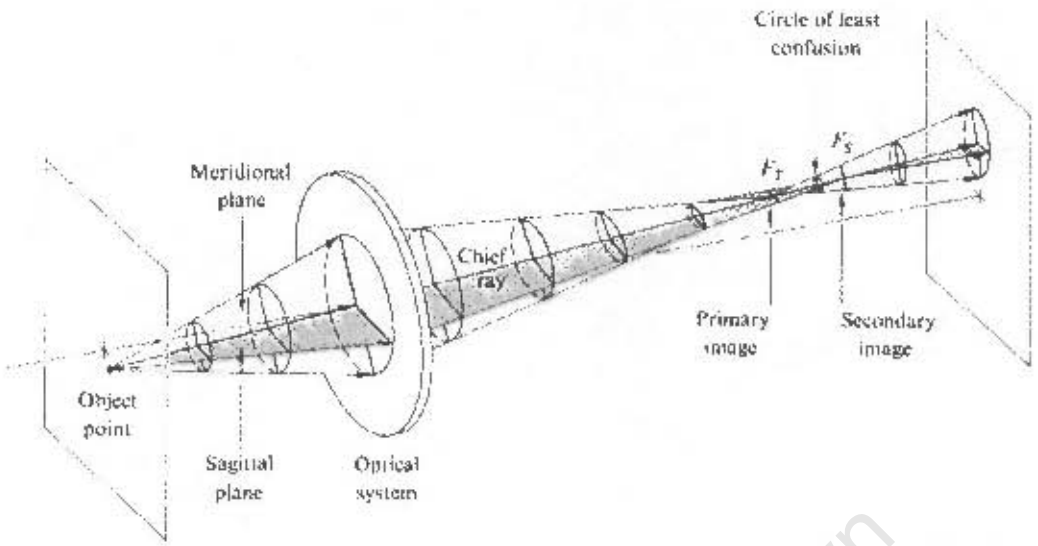

Figure 1.15: Imaging of an off-axis point illustrating astigmatism[30]

Astigmatism does not occur when the object point is on the optical axis since the cone of rays will be symmetrical when striking the surface of the lens. Therefore there is no need to make a distinction between the meridional and sagittal planes. This means that all focal lengths will be the same and that all rays will come together at a single point. However, this will only be true if spherical aberration is absent. In contrast, when imaging an off-axis point there will be two distinct planes namely the meridional and sagittal planes, which have differing focal lengths. The meridional rays focus closer to the lens than the sagittal rays forming a conoid as shown in figure 1.15. It can be seen from the schematic that as the cone of rays traverse the lens, deformation occurs in the meridional plane transforming the cross-section of beams into an ellipse. This is due to the meridional rays having a shorter focal length. The ellipse then degenerates into a line, known as the primary image, at the tangential or meridional focus. After this point the cross-section then grows and becomes circular at the point known as the circle of least confusion, which is a circular blur. Deformation of the circular cross-section then starts to occur in the sagittal plane, until once again the ellipse degenerates into a line, known as the secondary image, at the sagittal or radial focus. The separation of the meridional and sagittal conjugates is known as astigmatism.

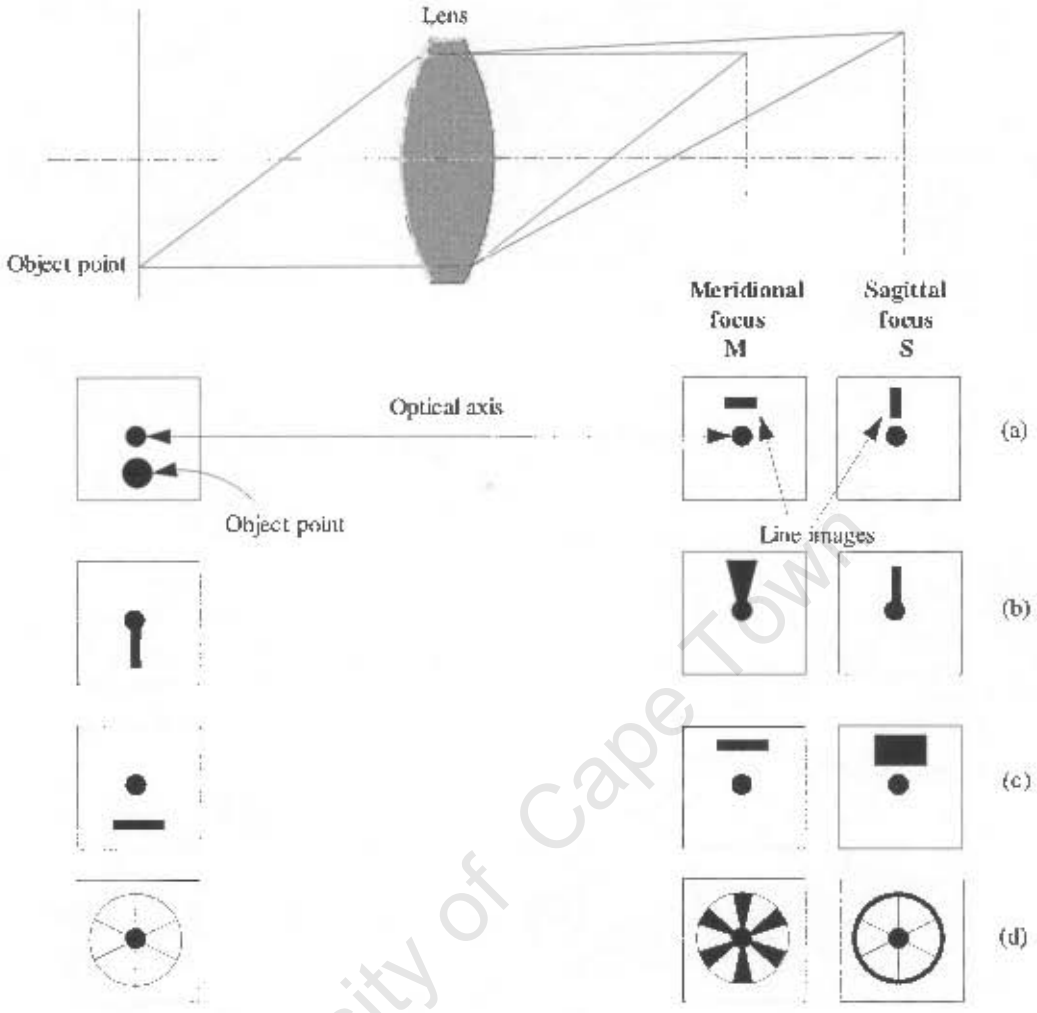

Figure 1.16: Distortion of images due to astigmatism[28]

The difference in focal length of the two planes is known as the astigmatic difference and as this difference increases (i.e. as the object point moves further from the optical axis), so does the diameter of the circle of least confusion. The increasing of the astigmatic difference also changes the orientation of the primary and secondary line image. However the primary line image will always be tangential to a circle drawn around the optical axis and the secondary line image will always be radial with respect to the optical axis. Figure 1.16 illustrates how this occurrence affects the imaging of an optical system. It can be seen from figure 1.16(a) that a point object, because of astigmatism, will be imaged as a tangential line at the meridional focus (M) and a radial line at the Sagittal focus (S). If the object is a radial line, as

shown by figure 1.16(b), then it will be blur at M and sharp at S. Tangential lines are sharp at M and blur at S, as depicted by figure 1.16(c). If the object is a wagon wheel then the rim (which is a sum of short tangential lines) will be sharp at M, while the spokes will be sharp at S.

Astigmatism depends mostly on conjugate ratios and lens shape only if the aperture in the system is not in direct contact with the lens itself. If an optical system does not contain an aperture or stop then it is the lens itself that serves as the aperture.

1.5.3 Coma

Coma, like astigmatism, occurs only when the object point is off-axis. It is also very similar to spherical aberration (SA) in that the ray bundle does not focus to a point. However, even if an optical system has been corrected for spherical aberration it will still exhibit coma. This aberration originates from the fact that the principal plane can only be treated as a plane in the paraxial region.

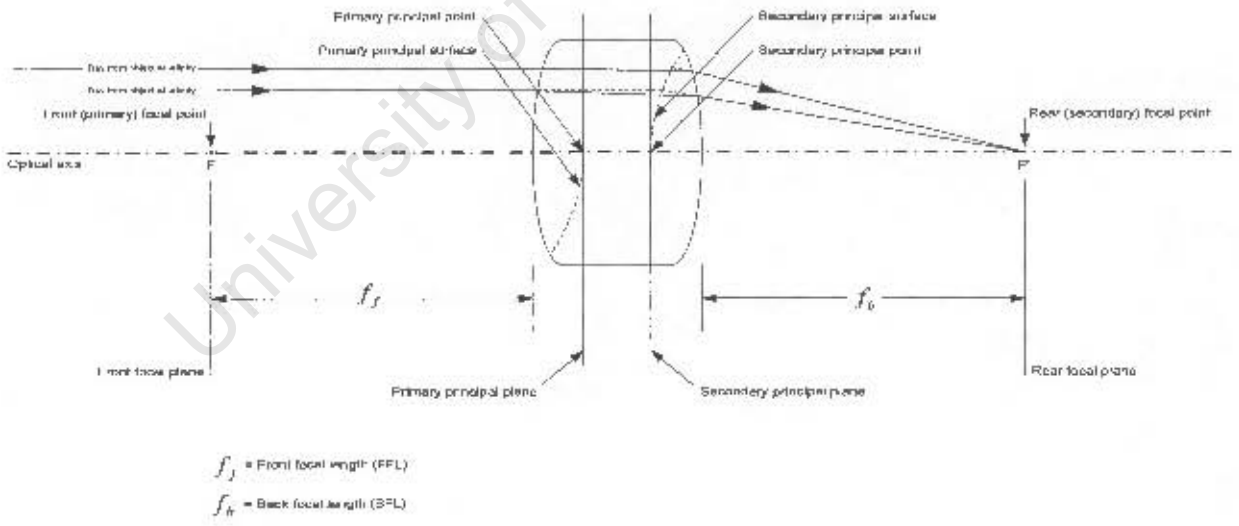

Figure 1.17: The principal plane

It can be seen from figure 1.17 that the principal plane is actually a principal curved surface. In the absence of spherical aberration this curved surface brings paraxial rays to a point at F'', a distance equivalent to the back focal length (BFL) of the lens from the vertex. The rays traversing the off-axis region of the lens will however have differing effective focal lengths at various points on the lens which in turn causes the magnifications at these various points to differ. This produces a blur in the image plane of off-axis object points as illustrated in figure 1.18. As a result, the off-axis object point is not imaged as a point but as a characteristic comet-like flare. It can also be seen from figure 1.18 that the outer ring is formed due to the intersection of marginal rays in which case the distance between 0 and 1 is known *tangential coma* and the distance from 0 to 3 on $\sum_i$ is termed the *sagittal coma*.

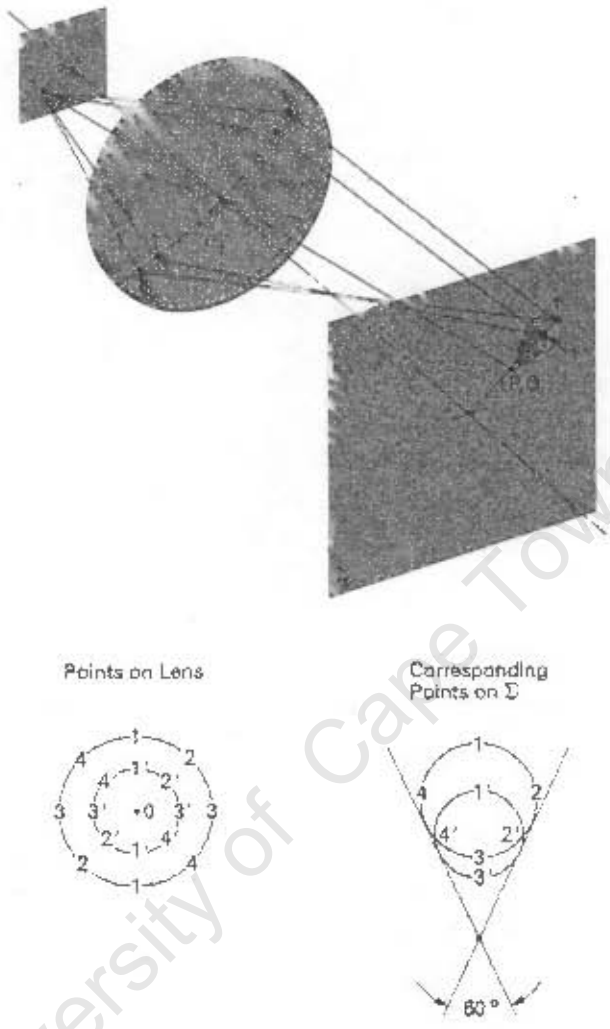

Figure 1.18: The affect of coma on an object point[27]

Coma can be positive or negative depending on whether the marginal rays come to a point closer or further away from the optical axis as compared to the inner rays. If the marginal rays come to a point closer to the optical axis than the inner rays then the coma is said to be negative as shown in figure 1.19(a). If the inner rays come to a point closer to the optical axis then the marginal rays then the coma is said to be positive as shown in figure 1.18 and 1.19(b).

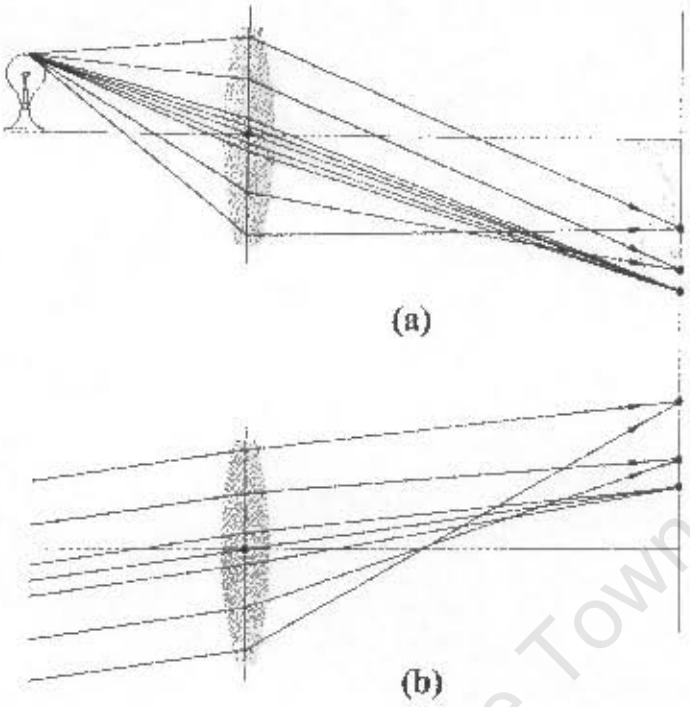

Figure 1.19: Negative and positive coma[30]

As with spherical aberration, coma can be corrected by using multiple surfaces or by changing the shape of the lens symmetric about a central stop. Figure 1.20 illustrates how various lens shapes affects coma. It can be seen that a concave positive-meniscus lens shape with an object at infinity has a large negative coma while the convex meniscus lens shape has a large positive coma. Therefore an equiconvex lens shape will produce negligible coma. The image quality can also be improved by judiciously placing an aperture or a stop in an optical system as to eliminate marginal rays.

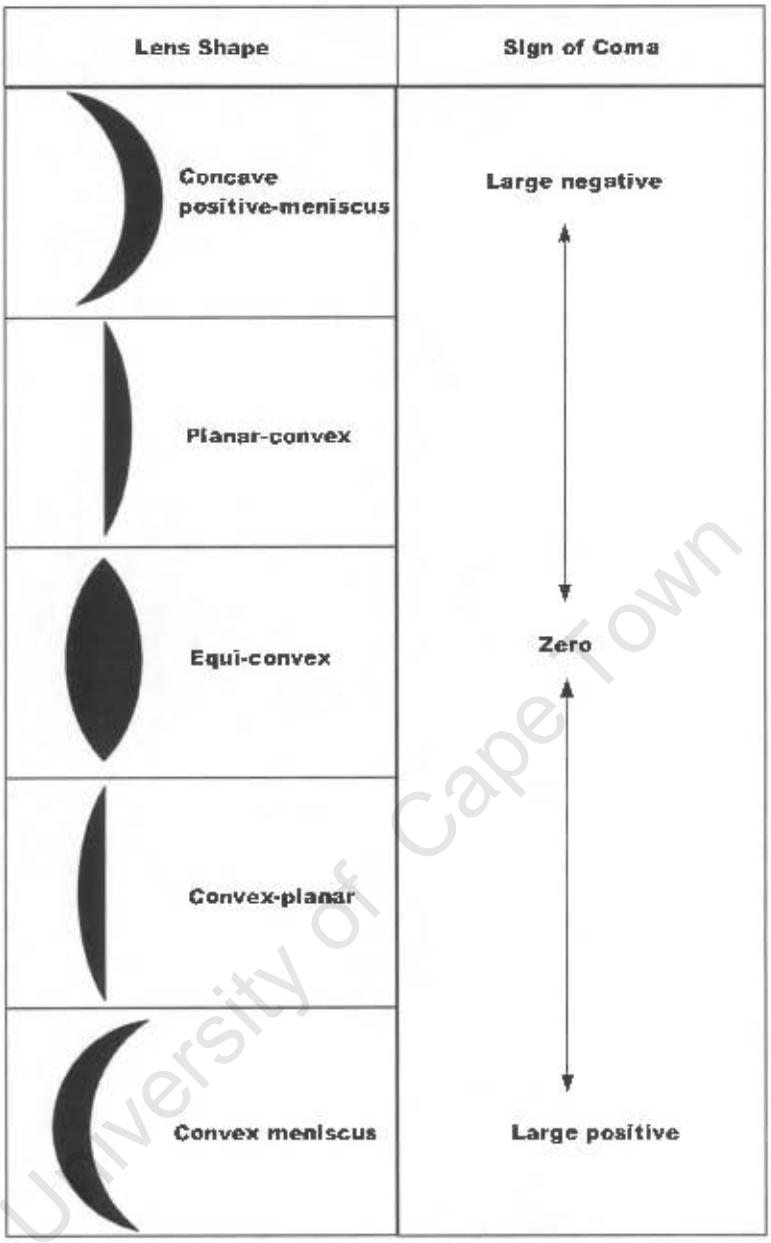

Figure 1.20: The affect of lens shape on coma

1.5.4 Field of Curvature

Field of curvature is closely related to astigmatism, in that any oblique ray will traverse the lens asymmetrically and therefore shortens its focal length as one travels away from the optical axis. This causes the image plane to develop into a 3-dimensional paraboloid, which

known as a *Petzval surface*, after the Hungarian mathematician Josef Max Petzval (1807-1891). Figure 1.21 illustrates this phenomenon, where it can be seen that the more oblique rays cause greater curvature. In the presence of astigmatism this problem is compounded since there will be two paraboloidal image surfaces corresponding with the tangential and sagittal conjugates.

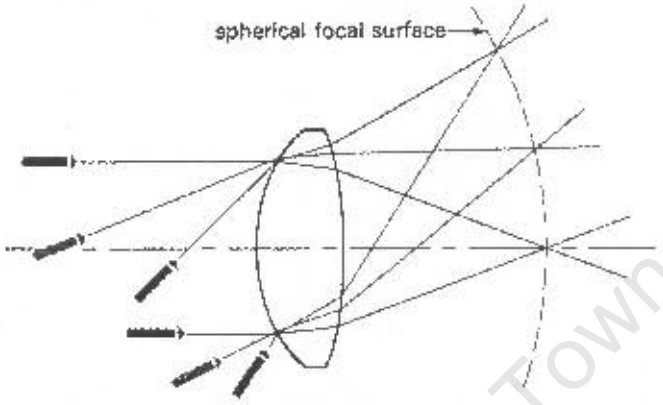

Figure 1.21: Field of curvature[27]

A positive lens develops an inward facing Petzval surface, where as a negative *field flattener* lens produces an outward facing Petzval surface. The right combination of positive and negative lenses will therefore negate curvature of field. Another approach is to simply place a spherical mirror, which conforms to the field of curvature, in the image plane.

1.5.5 Distortion

Distortion differs from the other monochromatic aberrations in that these aberrations refer to the failure of a lens to form a point image from a point object[31]. The fact that different areas of a lens have different focal lengths and different magnifications produces distortion. Distortion does not produce a lack of sharpness but causes the magnification of the image to vary with distance from the optical axis. This simply means that a lens will image an object point perfectly but it will be mapped to the wrong location on the image plane. *Pincushion* or *positive distortion* is when magnification increases with increasing distance from the optical axis, as illustrated in figure 1.22(a). It can be seen from figure 1.22(b) that *barrel* or *negative distortion* is the opposite of pincushion distortion since magnification decreases with

increasing distance from the optical axis. Furthermore, it can be seen that distortion increases as one moves away from the optical axis.

Figure 1.22: Distortion[27]

Distortion can be prevented by placing a stop midway between two identical lenses. By doing so distortion created by the first lens will be eliminated by the second lens. Furthermore, a perfectly symmetrical optical with a magnification ratio of 1:1 will eliminate distortion as well as coma and lateral color for that matter. Another method of negating distortion is by using a fairly thin lens, which develops relatively little distortion.

1.5.6 Chromatic Aberration

Chromatic aberration differs from the aberrations discussed earlier as it only occurs in polychromatic light. The quintessential feature of chromatic aberration lies in the fact that the index of refraction of a material is a function of its wavelength. This means that blue light (i.e. short wavelength light) will come to a focus closer (i.e. due to a higher index of refraction) to the lens then red light (i.e. long wavelength light), if the light traverses a positive lens element as shown in figure 1.23. When the blue light comes to focus before the red light it is known as positive chromatic aberration and if the opposite occurs, it is known as negative chromatic aberration. The horizontal distance between the two focal points is known as *longitudinal chromatic aberration* or *longitudinal color*. The minimum cross-sectional area between the two focal points is known as the *circle of least confusion* where the best image will be produced.

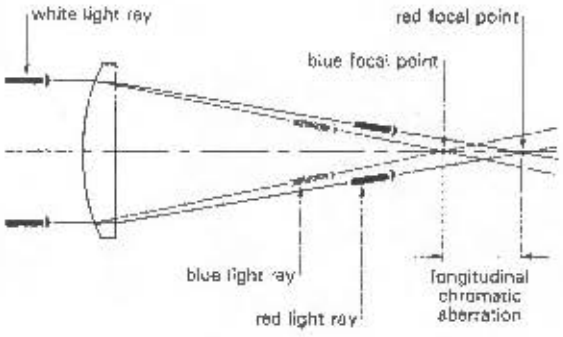

Figure 1.23: Longitudinal chromatic aberration[27]

Chromatic aberration can be eliminated in the same manner as spherical aberration in that positive and negative lenses produce opposite signs of chromatic aberration. Therefore the right combination of these lenses can produce a chromatic aberration-free optical system, known as a *doublet*.

1.5.7 Lateral Color

Lateral color like chromatic aberration only poses a problem in polychromatic light and is the lateral effect of chromatic aberration. The main characteristic of lateral color is that blue light will have a higher index of refraction then red light, which causes the rays to intercept the image plane at different heights, as shown in figure 1.24. This in effect causes a magnification difference. This means that if one were to place a screen at the blue focus one would see a smaller image with its details surrounded by a red halo and if one were to move the screen to the red focus, the image will be larger with its details having a blue halo.

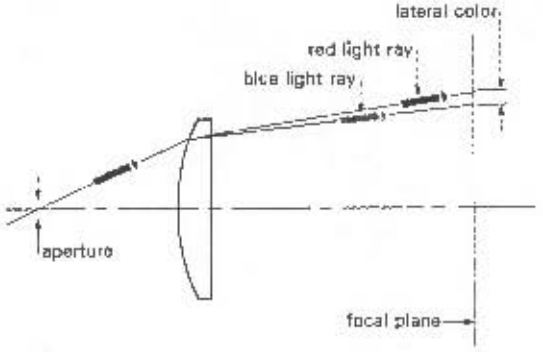

Figure 1.24: Lateral color[27]

Lateral color can be eliminated by judiciously placing a stop within the optical system. When using a simple lens, lateral color is negated if the stop is in contact with the lens.

APPENDIX B

2. Derivation of the final Intensity Distribution in Digital Shearography

Let $a = \theta(x+\delta x, y) + \theta(x, y)$ and $b = \Delta\phi$

Therefore

$I_a = 2A^2(1+\cos a)$ *And*

$I_b = 2A^2(1+\cos(a+b))$

$I_r = I_a - I_b = 2A^2(1+\cos a) - 2A^2(1+\cos(a+b))$

$\Rightarrow 2A^2 + 2A^2\cos a - 2A^2 - 2A^2\cos(a+b)$

$\Rightarrow 2A^2\cos a - 2A^2\cos a\cos b + 2A^2\sin a\sin b$ *Since* $\cos(x+y) = \cos x\cos y - \sin x\sin y$

$\Rightarrow 2A^2\cos a[1-\cos b] + 2A^2\sin a\sin b$

$\Rightarrow 2A^2\cos a\left[1-1+2\sin^2\frac{b}{2}\right] + 2A^2\sin a\sin b$ *Since* $\cos y = 1-2\sin^2\frac{y}{2}$

$\Rightarrow 2A^2\cos a\left(2\sin^2\frac{b}{2}\right) + 2A^2\sin a\sin b$

$\Rightarrow 4A^2\cos a\sin^2\frac{b}{2} + 2A^2\sin a\sin b$

$\Rightarrow 4A^2\cos a\sin^2\frac{b}{2} + 2A^2\sin a\left(2\sin\frac{b}{2}\cos\frac{b}{2}\right)$ *Since* $\sin y = 2\sin\frac{y}{2}\cos\frac{y}{2}$

$\Rightarrow 4A^2\cos a\sin^2\frac{b}{2} + 4A^2\sin a\cos\frac{b}{2}\sin\frac{b}{2}$

$\Rightarrow 4A^2\left[\cos a\sin\frac{b}{2} + \sin a\cos\frac{b}{2}\right]\sin\frac{b}{2}$

$\therefore I_r = 4A^2\left[\sin\left(a+\frac{b}{2}\right)\right]\sin\frac{b}{2}$ *Since* $\sin(x+y) = \sin x\cos y + \cos x\sin y$

APPENDIX C

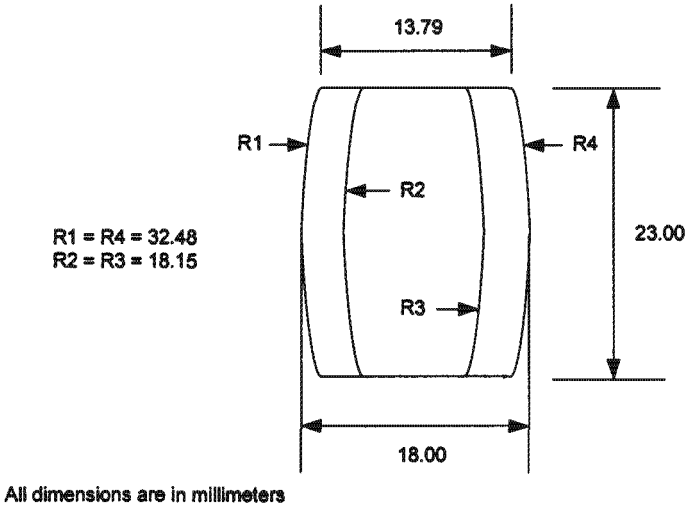

Schematic of the Hastings triplet

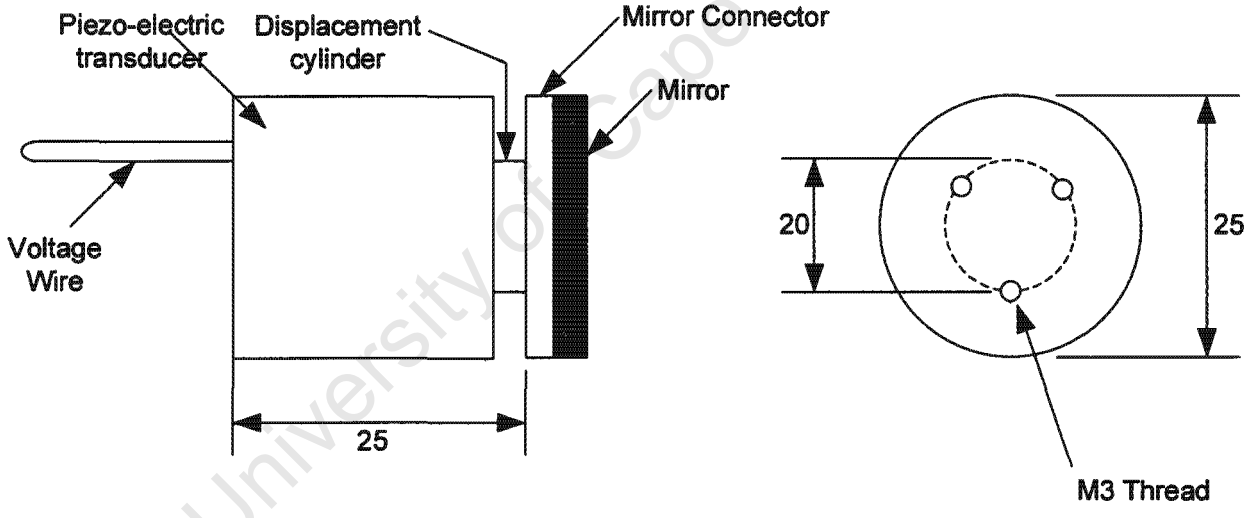

Schematic of the Piezo-electrically Driven Mirror

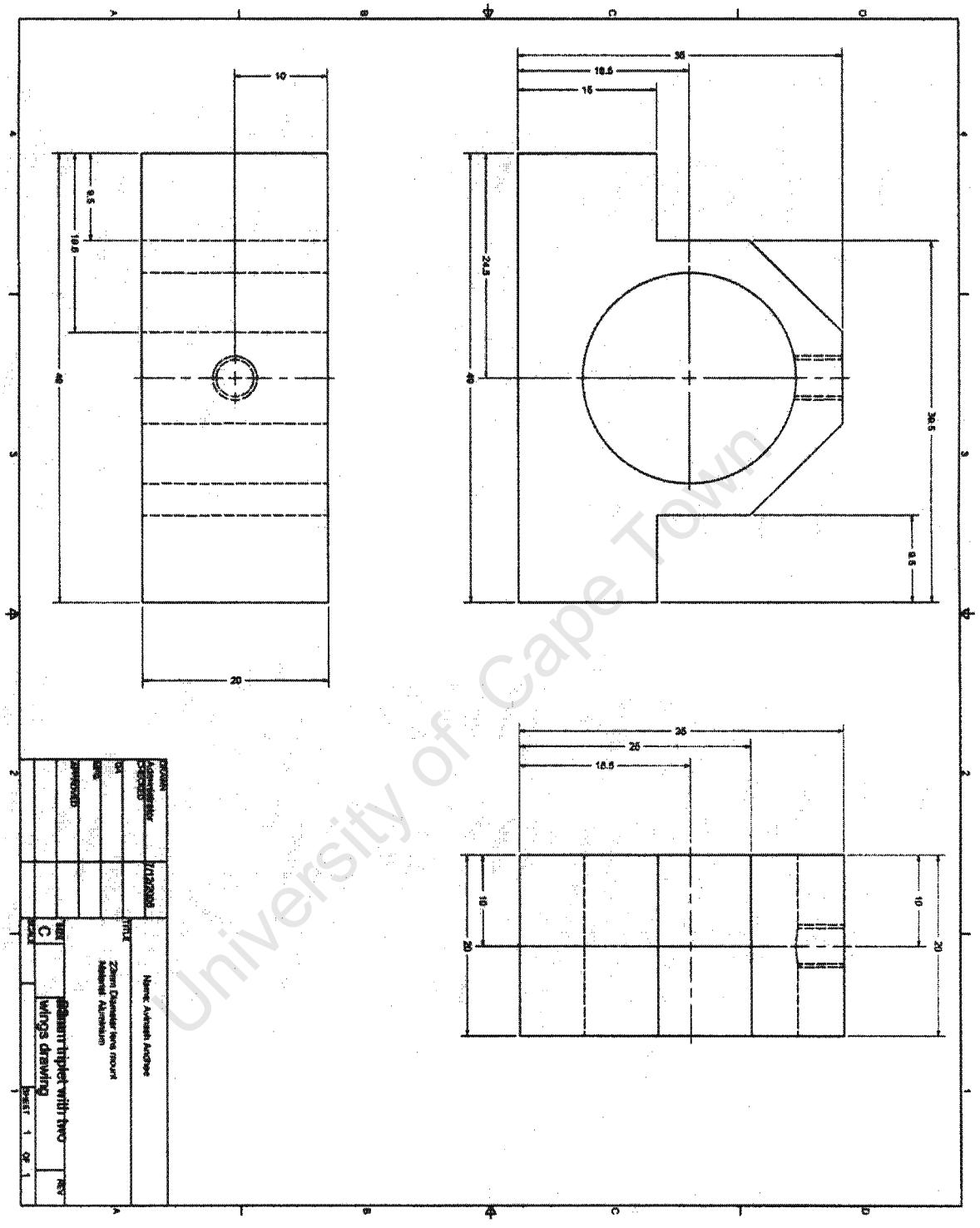

Schematic of the lens mount

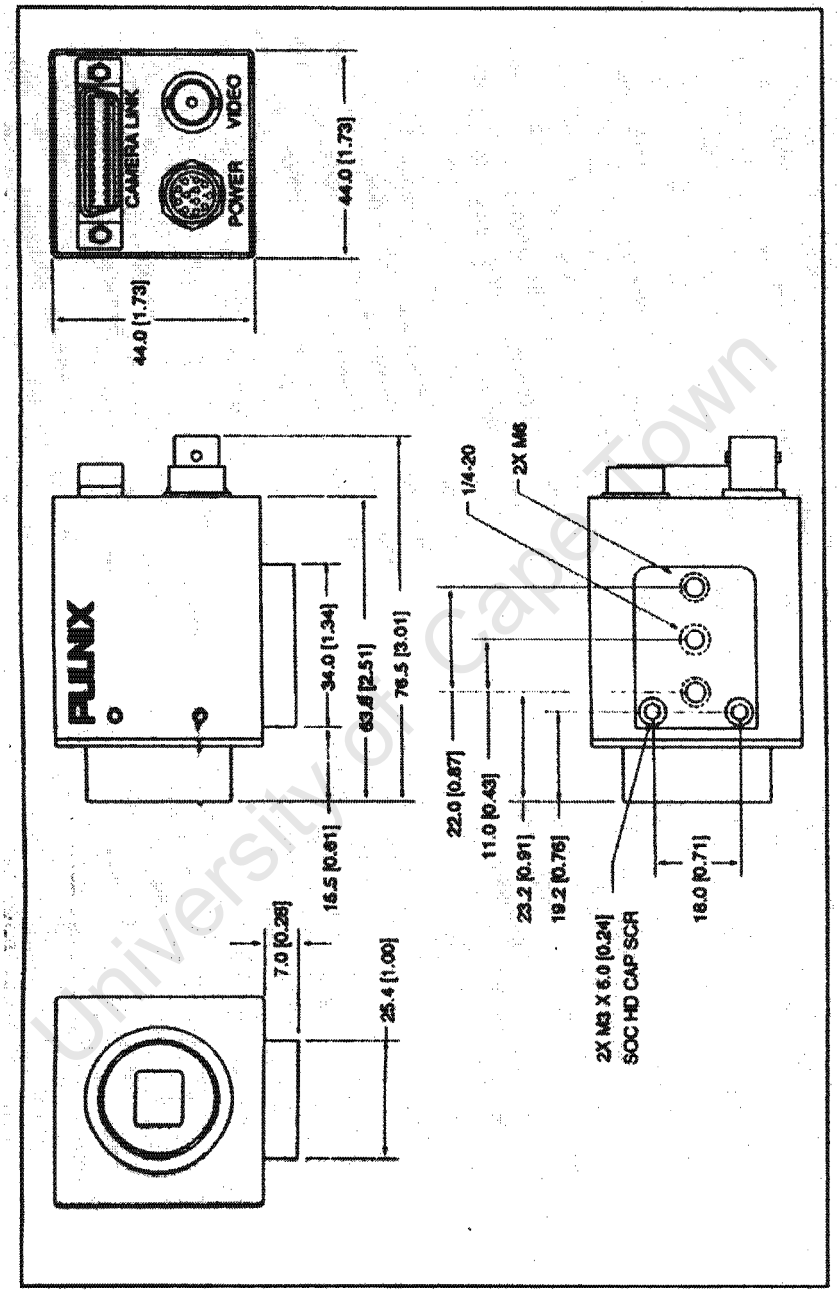

Schematic of the CCD Camera

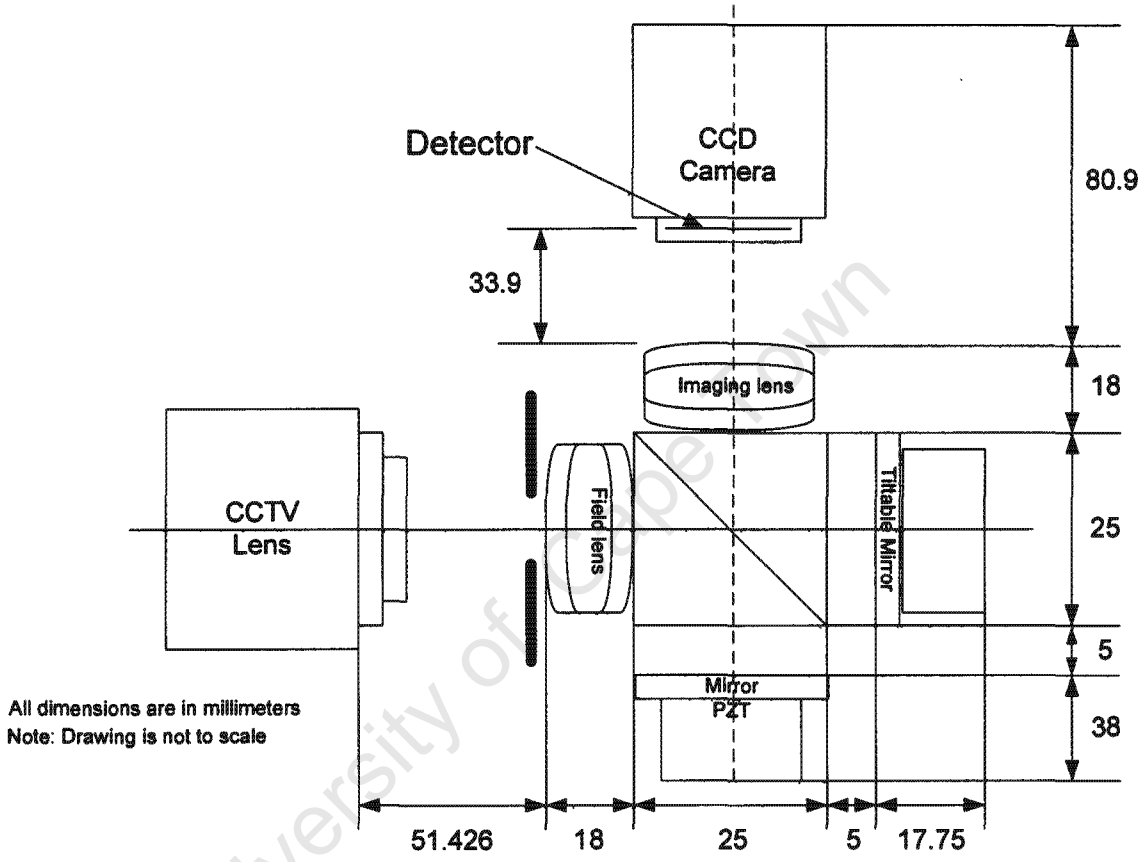

Schematic of the Compact Shearographic System

APPENDIX D

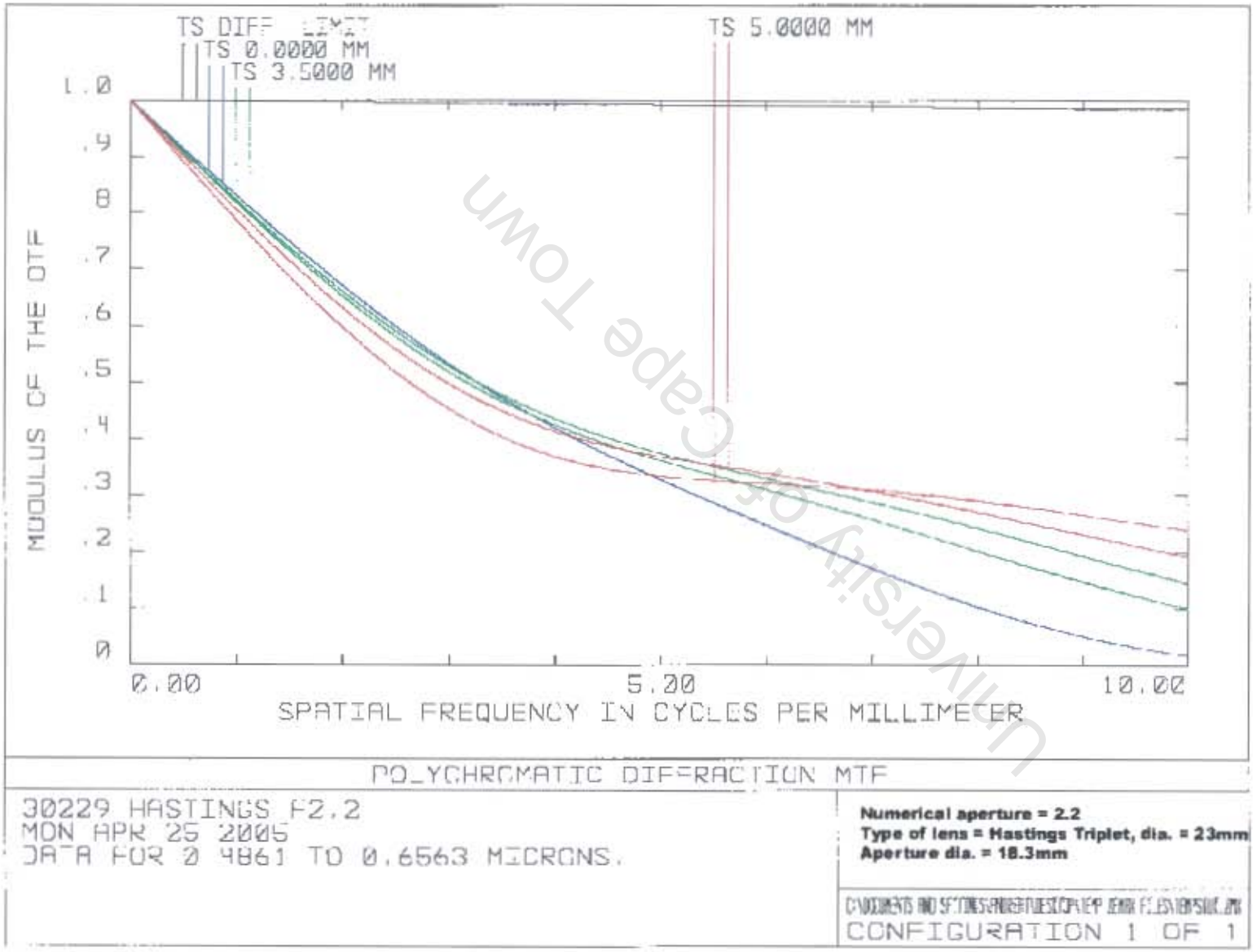

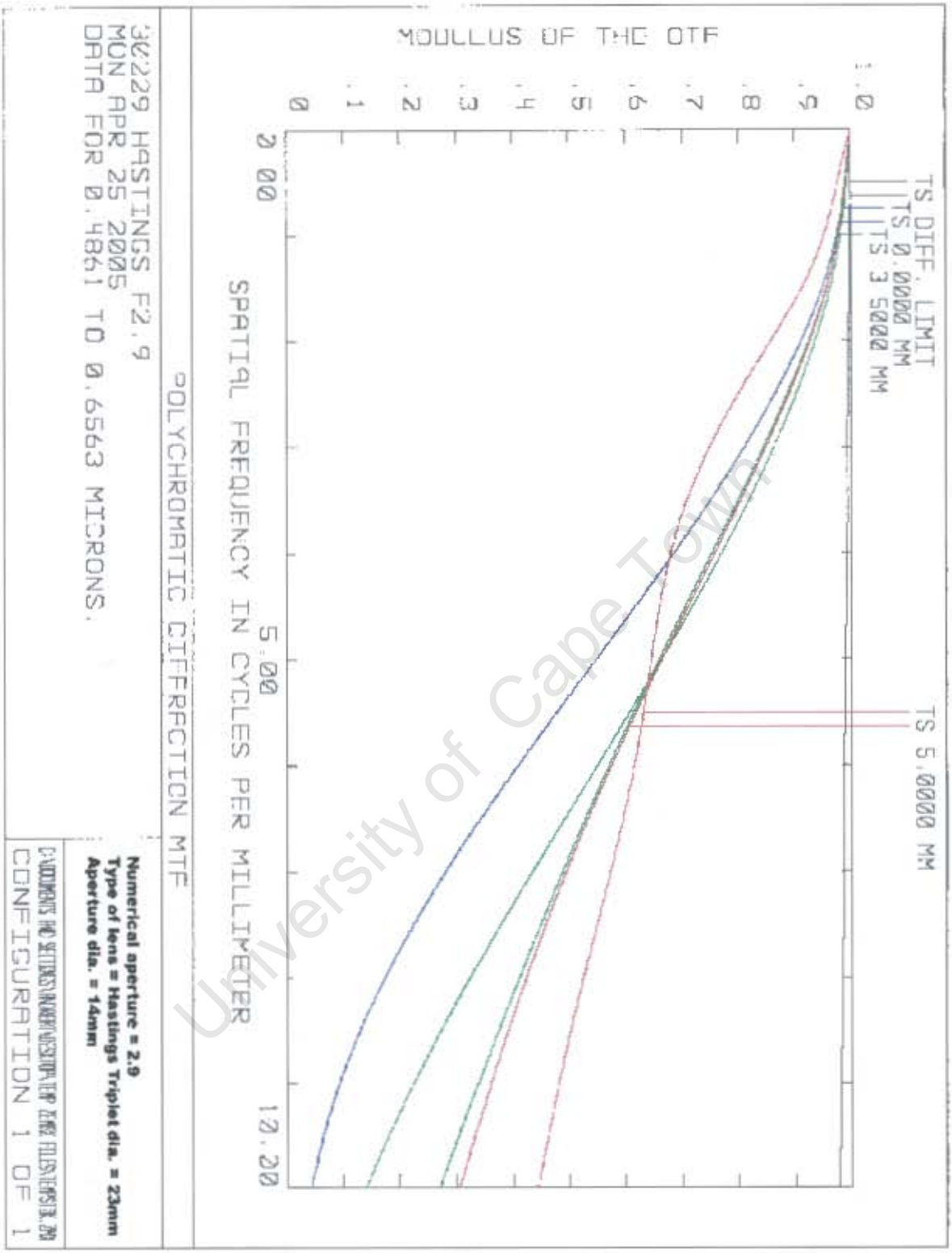

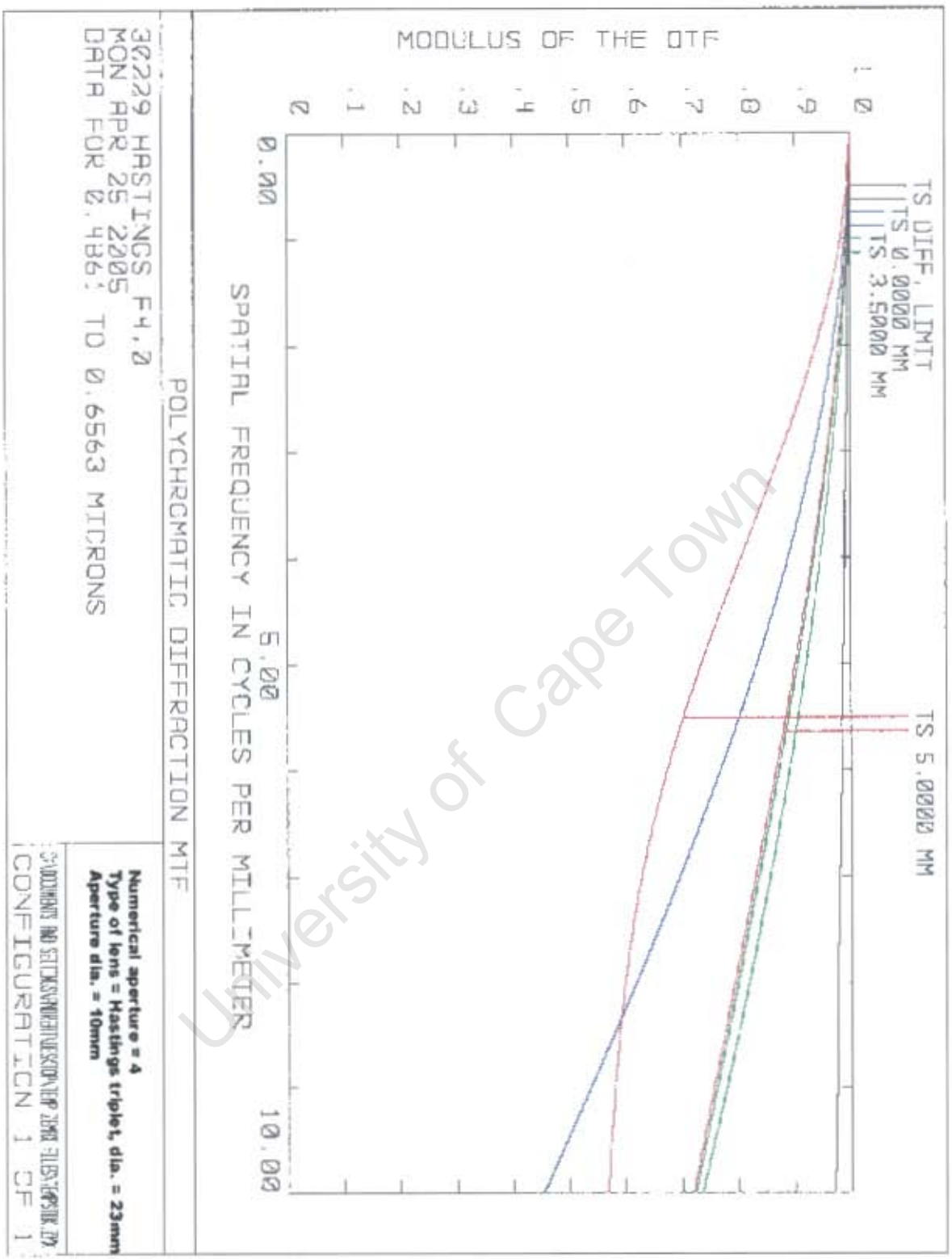

APPENDIX E

OPTICAL SIMULATIONS FOR DESIGN CONCEPT A

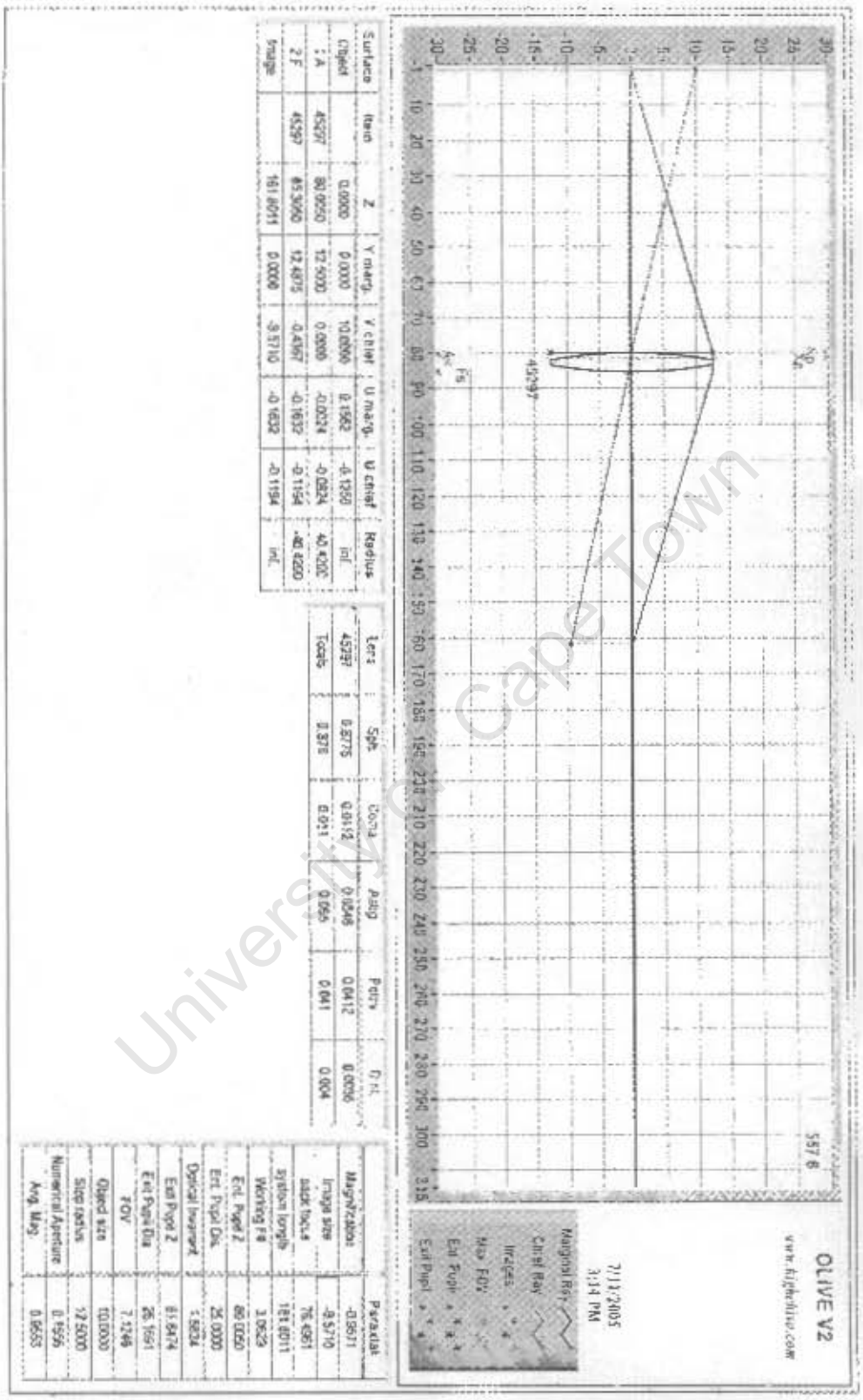

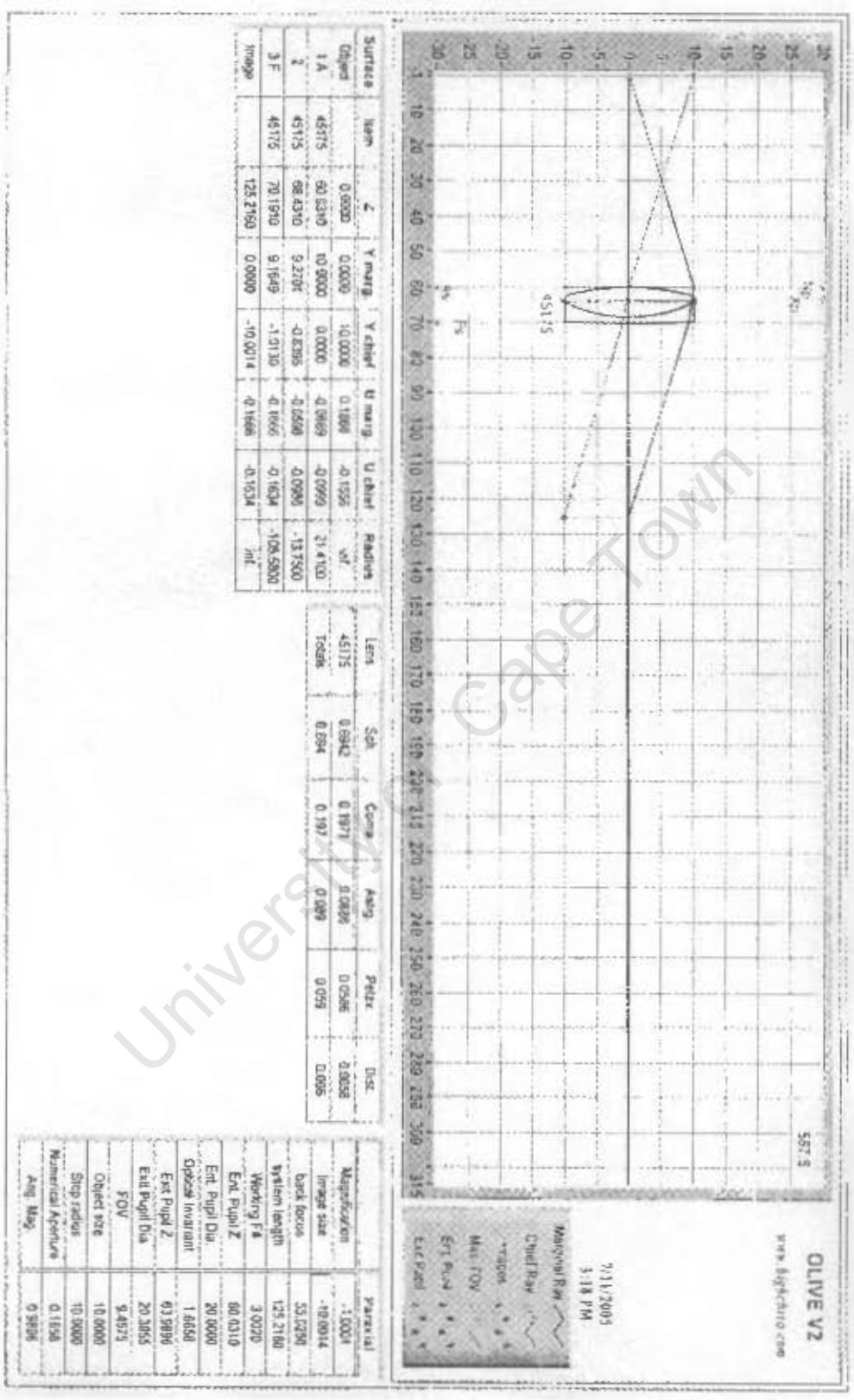

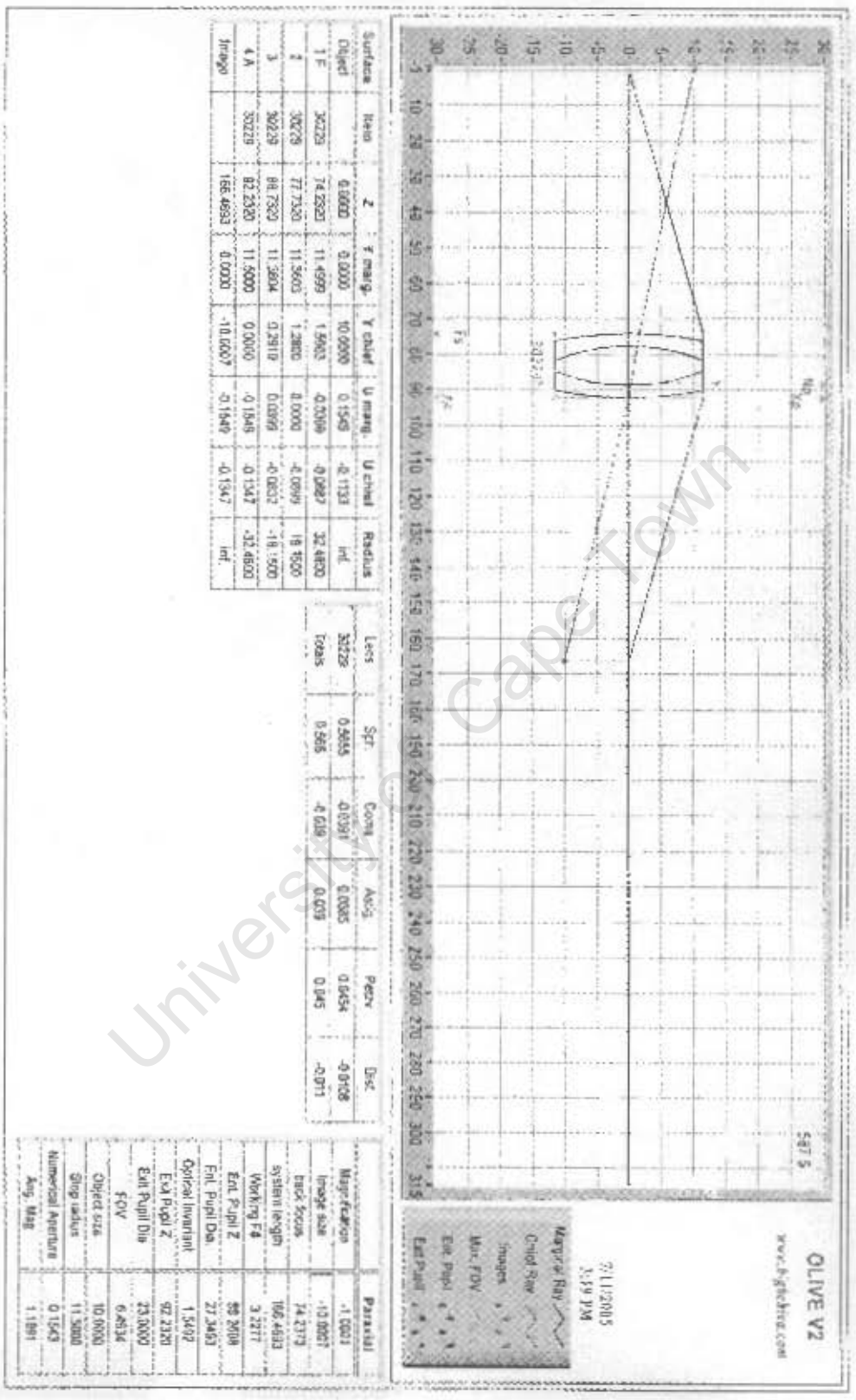

OPTICAL SIMULATIONS FOR DESIGN CONCEPT B

Surface	Item	Z	Y marg	Y chief	U marg.	U chief	Radius
Object		0.0000	0.0000	10.0000	0.3327	0.4071	inf.
1 F	32013	16.8100	5.5930	16.8439	0.1135	-0.0902	18.0100
2	32013	20.2900	5.9881	16.6691	0.0004	-0.5545	-18.0100
3 A	32013	50.3500	0.0000	0.0000	-0.1132	-0.3696	18.0100
4	32013	53.8300	5.8069	-1.2723	-0.3326	-0.5180	-18.0100
Image		70.6629	0.0000	-10.0024	-0.3326	-0.5180	Inf.

Loss	Sph	Coma	Astig	Petzv	Dist
32013	0.6459	-1.4645	3.5756	0.4189	-11.1471
32013	0.6497	-0.3333	0.4279	0.4189	0.2318
Totals	1.296	-1.798	4.004	0.838	-10.915

	Paraxial
Magnification	-1.0002
Image size	-10.0024
back focus	16.8529
system length	70.6629
Working F#	1.5031
Ent. Pupil Z	-24.5659
Ent. Pupil Dia	16.3443
Optical Invariant	3.3272
Exit Pupil Z	51.3740
Exit Pupil Dia	12.8467
FOV	-22.1529
Object size	10.0000
Stop radius	8.0000
Numerical Aperture	0.3266
Ang. Mag.	-1.2724

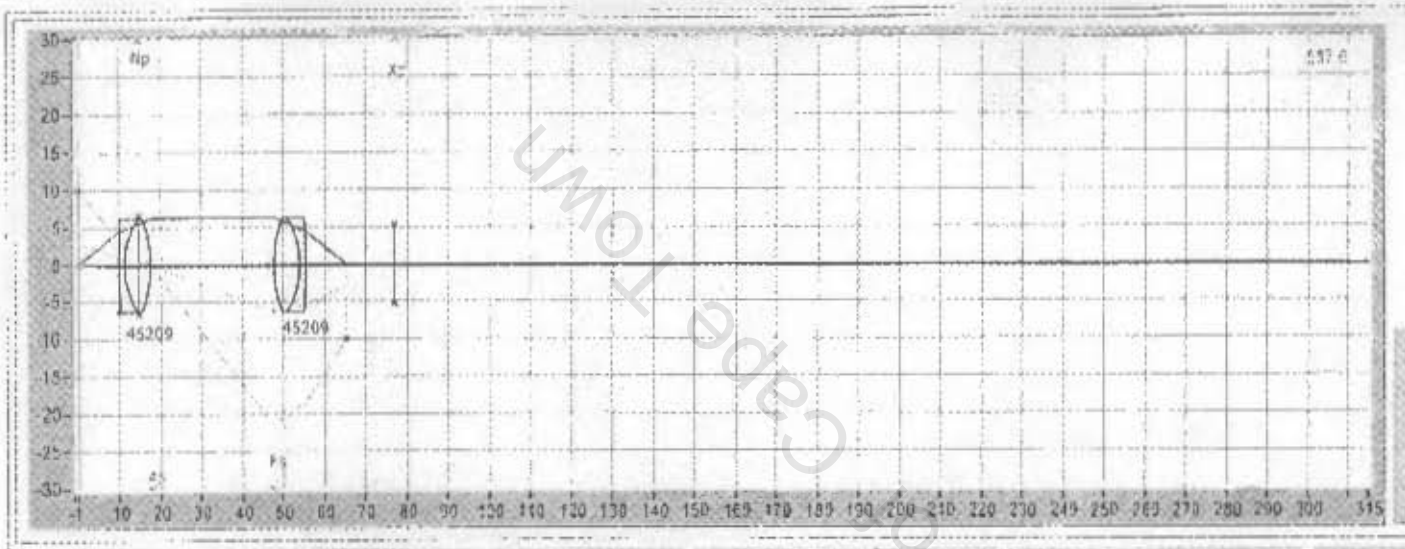

Surface	Item	Z	Y marg.	Y chief	U marg.	U chief	Radius
Object		0.0000	0.0000	10.0000	0.4460	-0.8752	inf.
1	45209	9.8200	4.4239	3.3025	0.2351	-0.4271	56.5400
2	45209	11.4200	4.7766	2.6618	0.2365	-0.4273	7.7200
3 A	45209	17.6500	6.2500	0.9000	-0.0001	-0.7135	-10.6000
4 F	45209	47.1900	6.2472	-21.4829	-0.2365	0.3851	10.6000
5	45209	53.9600	4.7737	-19.0636	-0.2351	0.3808	-7.7200
6	45209	55.4600	4.4210	-18.4926	-0.4459	0.8566	-56.5400
Image		65.3741	0.0000	-10.0005	-0.4459	0.8566	inf.

Lens	Sph.	Coma	Astg.	Petzv.	Dist
45209	0.6691	0.0631	0.9647	0.8917	-0.6856
45209	0.6677	2.2300	8.4080	0.8917	38.5116
Totals	1.337	2.293	9.373	1.783	37.826

	Paraxial
Magnification	-1.0001
Image size	-10.0005
back focus	9.9141
system length	65.3741
Working F#	1.1213
Ent. Pupil Z	14.8114
Ent. Pupil Dia	13.2104
Optical Invariant	4.4555
Exit Pupil Z	77.8491
Exit Pupil Dia	10.4124
FOV	34.6254
Object size	10.0000
Stop radius	6.2500
Numerical Aperture	0.4313
Ang. Mag.	-1.2687

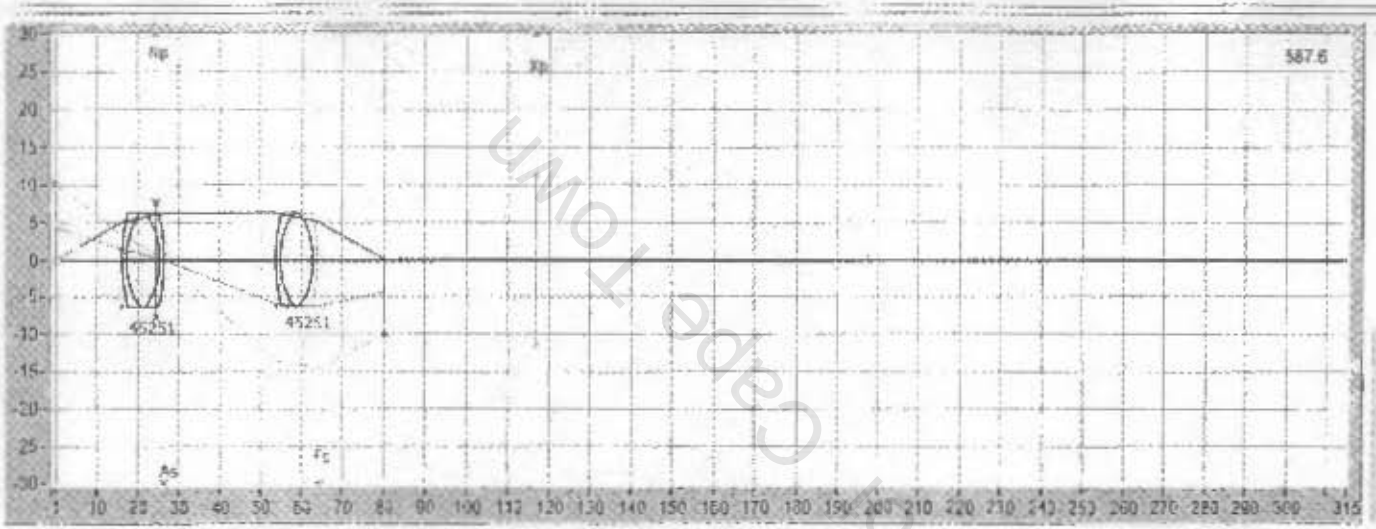

Surface	Item	Z	Y marg.	Y chief	U marg.	U chief	Radius
Object		0.0000	0.0000	10.0000	0.3122	-0.4988	Inf.
1	45251	16.3100	5.0922	3.3634	0.0624	-0.3373	14.9500
2	45251	17.4100	5.1606	2.9924	0.1145	-0.3325	7.3400
3	45251	25.9300	6.0741	0.3392	0.1699	-0.3083	-7.3400
4 A	45251	26.4900	6.2500	0.0000	-0.0002	-0.4995	-14.9500
5	45251	53.7790	6.2453	-13.6319	-0.1600	0.0436	14.9500
6	45251	54.8790	6.0693	-13.5872	-0.1146	-0.0826	7.3400
7	45251	62.9590	5.1548	-14.2463	-0.0628	-0.2010	-7.3402
B F	45251	63.9590	5.0660	-14.4674	-0.3123	0.2744	-14.9500
Image		80.2468	0.0000	-9.9985	-0.3123	0.2744	Inf.

Lens	Sph.	Coma	Astig	Petzv	Dist.
45251	0.2436	0.1519	0.1519	0.3875	-0.3401
45251	0.2431	0.3293	0.6489	0.3875	2.5416
Totals	0.487	0.530	0.800	0.775	2.201

	Paraxial
Magnification	-0.9999
Image size	-9.9985
back focus	16.2878
system length	80.2468
Working F#	1.6012
Ent. Pupil Z	24.5758
Ent. Pupil Dia.	15.3457
Optical Invariant	3.1221
Exit Pupil Z	149.6885
Exit Pupil Dia	22.7584
FOV	22.1436
Object size	10.0000
Stop radius	6.2500
Numerical Aperture	0.3072
Ang. Mag.	-0.6248

OPTICAL SIMULATIONS FOR DESIGN CONCEPT C

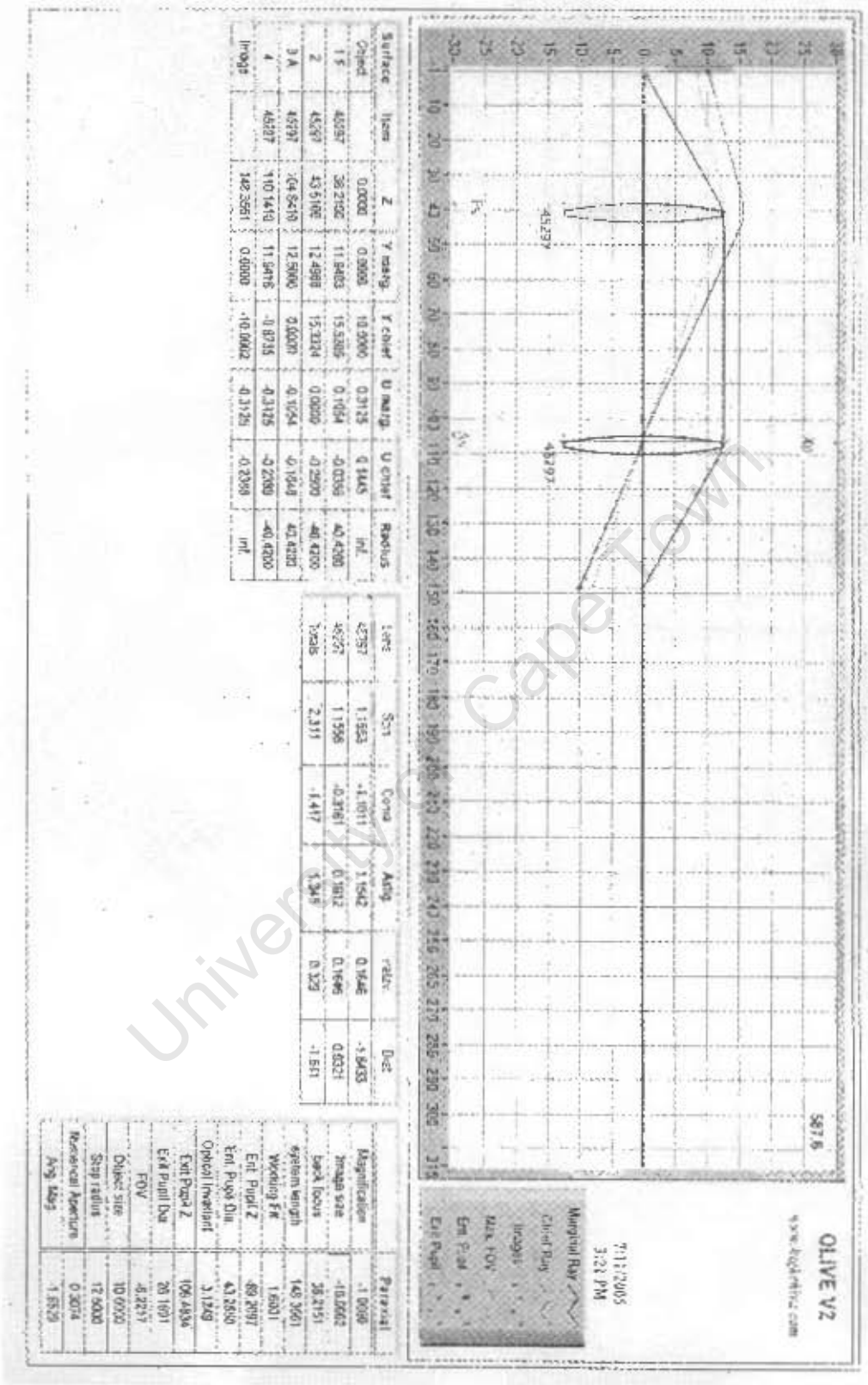

Surface	Type	Z	Y marg	Y chief	U marg	U chief	Radius
Object		0.0000	0.0000	10.0000	0.3125	0.1445	Infinity
1 F	45297	38.2192	11.9403	15.5305	0.1034	-0.0356	40.4200
2	45297	43.5192	12.4988	15.3324	0.0000	-0.2909	-40.4200
3 A	45297	104.8419	12.5000	0.0000	-0.1034	-0.1944	40.4200
4	45297	110.1419	11.9416	-9.8735	-0.3125	-0.2369	-40.4200
Image		148.3561	0.0000	-10.0002	-0.3125	-0.2369	Infinity

Type	Conic	Asphe	rotate	Dec
45297	1.1553	-1.1011	1.1542	0.1646	-5.8433
45297	1.1556	-0.3761	0.1612	0.1646	0.6321
Tomas	2.311	-1.417	1.345	0.329	-1.551

Paraxial	
Magnification	-1.0000
Image size	-10.0002
back focus	38.2151
system length	148.3561
Working F#	1.6931
Ent. Pupil Z	-89.2197
Ent. Pupil Dia	43.2650
Optical Invariant	3.1249
Ent Pupil Z	106.4934
Exit Pupil Dia	26.1691
FOV	-5.2257
Object size	10.0000
Stop radius	12.5000
Numerical Aperture	0.3074
Avg. Mag	1.8529

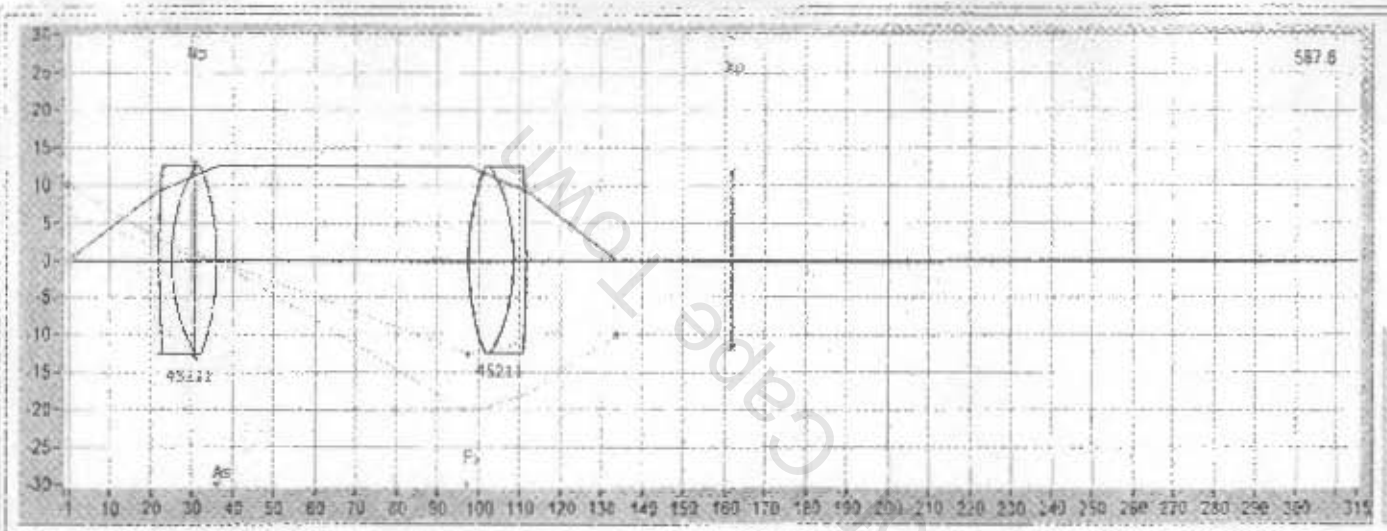

Surface	Item	Z	Y marg.	Y chief	U marg.	U chief	Radius
Object		0.0000	0.0000	10.0000	0.4166	-0.3541	inf.
1	45211	22.2330	9.2607	2.7855	0.2082	-0.1975	118.6600
2	45211	25.2390	9.8852	2.2031	0.2368	-0.1996	16.0800
3 A	45211	36.2700	12.5000	0.0000	-0.0004	-0.3333	-21.1700
4 F	45211	97.5510	12.4949	-20.4751	-0.2369	0.1875	21.1700
5	45211	108.5910	9.8801	-19.3532	-0.2082	0.1427	-16.0800
6	45211	111.5910	9.2556	-17.9660	-0.4166	0.3567	-118.6600
Image		133.8001	0.0000	-10.0002	-0.4166	0.3567	inf.

Lens	Sph.	Coma	Astig.	Petzv	Dist
45211	0.8622	0.0272	0.4424	0.3688	-0.1106
45211	0.8605	1.3787	2.8505	0.3688	6.4378
Totals	1.723	1.406	3.293	0.738	6.327

	Paraxial
Magnification	-1.0000
Image size	-10.0002
back focus	22.2181
system length	133.8091
Working F#	1.2003
Ent. Pupil Z	30.8557
Ent. Pupil Dia.	25.7081
Optical Invariant	4.1659
Exit Pupil Z	161.8459
Exit Pupil Dia	23.3591
FOV	17.9670
Object size	10.0000
Stop radius	12.5000
Numerical Aperture	0.4046
Ang. Mag	-1.1006

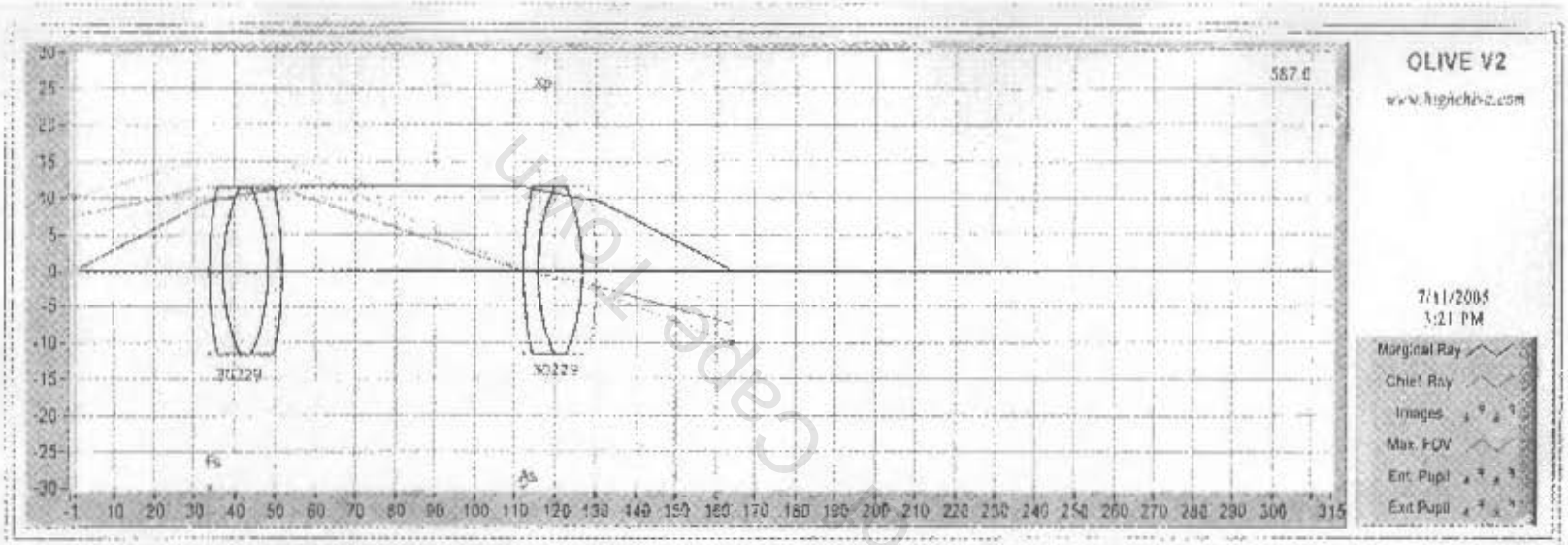

Surface	Item	Z	Y marg.	Y chief	U marg.	U chief	Radius
Object		0.0000	0.0000	10.0000	0.2351	0.1629	Inf.
1 F	30229	53.6960	9.6045	15.5229	0.0621	-0.0523	32.4800
2	30229	57.3960	9.6819	15.2347	0.1034	-0.0308	18.1500
3	30229	48.3960	11.0193	14.8998	0.1305	0.0235	-18.1500
4	30229	51.8960	11.4936	14.9779	0.0001	-0.2478	-32.4800
5 A	30229	112.3070	11.5000	0.0000	-0.1554	-0.1539	32.4800
6	30229	115.8070	11.0259	-2.5356	-0.1033	-0.1655	18.1500
7	30229	129.8070	8.8895	-2.3598	-0.0820	-0.1632	-18.1500
8	30229	130.3070	9.0724	-2.9270	-0.2351	-0.2085	-32.4800
Image		164.2330	0.0000	-10.0007	-0.2351	-0.2085	Inf.

Lens	Sph.	Coma	Astig.	Petzv	Dist
30229	0.5457	-0.6686	0.7345	0.1549	-1.2529
30229	0.5468	-0.1032	0.0768	0.1540	0.0705
Totals	1.093	-0.771	0.811	0.309	-1.183

	Paraxial
Magnification	-1.0001
Image size	10.0007
back focus	53.8253
system length	164.2330
Working F#	1.7538
Ent. Pupil Z	-61.3731
Ent. Pupil Dia	34.9979
Optical Invariant	2.8512
Exit Pupil Z	116.2992
Exit Pupil Dia	27.3493
FOV	-9.2543
Object size	10.0000
Stop radius	11.5000
Numerical Aperture	0.2813
Ang. Mag	-1.2797

HASTINGS TRIPLETS 70mm APART

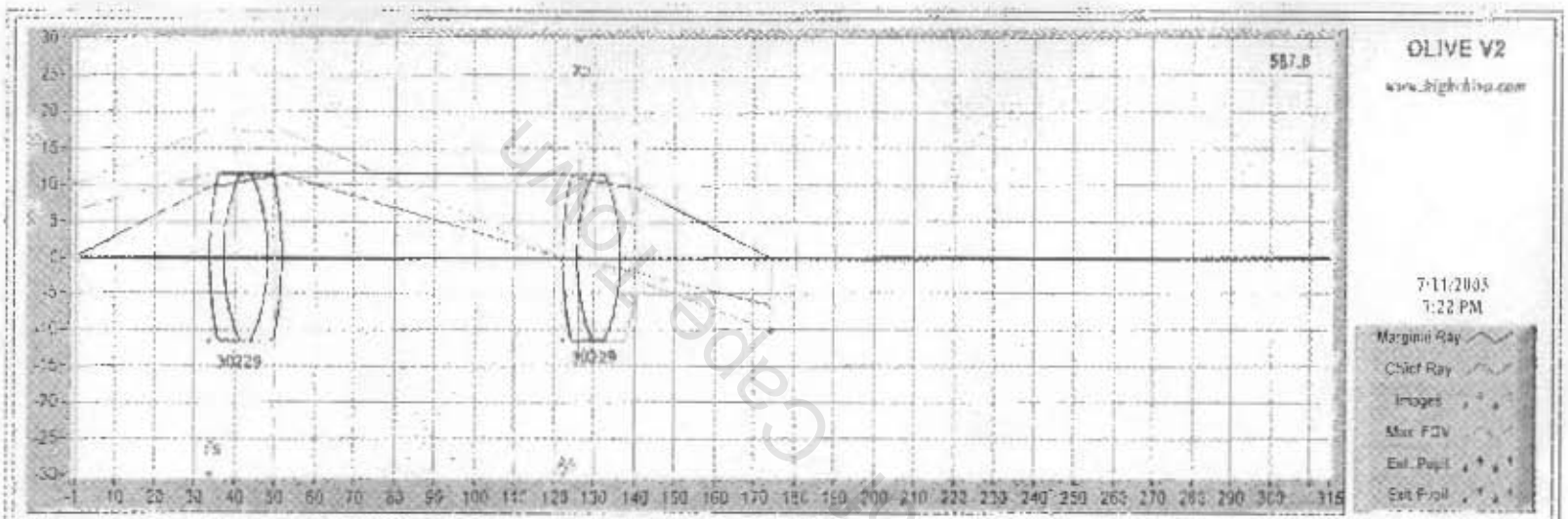

Surface	Item	Z	Y marg.	Y chief	U marg.	U chief	Radius
Object		0.0000	0.0000	10.0000	0.2851	0.2233	inf.
1 F	30229	33.8960	9.6636	17.5676	0.0621	-0.0092	32.4800
2	30229	37.3960	9.8810	17.3254	0.1034	-0.0060	18.1500
3	30229	48.3960	11.0133	17.2274	0.1355	0.0621	-68.1500
4	30229	51.8960	11.4925	17.4955	0.0001	-0.2478	-32.4800
5 A	30229	122.1210	11.5000	0.0000	-0.1354	-0.1536	32.4800
6	30229	125.6210	11.0299	-0.5356	-0.1833	-0.1466	18.1500
7	30229	136.6210	9.8856	-2.3556	-0.0620	-0.1532	-18.1500
8	30229	140.1210	9.6724	-2.9257	-0.3851	-0.2099	-32.4800
Image		174.0470	0.0000	-9.9998	-0.2851	-0.2085	inf.

Lens	Spn.	Curva.	Astig.	Petzv.	Dist.
30229	0.5456	-0.7232	1.0160	0.1539	-1.8383
30229	0.5468	-0.1031	0.0758	0.1539	0.0702
Totals	1.092	-0.826	1.092	0.308	-1.768

	Paraxial
Magnification	-1.0000
Image size	-9.9998
back focus	33.9260
system length	174.0470
Working F#	1.7539
Ent. Pupil Z	-44.7910
Ent. Pupil Dia	25.5396
Optical Invariant	2.8510
Exit Pupil Z	126.0832
Exit Pupil Dia	27.3493
FOV	-12.5654
Object size	10.0000
Stop radius	11.5000
Numerical Aperture	0.2813
Ang. Mag.	-0.9038

HASTINGS TRIPLETS 80mm APART

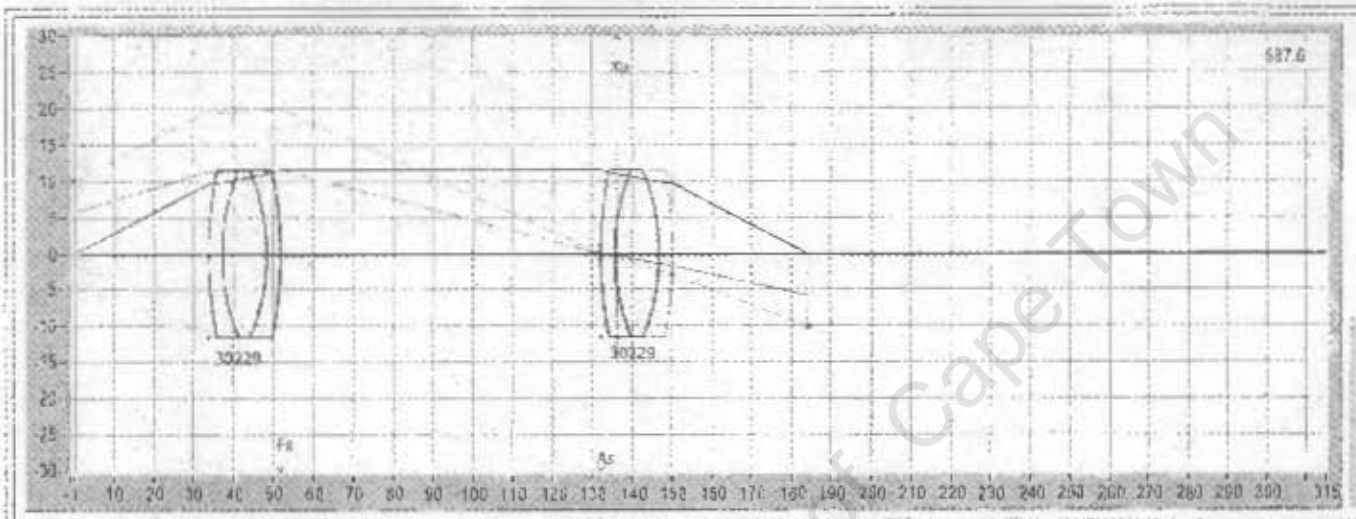

Surface	Item	Z	Y marg.	Y chief	U marg.	U chief	Radius
Object		0.0000	0.0000	10.0000	0.2851	0.2856	Inf.
1	30229	33.8950	8.6627	19.6802	0.0621	-0.0556	32.4800
2	30229	37.3950	9.8801	18.4855	0.1034	0.0137	18.1500
3	30229	46.8950	11.0173	18.6359	0.1355	0.0817	-18.1500
4 F	30229	51.8950	11.4915	19.9220	0.0001	-0.2479	-32.4800
5 A	30229	132.2830	11.5000	0.0000	-0.1354	-0.1539	32.4800
6	30229	135.7830	11.0259	-0.8386	-0.1033	-0.1854	18.1500
7	30229	146.7830	9.8896	-2.3553	-0.0620	-0.1832	-18.1500
8	30229	150.2830	8.6724	-2.9264	-0.2851	-0.2085	-32.4800
Image		184.1890	0.0000	-9.9988	-0.2851	-0.2085	Inf.

Lens	Sph	Coma	Astig.	Petzv	Dist
30229	-0.5453	-0.8422	1.3580	0.1539	-2.6474
30229	-0.5468	-0.1031	0.0798	0.1539	0.0702
Total	1.092	-0.946	1.438	0.308	-2.577

	Paraxial
Magnification	-0.9999
Image size	-9.9988
back focus	33.9260
system length	184.1890
Working F#	1.7538
Ent. Pupil Z	-35.0158
Ent. Pupil Dia.	19.9639
Optical Invariant	2.8507
Exit Pupil Z	135.2252
Exit Pupil Dia	27.3453
FOV	-15.9386
Object size	10.0000
Stop radius	11.5000
Numerical Aperture	0.2812
Ang. Mag	-0.7300